Experimental study of plasma turbulence in the TCV tokamak

THÈSE N^{O} 7715 (2017)

PRÉSENTÉE LE 1ER SEPTEMBRE 2017
À LA FACULTÉ DES SCIENCES DE BASE
SPC - PHYSIQUE DU TOKAMAK TCV
PROGRAMME DOCTORAL EN PHYSIQUE

ÉCOLE POLYTECHNIQUE FÉDÉRALE DE LAUSANNE

POUR L'OBTENTION DU GRADE DE DOCTEUR ÈS SCIENCES

PAR

Zhouji HUANG

acceptée sur proposition du jury:

Prof. V. Savona, président du jury
Dr S. Coda, directeur de thèse
Dr T. Happel, rapporteur
Dr C. Hidalgo, rapporteur
Prof. L. Villard, rapporteur

ÉCOLE POLYTECHNIQUE
FÉDÉRALE DE LAUSANNE

Suisse
2017

Abstract

This thesis presents an experimental investigation of electron density fluctuations in the TCV tokamak, primarily with the tangential phase contrast imaging (TPCI) diagnostic. The focus is to study the small-scale broadband turbulence in the plasma, which has long been believed to be the primary cause of anomalous transport, one of the most important issues for magnetic confinement fusion research. Nonlinear interactions within the turbulence can drive zonal flows, which in turn modulate and suppress the turbulence; geodesic acoustic modes (GAMs) are associated to zonal flows and easier to detect thanks to their finite frequency. A characterization of the GAMs in TCV with multiple diagnostics constitutes a central part of this work. The study includes spatial profile measurements as well as frequency and wavenumber spectra of turbulence and GAMs in various plasma conditions.

The first part of this work is dedicated to investigating the improvement in energy confinement when the triangularity (δ) at the edge of the plasma poloidal cross-section changes from positive to negative. Measurements of turbulent density fluctuations show a substantial reduction of the turbulence amplitude, decorrelation time and radial correlation length from positive to negative triangularity. In addition, the turbulence amplitude decreases with the effective collisionality of the plasma in the Trapped Electron Mode (TEM) regime. This result is consistent with the experimental observation of transport reduction in TCV and with nonlinear gyrokinetic simulations.

The second part of this thesis is focused on the characterization of the GAMs in TCV. A transition has been observed in the course of a single discharge from a local regime, with frequency varying along the radius according to a theoretically predicted linear dependence on the sound speed, to a radially extended regime, in which the oscillations are at a constant frequency over a large fraction of the minor radius. Gyrokinetic simulations succeed in reproducing the transition. The coupling between the GAM and the broadband turbulence was studied in a density ramp-up using bispectral techniques. The GAM has also been observed and characterized for the first time in the scrape-off layer (SOL), primarily by magnetic probes and Langmuir probes but also by D_α emission.

Key words: plasma, tokamak, fusion, phase-contrast imaging, turbulence, plasma shaping, collisionality, zonal flow, geodesic acoustic mode, scrape-off layer

Résumé

Cette thèse présente une investigation expérimentale des fluctuations de densité électronique dans le tokamak TCV (Tokamak à Configuration Variable), principalement à l'aide du diagnostique de contraste de phase tangentiel (TPCI). L'étude se concentre sur les turbulences de petite échelle à large bande , qui sont, depuis longtemps, suspectées d'être la cause principale du transport anormal, un défi majeur pour la fusion par confinement magnétique.

Les interactions non-linéaires dans la turbulence peuvent entrainer des flux zonaux qui, à leurs tours, modulent et suppriment la turbulence. Les modes acoustiques géodésiques (GAMs), associés aux flux zonaux, sont plus facilement détectables expérimentalement grace à leur fréquence finie. Une partie essentielle de ce travail est de caractériser les GAMs dans TCV à l'aide de diagnostiques multiples. L'étude comprend la mesure de profiles spatiaux, des spectres en fréquence et en nombre d'ondes de la turbulence et des GAMs pour différents plasmas.

La première partie de ce travail consiste à étudier l'amélioration du confinement énergétique qui est observé lorsque la triangularité (δ) de la dernière surface de flux magnétique fermée passe d'une valeur positive à négative. Lors de ce changement, les mesures de l'amplitude des fluctuations de densité montrent une réduction substantielle de l'amplitude, du temps de décorrelation ainsi que de la longueur de corrélation radiale de la turbulence. De surcroit, l'amplitude de la turbulence décroit avec la collisionalité effective du plasma dans le régime des modes d'électrons piégés. Ce résultat est en accord avec les observations de la réduction de transport dans TCV et avec les simulations gyrocinétiques non-linéaires.

La deuxième partie de cette thèse se concentre sur la caractérisation des GAMs dans TCV. Au cours de la même décharge, une transition a été observée depuis un régime local, exhibant une variation en fréquence le long du rayon dépendant linéairement de la vitesse du son, comme prédit par la théorie, à un régime étendu dans la direction radiale dans lequel les oscillations ont une fréquence constantes pour une large fraction du petit rayon. Les simulations gyrocinétiques reproduisent avec succès cette transition. Le couplage entre le GAM et la turbulence à large bande a été étudiée par le truchement de techniques bispectrales durant l'accroisement de densité. Le GAM a aussi été observé et caractérisé pour la première fois dans le Scrape Off Layer (SOL), principalement à l'aide de sondes magnétiques et de Langmuir, mais aussi par emission D_α.

Mots clefs : plasma, tokamak, fusion, contrast de phase, turbulence, flux zonal, modes acoustiques géodésiques, scrape off layer

Contents

List of Figures

List of Tables

1 Introduction

1.1 Thermonuclear fusion and tokamaks

Nuclear fusion is one of the fundamental energy production mechanisms in the universe. The binding energy of the nuclei in nature increases with the mass of the nucleus up to iron, then decreases. Therefore, either fusing of lighter nuclei or splitting of heavier nuclei would release the binding energy. The former process corresponds to nuclear fusion while the latter to nuclear fission. Besides nuclear fission reactors, most energy resources used in civilization such as coal, petroleum, natural gas originates from the energy radiated from the sun, which is essentially a natural nuclear fusion reactor like all other stars.

It would be a historical breakthrough for humans if nuclear fusion were achieved on earth with the energy released in a controlled way and converted into electricity. The main difficulty lies in the fact that all nuclei are positively charged, therefore the nuclei are required to have considerable kinetic energy to overcome the electrostatic repulsion and collide. The fuel has to be sufficiently dense and at high temperature at the same time to maximize the fusion reaction rate. In addition, the energy needs to be confined for a sufficiently long time to maintain the required temperature with minimum power in order to have net positive energy generation. The well-known Lawson criterion states the condition to reach ignition, i.e. the condition for the released fusion power to be sufficient to maintain the burning regime: the "triple" product of density n, temperature T and energy confinement time τ_E needs to exceed a threshold value:

$$n T \tau_\mathrm{E} \geq \frac{12 k_\mathrm{B} T^2}{< \sigma v > \epsilon} \tag{1.1}$$

where k_B is the Boltzmann constant, σ is the fusion cross section, v is the relative velocity, <> denotes an average over the Maxwellian velocity distribution, ϵ is the energy of the charged fusion products. The reaction with the largest cross-section of all possible fusion reactions is the deuterium-tritium (D-T) reaction:

$$\mathrm{D} + \mathrm{T} \rightarrow \mathrm{He}\,(3.5\ \mathrm{MeV}) + \mathrm{n}\,(14.1\ \mathrm{MeV}) \tag{1.2}$$

For a D-T reaction, the energy of the fusion generated α particles is $\epsilon = 3.5$ MeV, and the minimum triple-product lies in the temperature range about of 10 to 20 keV, which far exceeds the electron binding energy of the atoms. This means that at such high temperature, atoms are ionized into negatively charged electrons and positively charged ions. This state of matter is called a plasma, which accounts for most matter in the observed universe. To confine the hot plasma against the thermal pressure therefore becomes the key problem in achieving fusion. In the case of stars, their massive gravitation serves this purpose. For humans, two main approaches have been developed in mainstream fusion research: one is inertial confinement, which initiates fusion reactions by compressing the fuel target with shock waves generated by high energy laser beams, resulting in a very high plasma density $n \sim 10^{30}\ \mathrm{m}^{-3}$ and high reaction rate, so that a significant fraction of the fuel can burn before the energy dissipation, and only a short confinement time $\tau_\mathrm{E} \sim 10^{-9}$ s is needed; the other is magnetic confinement, which uses a strong magnetic field to trap the charged particles in a low density plasma, $n \sim 10^{20}\ \mathrm{m}^{-3}$, however for a much longer confinement time, typically $\tau_\mathrm{E} > 1.5$ s in case of a fusion reactor.

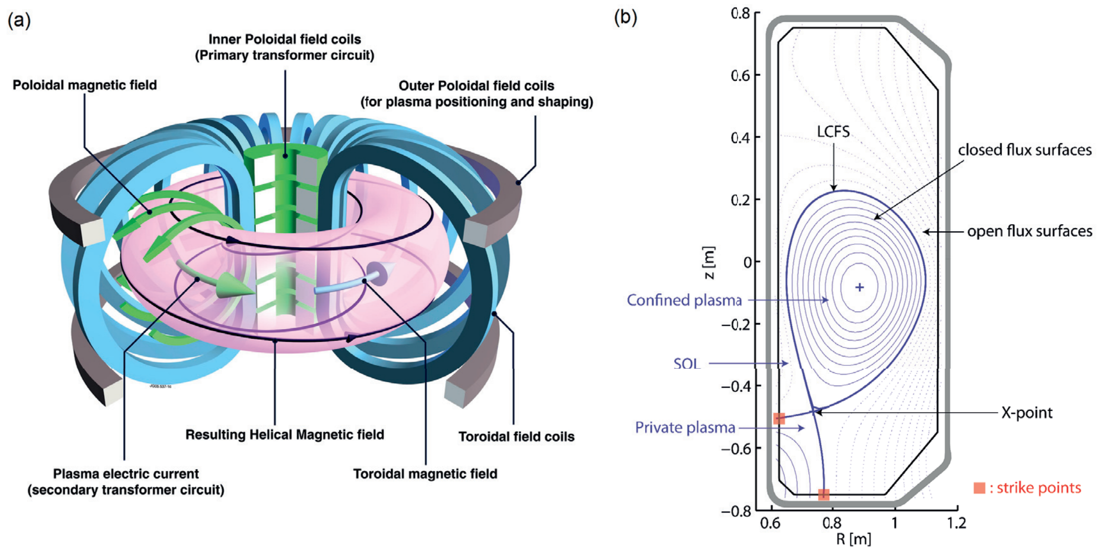

Figure 1.1: (a) Illustration of the tokamak configuration. *Source: EFDA-JET*. (b) Schematic view of the poloidal cross-section of a diverted plasma in TCV.

Various magnetic confinement schemes have been devised; one of the most successful approaches is the tokamak configuration. A schematic diagram of the magnetic configuration in a tokamak is shown in Fig. 1.1 (a). The plasma is confined inside a torus-shaped vacuum vessel. The main magnetic field component is in the toroidal direction, applied by a set of external toroidal field coils; a secondary poloidal field component is primarily generated by a toroidal plasma current driven by a central solenoid which serves as the primary transformer circuit, with external poloidal field coils also used to adjust the poloidal field for shape and position control. The combination of the toroidal and poloidal field components results in helical magnetic field lines, which are necessary for a stable equilibrium. These helical field lines form magnetic flux surfaces, on which the magnetic flux is constant.

The plasma is confined within closed magnetic flux surfaces, the last closed flux surface (LCFS) defining the shape of the plasma cross-section. The region outside the LCFS is called the scrape-off layer (SOL), where the magnetic field lines intersect the machine surface and cannot close on themselves. Cross-field transport will inevitably move particle and energy flux out of the LCFS into the SOL and finally dump them on at the machine wall. Generally there are two different kinds of LCFS geometries: the first one is obtained by simply inserting a solid material and the plasma is *limited* by this material called *limiter*; the other configuration is to use external poloidal field coils generating a poloidal field in opposition to the field generated by the plasma current, to create a null in the poloidal field called X-point, with a solid material used to cut through the flux surface created by the external current. The latter is called a *divertor* configuration. A poloidal cross-section of a *diverted* plasma in a tokamak is illustrated in Fig. 1.1 (b). The magnetic flux surface encompassing the X-point is called *separatrix*. The points at which the open flux surface directly connects to the solid surface are called *strike points* (divertor target). The region under the X-point inside the separatrix is called the *private region* of the SOL [9].

1.2 Motivation of the thesis

1.2.1 Plasma turbulence

One of the main goals of tokamak research is to investigate and possibly control the radial transport of particles and energy, which dramatically reduce the confinement time of the plasma, preventing it from reaching the Lawson criterion. The most fundamental transport is caused by diffusion induced by Coulomb collisions, called *classical* transport, which is in fact negligible compared to experimentally measured values. Enhanced transport induced by the toroidal geometry is known as *neoclassical* transport, which still predicts substantially lower levels of electron transport. The remaining additional transport is referred to as *anomalous*, and is widely accepted to be induced by plasma turbulence caused by non-linear coupling of microinstabilities, which consist of a broad class of modes at a microscopic scale, i.e. in the order of ion and electron Larmor radii.

An intuitive description of turbulent transport is as follows: A confined plasma is by definition far from a thermodynamic equilibrium, thus providing the free energy source for microinstabilities: this comes from the pressure and current gradients typically all across the plasma radius, and the non-Maxwellian nature of velocity distribution functions. These instabilities involve fluctuations in density $\tilde{n}$ and temperature $\tilde{T}$, as well as electric and magnetic field, which lead to fluctuating drift velocities $\tilde{v}$. When the density fluctuations $\tilde{n}$ are in phase with the velocity fluctuations $\tilde{v}$, a net particle flux Γ can develop, similarly for a net energy flux Q.

An important motivation behind the investigation of plasma turbulence under various plasma configurations is to tie the phenomenology of micro-turbulence to the macroscopic plasma properties, therefore providing a better understanding of these configurations. One item of interest particularly suited to TCV is to understand the effect of the shape of the plasma poloidal cross-section on the energy confinement. Previous work [10, 11, 7] has established that negative triangularity significantly improves the energy confinement and, for equal gradients, reduces the heat flux. An investigation of plasma turbulence at different triangularities was undertaken in the course of this thesis work with the purpose of furthering the understanding of this phenomenology.

1.2.2 Zonal flows and geodesic acoustic modes

One basic mechanism to stabilize the turbulence in tokamaks is to decorrelate the turbulent eddies by sheared $E \times B$ flows. An important example is the high confinement mode (H-mode), in which the plasma confinement is improved by approximately a factor of 2. In H-mode, a transport barrier with steep pressure gradient develops at the plasma edge, where a radial electric field with steep gradient is also localized, associated with sheared $E \times B$ flows. These sheared flows shear the turbulent eddies, thus reduce their radial correlation length, decorrelate and stabilize the turbulence, and finally reduce the anomalous transport, creating an edge transport barrier; the sheared flows therefore play a crucial role in the development of the enhanced confinement regime.

Besides the mean edge $E \times B$ flow, recent research has also noted the importance of fluctuating sheared $\tilde{E} \times B$ flows known as zonal flows in plasma turbulence. Zonal flows (ZF) are azimuthally symmetric band-like sheared flows that are widely observed in nature and the laboratory [12, 13, 14]. In the context of magnetized toroidal plasmas, zonal flows are sheared $\tilde{E} \times B$ flows associated with an electric field fluctuation which is constant on magnetic surfaces but varies perpendicularly with finite radial wave number. One important feature of zonal flows is that they are excited exclusively by non-linear interactions of all types of microinstabilities and can in turn suppress the turbulence amplitude through the shearing-decorrelation mechanism [15], and finally regulate the transport. Therefore turbulence and zonal flows form a self-regulating system described by a general predator-prey model, which has applications that go well beyond the specificities of thermonuclear fusion research. In addition, recent research suggests that zonal flow dynamics may also play a role in the L-H transition [16, 17, 18, 19, 20].

The geodesic acoustic mode (GAM) [21] is a finite frequency branch of the zonal flow. Its well defined frequency makes the GAMs much easier to detect and identify than the zero mean frequency zonal flows. The GAM frequency is predicted to depend on the ratio of the ion sound speed to the major radius R:

$$f = F\sqrt{2 + q^{-2}}\, c_{\mathrm{s}} / (2\pi R) \tag{1.3}$$

where c_{s} is defined as:

$$c_{\mathrm{s}} \approx \sqrt{(T_{\mathrm{e}} + T_{\mathrm{i}})/m_{\mathrm{i}}} \tag{1.4}$$

Here, T_e and T_i are the electron and ion temperatures, respectively, m_i is the ion mass, q is the safety factor, F is a coefficient of order unity which depends on plasma and shape parameters (especially elongation) [22, 23, 24].

The GAM frequency is by definition dependent on plasma temperature T, which is itself inhomogeneous in the radial direction in a confined plasma. Therefore, the GAMs often appear to be radially localized flows with a frequency continuum depending on the radial location, typically decreasing towards the plasma edge. Another regime has however also been identified in experiments, in which the GAM frequency is constant over a finite radial extent; some appear as multiple discrete coexisting modes [22, 25] or even one single-frequency global mode [26, 8, 27]. Possible candidate mechanism for the radially extended regime includes the GAM eigenmode due to finite ion Larmor radius effect [28], and also radial extension of a dominate component associated with the continuum GAM [29]. The conditions for these two regimes to occur and the transition between them, as well as their effects on turbulence are still not well understood and thus remain an active and interesting area of GAM investigation.

The GAM consists of a $\tilde{E} \times B$ flow component with toroidal mode number $n = 0$ and poloidal mode number $m = 0$, a pressure component with $n = 0$ and $m = 1$, as well as a recently discovered magnetic component which is found to be $n = 0$ and mainly $m = 2$ in both theory [30] and experiment [8]. In the course of this thesis GAM oscillations have also been detected in other fields, in particular for the first time as particle flux oscillations in the SOL by Langmuir probes. This new observation suggests a possible coupling between ZF/GAMs and avalanches [31], provides new considerations on the relation between ZF/GAMs and transport, and also couples the ZF/GAM physics to SOL and exhaust physics.

1.3 Thesis outline

The remainder of this thesis is organized as follows. The introduction (Chapter 1) is followed by a description of the experimental apparatus including the TCV tokamak and the diagnostics used in this work in Chapter 2. Special attention is given to the most important diagnostic in this work, the tangential phase contrast imaging (TPCI) diagnostic. Chapter 3 addresses the investigation of the dependence of turbulence - the density fluctuation component - on plasma shape, especially triangularity, and on collisionality, primarily using the TPCI diagnostic. Chapter 4 presents a characterization of the geodesic acoustic mode in TCV through multiple diagnostics. Finally, a summary is given in Chapter 5.

2 Experimental apparatus

In this chapter, the experimental apparatus used in this work will be described. Section 2.1 presents a brief overview of the Tokamak à Configuration Variable (TCV). Section 2.2 is dedicated to the main diagnostic used in the thesis: the Tangential phase contrast imaging (TPCI) diagnostic. In Section 2.3, some other diagnostics on TCV which are involved in this work are presented. Finally, the definition of several statistical techniques used to analyze the TPCI signals is provided in section 2.4.

2.1 The TCV Tokamak

The TCV tokamak [32] is a mid-sized tokamak operated since 1992 at the Swiss Plasma Center (SPC) of the Ecole Polytechnique Fédérale de Lausanne (EPFL), Switzerland. The major machine and plasma parameters are listed in table 2.1.

Parameter	Symbol	Value
Major radius	R_0	0.88 m
Minor radius	a	0.25 m
Vacuum vessel height	b	1.45 m
Toroidal magnetic field	B_T	≤ 1.54 T
Plasma current	I_p	≤ 1 MA
Elongation	κ	$0.9 \leq \kappa \leq 2.8$
Triangularity	δ	$-0.8 \leq \delta \leq 1$
Plasma density	n	$0.5 \times 10^{19} \leq n \leq 20 \times 10^{19}\ \mathrm{m}^{-3}$
Electron temperature	T_e	≤ 15 keV (with ECH)
Ion temperature	T_i	≤ 5 keV (with NBH)
ECH power	P_ECH	4.1 MW (2.8 MW X2 + 1.3 MW X3)
NBH power	P_NBH	1 MW
Energy confinement time	τ_E	≤ 50 ms

Table 2.1: Selected parameters of the TCV tokamak.

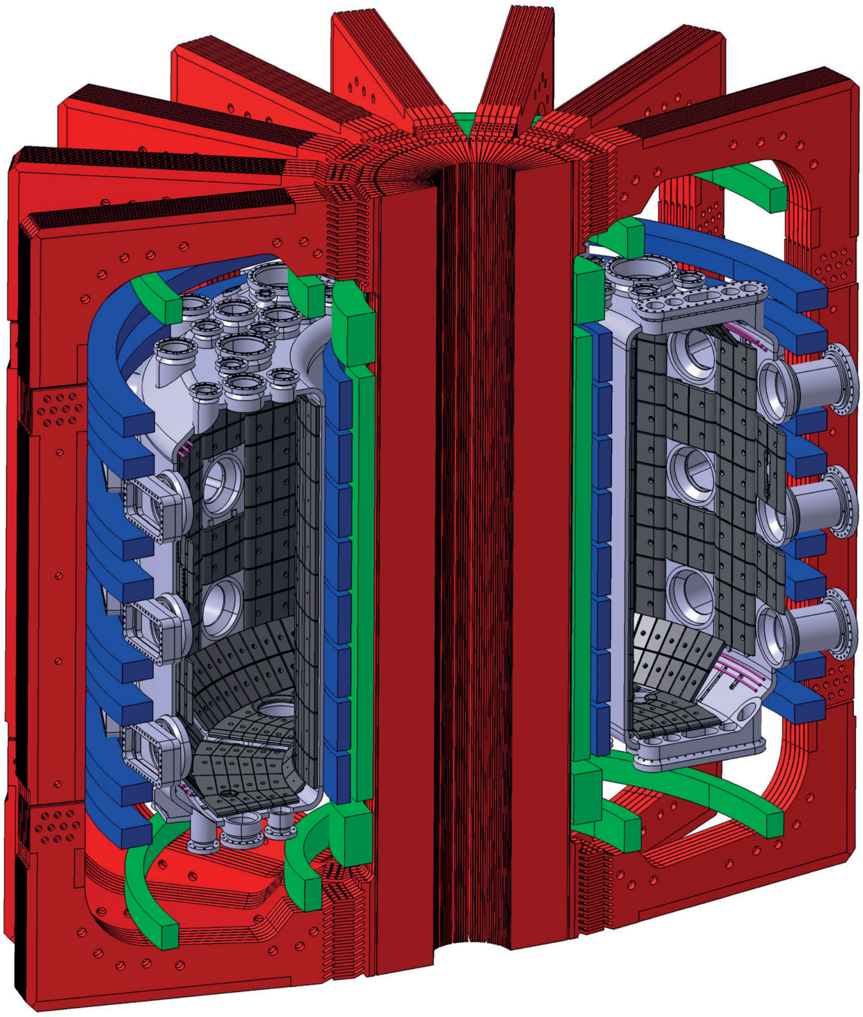

Figure 2.1: Schematic drawing of the TCV tokamak with the toroidal field coils (red), Ohmic coils (green), poloidal field coils (blue), internal fast coils (magenta), vacuum vessel (light gray) and first wall (dark gray). *Source: TCV 3D views by Matthieu Toussaint.*

As suggested by its name, the TCV tokamak is characterized by a high operational flexibility particularly in terms of plasma shapes. This is achieved by the fact that TCV has a highly elongated vacuum vessel and 16 independently powered poloidal field (PF) coils, as illustrated in Fig. 2.1. The unique shaping capability extends to limited and diverted plasmas. TCV is the only tokamak capable of creating negative triangularity plasmas and the snowflake divertor configurations.

Another unique feature of TCV is its electron cyclotron heating and current drive system [33]. The system features eight gyrotrons grouped in three clusters, with nominal output power ranging from 300 to 750 kW and a maximum duration of 2 s, as illustrated in Fig. 2.2.

Five of the gyrotrons in two clusters are operated at 82.7 GHz, corresponding to the second (X2) harmonic of the electron cyclotron frequency near $R = 0.9$ m with a nominal toroidal field

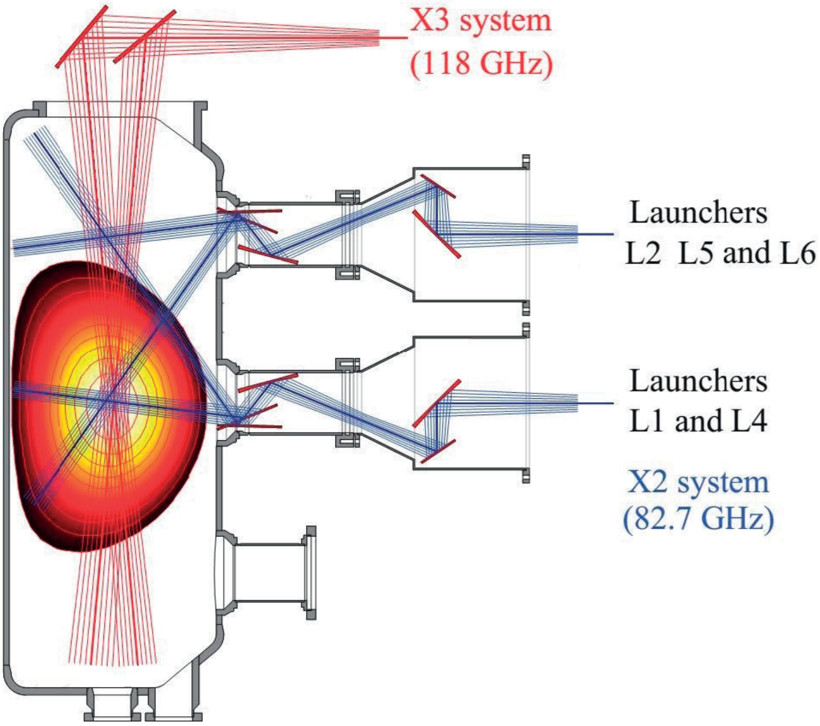

Figure 2.2: Schematic view of the TCV ECH launchers. The steering range in the poloidal plane is shown for X2 (blue) and X3 (red) microwave beams.

$B \approx 1.45$ T. The launching apparatus of the X2 system is composed of two launchers at the equatorial plane ($z = 0$ for L1 and L4), and three launchers at $z = 0.46$ m for L2, L5 and L6, through which the ECH microwave beams are injected into the plasma. Each X2 launcher has two degrees of freedom, allowing power deposition at arbitrary radius as well as non-inductive current drive. The cutoff density for central heating of the X2 system is about 4×10^{19} m^{-3}, restricting its use primarily to low density L-mode plasmas.

The third harmonic (X3) system at 118 GHz is used for heating high density plasmas such as H-mode discharges. The X3 microwave beam is delivered through one launcher from the top of the vessel to pass through the plasma almost parallel to the resonant layer to increase the absorption. The maximum density available for X3 heating on TCV is about 11×10^{19} m^{-3}.

2.2 The tangential phase contrast imaging diagnostic

The TPCI diagnostic [2] is the primary experimental tool for plasma turbulence investigations in this work. It measures small-scale, broadband turbulent density fluctuations, as well as coherent modes such as geodesic acoustic modes. This section will first briefly introduce the principles of phase-contrast imaging and the spatial filtering technique in Sec. 2.2.1, and then describe the experimental setup on TCV in Sec. 2.2.2. A more detailed version of the technique and of the diagnostic can be found in reference [34, 3, 2, 1].

2.2.1 Principles of phase-contrast imaging

Electromagnetic waves in a plasma

Consider a laser beam, i.e. an electromagnetic wave packet, traversing a plasma. For tokamak plasmas and infrared lasers, the wave frequency is much higher than the plasma frequency ($\omega >> \omega_{\mathrm{p}}$), which is defined as:

$$\omega_{\mathrm{p}}^2 = \frac{n_{\mathrm{e}} e^2}{\epsilon_0 m_{\mathrm{e}}} \tag{2.1}$$

where e is the electric charge, ϵ_0 is the permittivity of free space, m_{e} is the electron mass. Assume that the wave frequency is also sufficiently high that the magnetic field can be neglected ($\omega >> \omega_{\mathrm{c}}$), where $\omega_{\mathrm{c}} = eB_0/m_e$ is the electron cyclotron frequency and B_0 is the magnetic field. The refraction index of the plasma, i.e., the modifications to free space propagation of the electromagnetic waves, can be simply written as:

$$N = \frac{kc}{\omega} \approx 1 - \frac{\omega_{\mathrm{p}^2}}{2\omega^2} \tag{2.2}$$

Under the WKB approximation [35] that the scale length of the inhomogeneity is long compared to the wavelength, the phase shift that will be imparted upon the laser beam traversing the plasma can be calculated from the definition of plasma frequency (Eq. 2.1):

$$\phi = k_0 \int N(x)\,\mathrm{d}x = r_{\mathrm{e}} \lambda_0 \int n_{\mathrm{e}}\,\mathrm{d}x \tag{2.3}$$

Here r_{e} is the classical electron radius:

$$r_{\mathrm{e}} = \frac{1}{4\pi\epsilon_0} \frac{e^2}{m_{\mathrm{e}} c^2} \; (\approx 2.818 \times 10^{-15}\ \mathrm{m}) \tag{2.4}$$

where k_0 and λ_0 are the wave number and wavelength of the laser beam; n_{e} and m_{e} are the electron density and mass, respectively; x is the spatial coordinate along the beam path. Various plasma diagnostics based on the interferometry technique have been developed based on the plasma's refractive index properties, such as the Far infrared interferometer (FIR) on TCV for line-integrated density measurements [36].

Phase contrast

The phase contrast imaging method, first proposed by Zernike [37], is an internal reference interferometer that transforms the phase variations into amplitude ones. An optical system based on the phase contrast method can then be established to create an image of the line-integrated density fluctuations. A schematic illustration of the phase contrast imaging technique is shown in Fig. 2.3 [1].

The total phase shift of an electromagnetic wave traversing a plasma can be written as the sum of a static and a fluctuating component:

$$\phi = \phi_0 + \tilde{\phi} \tag{2.5}$$

where the former is induced by the equilibrium plasma density and the latter by its fluctuations. The electric field of the scattered wave can be represented by:

$$E_\mathrm{s} = E_\mathrm{i} \mathrm{e}^{i(\phi_0+\tilde{\phi})} = E_0 \mathrm{e}^{i\tilde{\phi}} \approx E_0(1 + i\tilde{\phi}) \tag{2.6}$$

where E_i is the electric field of the initial wave, E_0 is the electric field of the "undiffracted" component of the beam, which contains the phase shift ϕ_0 induced by the equilibrium plasma density, and the last equality holds only if the fluctuating component is small. If it were possible to separate the undiffracted and diffracted components and add an additional 90° phase shift between them, the scattered electric field would become:

$$E_\mathrm{s} = iE_0(\pm 1 + \tilde{\phi}) \tag{2.7}$$

Therefore the measured amplitude signal from a detector would become:

$$|E_\mathrm{s}|^2 = |E_0|^2 (1 + 2\tilde{\phi}) \tag{2.8}$$

Finally the measured fluctuating component is linearly proportional to the original density fluctuation.

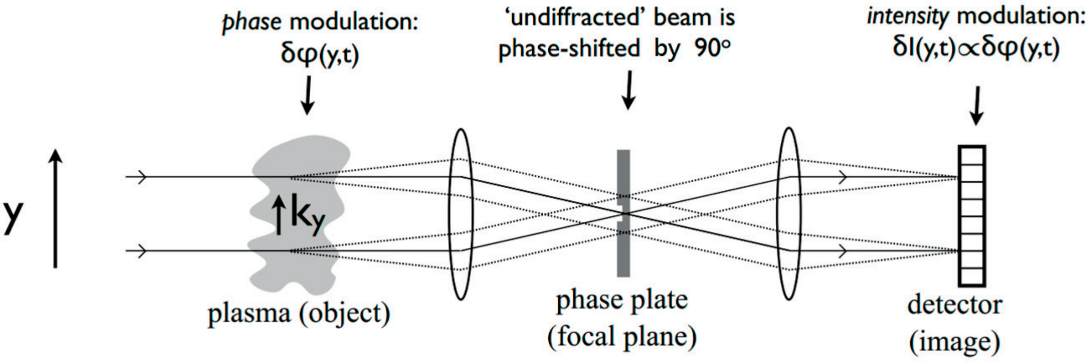

Figure 2.3: Principle of phase-contrast imaging. Solid and dashed rays correspond to the undiffracted and diffracted components, respectively. [1]

These two components can be physically separated by focusing the scattered beam, so that the undiffracted component will be focused on axis, while the scattered component by density fluctuations with wave number k will be focused off-axis on the focal plane at:

$$y = Fk/k_0 \tag{2.9}$$

where F is the effective focal length, k_0 is the wave number of the laser beam. A transmitting/reflecting phase-contrast filter is placed in the focal plane, introducing a quarter-wavelength shift between the two components. This can be achieved simply by adding a 1/4-wavelength-deep (1/8 in case of reflecting filter) groove at the center of the phase-contrast filter [38, 39].

Response function of the phase plate

In case of an infinite plane wave, the response function of the phase plate is that of a high-pass filter in wave number space; the cutoff wave number k_c can be easily calculated from Eq. 2.9 to be defined by the half-width d of the phase-plate groove:

$$k_\mathrm{c} = k_0 d/F \tag{2.10}$$

The highest resolvable wave number is defined by the condition that the diffraction needs to be within the Raman-Nath regime:

$$k^2 < \frac{\pi k_0}{L} \tag{2.11}$$

In the Raman-Nath regime, the geometric optic approximation is valid, and the total phase shift from the entire integration length L can be assumed to arise from a single thin layer which introduces an instantaneous phase shift given by the line-integrated density.

In the experiment, the signal from each detector element is proportional to the light intensity integrated over the area, and therefore the fluctuations with too short wavelength would be averaged out. The highest achievable wave number is thus also limited by the finite size of the detector elements.

For a finite-width wave, the focal spot has a finite size because of diffraction effects. If the incident wave is Gaussian with amplitude half-width w_0, the focal spot is also Gaussian with half-width $\lambda_0 F/(\pi w_0)$. The response function for such a Gaussian beam and aperture stop of radius a can be found out to be:

$$T(\mathbf{K}) = 2\sqrt{\rho}\,u_0(0)\int_{-a}^{+a}\frac{\sin(k_\mathrm{c}x)}{\pi x}e^{-x^2/w_0^2}[1-\cos(K_\mathrm{x}x)]\,\mathrm{d}x \tag{2.12}$$

Here $u_0(0) = 2P/(\pi M^2 w_0^2)$ is the dc power flux in the center of the image; ρ is the reflectivity of the phase-plate groove which can attenuate the undiffracted component and thus improve the contrast between the fluctuating component and the local oscillator. The detected signal will become:

$$|E_\mathrm{s}|^2 = |E_0|^2(\rho + 2\sqrt{\rho}\tilde{\phi}) \tag{2.13}$$

enhancing the contrast by a factor $\sqrt{\rho}$.

An optimization of the response function $T(\mathbf{K})$ can be made for the two dimensionless parameters $Q = k_c w_0/2$ and $\alpha = w_0/a$, so that the signal level is sufficiently high throughout the image and the transfer function is sufficiently smooth over a wide range of $\mathbf{K}$. This yields

$Q \approx 1.4 - 1.8$ and $\alpha \approx 1$ [34]. An example is shown in Fig. 2.4 for a ZnSe phase plate used in experiments, with $Q = 1.26$ and $\alpha = 1$.

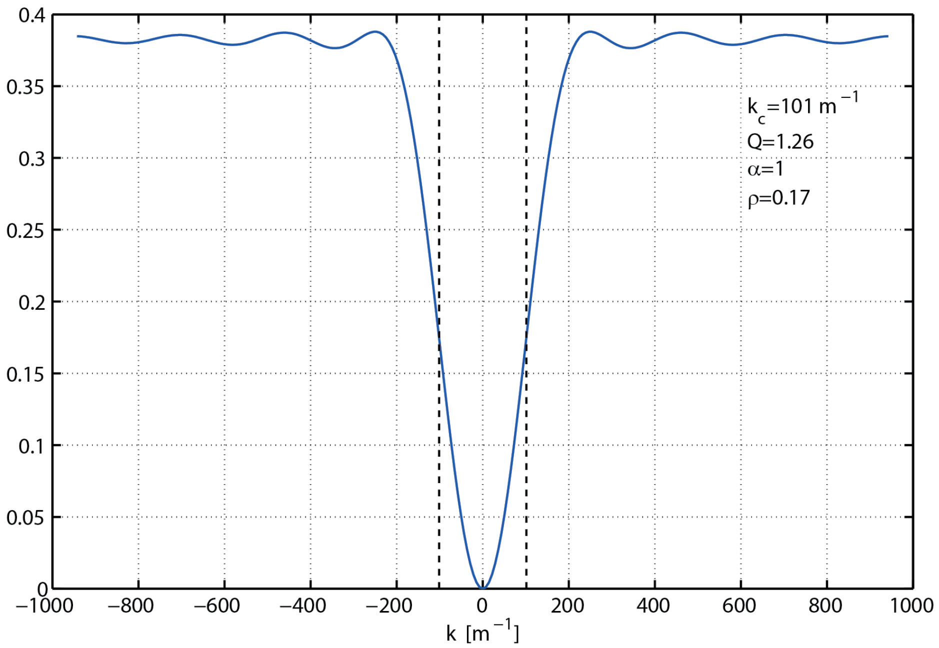

Figure 2.4: Optical response function of a ZnSe phase plate (with metallic coating outside the groove) with groove half-width $d = 200\ \mu$m and reflectivity $\rho = 0.17$ used in TCV experiments.

The response function is zero at $k = 0$ and with the 1/e point at approximately k_c. It is essentially flat from $2k_c$ to the Raman-Nath limit. Therefore, for sufficiently short structures, it is a true imaging system of the density fluctuations.

Spatial filtering

Phase-contrast imaging is intrinsically a line-integrated measurement along the laser beam path, and therefore has no longitudinal resolution. However, it is still possible to obtain a localized measurement along the chord, by exploiting the geometry of the magnetic field.
As all line-integrated methods, PCI is only sensitive to fluctuations with wave-vectors $\mathbf{k}$ perpendicular to the laser beam wave-vector $\mathbf{k}_0$. In addition, it is widely accepted that density fluctuations in a magnetized plasma are elongated along the magnetic field lines, i.e. $\mathbf{k}_\parallel \ll \mathbf{k}_\perp$, which leads to the criterion $\mathbf{k} \perp \mathbf{B}$. Combining the two criteria leads to the selection rule:

$$\mathbf{k} \parallel \mathbf{k}_0 \times \mathbf{B} \tag{2.14}$$

The direction of the magnetic field varies along the laser beam path, thus at each location along the beam path a precise angle of measured fluctuation wave-vector can be identified, as shown in Fig. 2.5 (a).

This angle can be selected by spatial filtering on the focal plane. With a tangential beam geometry, such as the one employed in TCV, the angle is a single-valued, monotonic and steep function of a linear coordinate along the beam path, as seen in Fig. 2.5 (c); it is then possible to select an effective integration length which is much shorter than the entire beam path by choosing the corresponding fluctuation angle. The steepness of the angle function is primarily caused by the curvature of the toroidal magnetic field, and is only weakly affected by the magnetic shear [2].

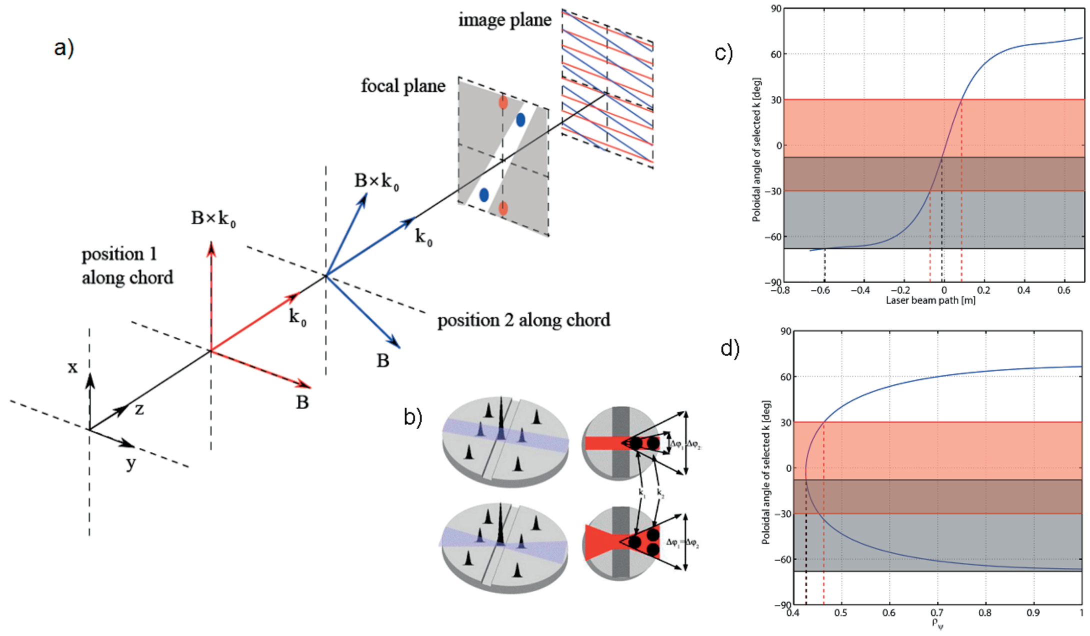

Figure 2.5: (a) The principle of longitudinal localization of a line-integrated measurement using the wave-vector selection rule $\mathbf{k} \parallel \mathbf{k}_0 \times \mathbf{B}$ [1]. (b) Fluctuation direction selection by means of a spatial filter [2]. (c,d): Selected fluctuation angle as a function of linear beam path and radial position, respectively. The red and the gray region denote the cases of good and bad radial resolution, respectively.

The focal spot of the laser beam has finite dimensions due to diffraction, so that the spatial filter must have a finite width, which translates into the angular range of fluctuation wave-vector selection. For a Gaussian beam with amplitude half-width w_0, the resulting angular resolution is:

$$\Delta\alpha = 2\arctan(2/kw_0) \tag{2.15}$$

It can be seen from Eq. 2.15 that the angular resolution improves with k. This means that for a rectangular shaped spatial filter, the resolution is optimized for all wave numbers, but it is not uniform, i.e. the selected length is shorter for high k. An alternative path is to use a wedge shaped filter, the angular resolution is being then the same for all k, and the achievable resolution being determined by the cutoff wave number k_c. These two spatial filter versions can be seen in Fig. 2.5 (b). An optimized configuration [3] for the TPCI system on TCV gives a

resolution approximately 60°.
Figure 2.5 (c) shows the selected fluctuation angle as a function of laser beam path. The angular function is steepest near the tangent point between the magnetic surface and laser wave-vector, where with a 60° wedge shaped spatial filter the effective integration length can be reduced to the order of tens of centimeters. In addition, a significant fraction of the laser beam path stays close to the magnetic surface near the tangent point, thus the linear coordinate along the beam path is also a steep function of radial coordinate ρ. This secondary effect again enhances the radial localization at this point, as shown in Fig. 2.5 (d). The optimized radial resolution can reach down to 1% of the minor radius.

2.2.2 The TPCI system on the TCV tokamak

Laser

The measurement laser is a RF excited waveguide CO_2 laser (Edinburgh Instruments model WL-8) with 28 THz frequency (10.6 μm wavelength).The nominal output power of the laser is 8 W, however the measured value is 6 W on average and 7 W maximum. It has 1.3 mm full Gaussian width and the full divergence is quoted as 9 mrad while the measured value is 18 mrad. The vertical polarization is ±5°. It is water cooled by a Neslab chiller to support continuous operation at $15°C$.
A visible laser (Scitec model SDL-635-LM-100T) with 635 nm wavelength and 100 mW power is co-aligned with the main measurement infrared laser for easy alignment. It first passes through a tunable telescope to match the divergence of the measurement laser.

Optical beam path

The two co-linear laser beams are first expanded to a collimated beam through a refractive-reflective telescope configuration. The beam's full Gaussian diameter is set to be $5-6$ cm in most of this work to avoid clipping in the narrowest part of the beam path. The telescope consists of a plano-convex ZnSe lens (L11) with $f = 38.1$ cm and an off-axis parabolic mirror (M20) with $f = 1.905$ m.
The expanded collimated beam is then sent into the tokamak through an entry assembly at the equatorial port in sector 1 of TCV. The entry assembly consists of three elliptical mirrors (M1-3) with the last two inside vacuum behind a ZnSe window (W1). The beam is sent tangentially with a 19° upward angle and exits the tokamak through the exit assembly at the upper lateral port in sector 14 of TCV. The exit assembly consists of two elliptical mirrors (M4-5) both in vacuum behind a ZnSe window (W2). In each port the normals to the mirrors lie in a single plane. The toroidal separation between the entry and exit ports is $3\pi/8$. Both the entry and exit assemblies can be shifted radially, the innermost position allowing the innermost mirrors on the entry and exit assemblies (M3 and M4) to protrude ~ 6 cm and ~ 2 cm beyond the protection tiles, respectively. A schematic drawing of the two assemblies is shown in Fig. 2.6.
After the beam leaves TCV, it propagates onto an off-axis parabolic mirror (M10) with $f =$

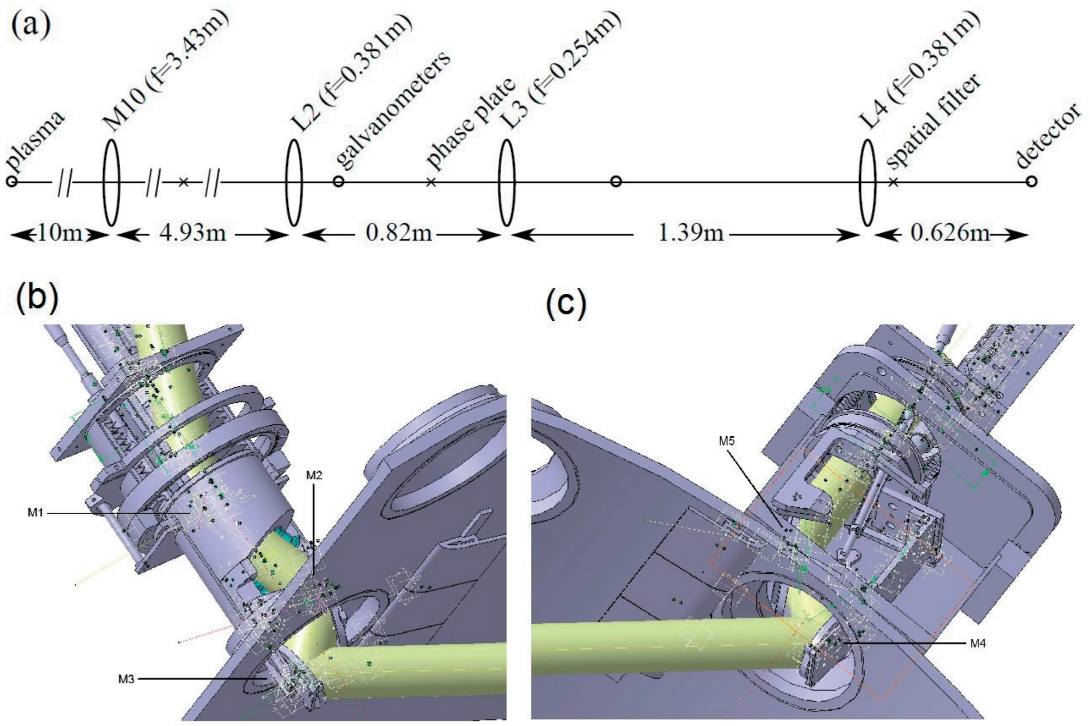

Figure 2.6: (a) Schematic drawing of the TPCI beam path [1]. CATIA drawing of the entry (a) and exit (b) ports [3]. The beam trajectory is in yellow.

3.454 m, large enough ($d = 37$ cm) to collect all the light scattered by the plasma at the highest wave numbers of interest. Relay lenses are used after the large parabolic mirror to reduce the effective focal length. The first lens (L2)with $f = 38.1$ cm after M10 creates the focal plane for the phase plate with effective focal length 1.17 m. After the phase plate the beam propagates through two other lenses: L3 with $f = 25.4$ cm and L4 with $f = 38.1$ cm; a second focal point is created after L4 and this is used for the spatial filter. The positions of L3 and L4 can be moved for different magnifications. Finally the detector is at the image plane created by L4.

A beam splitter is used after L2 and before the phase plate to split a small portion of the beam for the feedback vibration control system [34]. A quadrant detector (Infrared Ass.) consisting of four photoresistive HgCdTe elements is used as the position sensor to detect the position error on two axes. The error signals then enter the compensation circuit and the output signals are used to correct the position on the phase plate through two scanning mirrors mounted on galvanometers. The scanning mirrors are located in the image plane created by L2 before the phase plate. A detailed description of the feedback vibration control system can be found in ref. [1].

In-vessel geometry of the measurement

The toroidal and poloidal projections of the in-vessel laser beam path are illustrated in Fig. 2.7. For most experiments performed in this work, the radial positions of the entry and exit mirrors are at the positions where the tips of the innermost mirrors (M3 and M4, respectively) are flush with the protection tiles so that the mirrors will not be damaged by the plasma. In this configuration, the minimum major radius reached by the central chord of the laser beam (at the middle point of the in-vessel beam path) is $R = 0.95$ m, while the magnetic axis of a typical TCV plasma is at $R_0 \approx 0.89$ m.

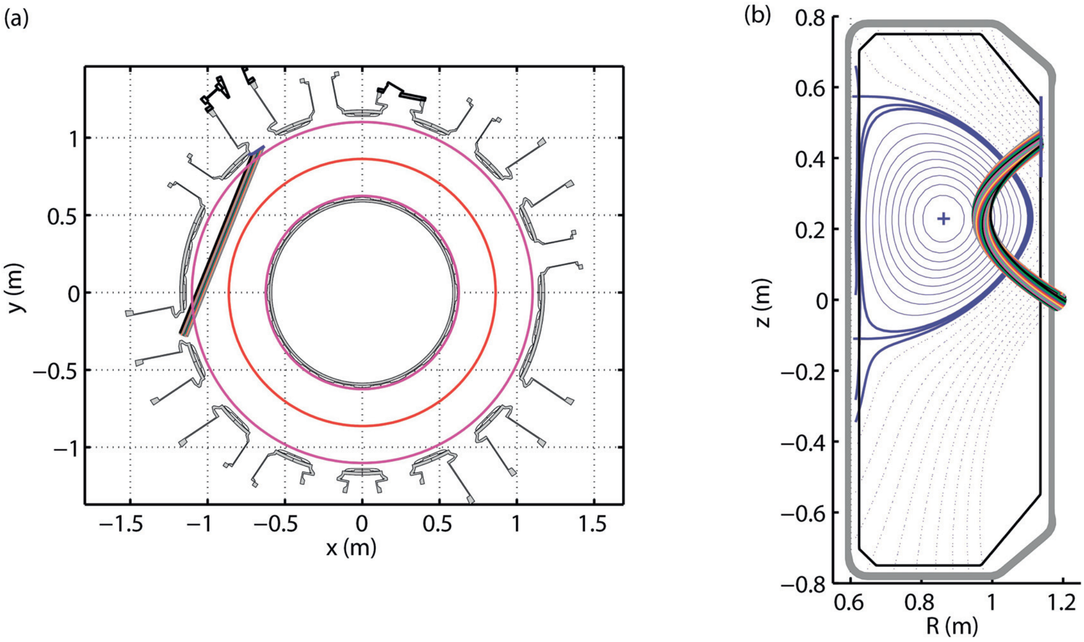

Figure 2.7: Schematic drawing of the top view (a) and the poloidal projection (b) of the TPCI laser beam inside the TCV vessel. The red line is the magnetic axis, the magenta lines are the plasma boundaries.

Thanks to the unique flexibility in terms of plasma shapes and positions of the TCV tokamak, the radial range of measurement can be greatly expanded by vertically shifting the plasma, allowing radially localized measurements from the core plasma to the edge, as shown in Fig. 2.8 (a): the magnetic axis of the plasma is at $R = 0.87$ m; the vertical position of the plasma shifting from $z = 0.23$ m to $z = 0$ m results in the radial position of the central chord going from $\rho_\psi = 0.5$ to 0.9 in flux coordinate.

The vertical shift of the plasma also changes the selected fluctuation wave-vector (see Eq. 2.14). By rotating the spatial filter to keep the selected wave-vectors centered around the tangent point, radially localized measurements can be achieved throughout the plasma, as shown in Fig. 2.8 (a). Fig. 2.8 (b) shows that even with the coarse angular resolution 60°, the radial resolution at the tangent point is in the range $0.01 - 0.05$. The wave-vector selected at the tangent point is always purely in the radial direction, as shown in Fig. 2.8 (c). On the other

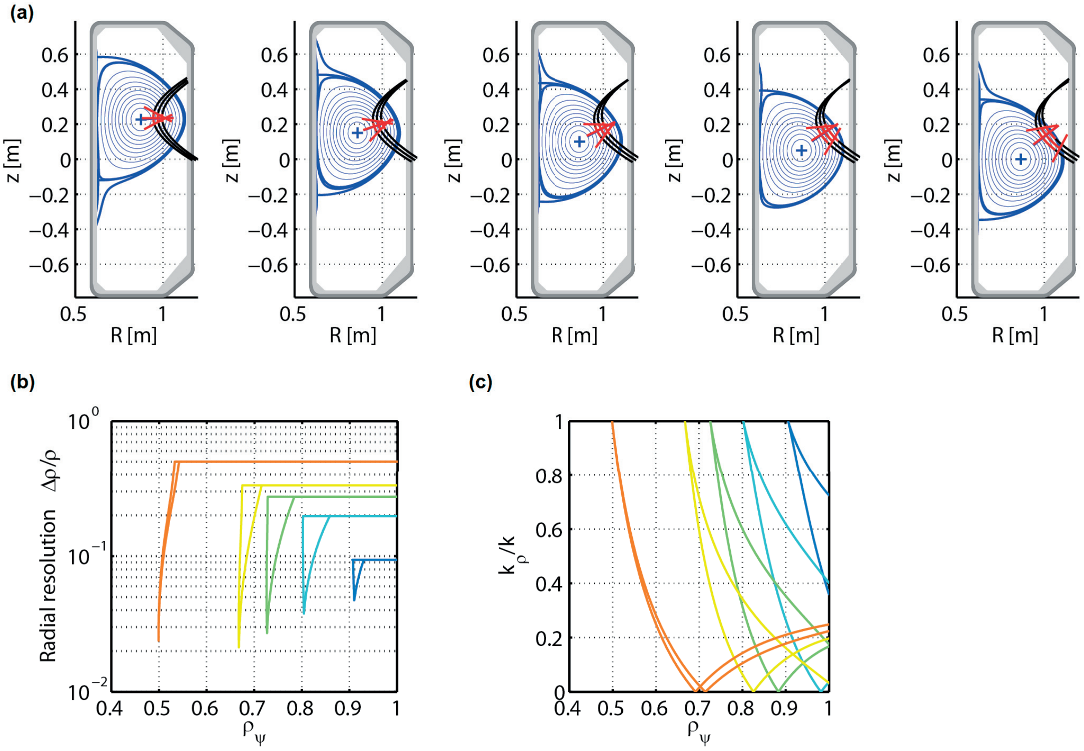

Figure 2.8: (a) Schematic of TPCI measurement geometry from core plasma to the edge by vertically shifting the plasma. The black lines illustrate the laser beam path, the region selected by the spatial filter is highlighted in red. (b) Radial resolution expressed as $\Delta\rho/\rho$ as a function of ρ itself. (c) Expected ρ component of measured fluctuating wave-vector (absolute value).

hand, the radial resolution is poor away from the tangent point.

Detectors and data acquisition

A linear array of 30 photoconductive HgCdTe elements (Infrared Associates) is used for the image detection, although only 9 unevenly spaced elements were still operational during the thesis work. Each element is a square with sides of length 250 μm and the space between elements is 50 μm. For a 5 cm full Gaussian diameter beam, it limits the Nyquist spatial frequency to be in the ion scale range $k_N = 9.4$ cm^{-1}, well below the Raman-Nath regime limit $k < 60$ cm^{-1} (see Sec. 2.2.1). The bandwidth is rated at 1.6 MHz without experimental verification.

Signals from the detector array are amplified by a preamplifier array with 61 dB gain and a passband of 7 kHz – 3 MHz [3]. The output signals from the preamplifiers are digitized by two 16-channel ADCs (D-Tacq model ACQ216) with sampling rate 12 MHz and a built-in 5 MHz anti-aliasing filter. The maximum acquisition time is 2.6 s which covers a typical TCV discharge.

2.3 Other diagnostics on TCV

2.3.1 Magnetic probes

In TCV, the magnetic measurements are performed using pick-up coils (magnetic probes), which measure the electric field induced by the time derivative of the magnetic field along the probe axis. The probes are aligned with the vessel wall between the wall and the graphite tiles [4]. The magnetic field measurements are used for the magnetic equilibrium reconstruction performed using the LIUQE code [40] and are also a fundamental part of the real time control system of the plasma position and shape. The probes are located inside the vacuum vessel, so the time resolution is not limited by the magnetic diffusion time of the conducting vessel. Their fast frequency response (> 100 kHz) and the fact that they are absolutely calibrated make the probes suitable for studying MHD phenomena. In this work, the magnetic probes are also used to study the magnetic oscillation component of the GAMs.

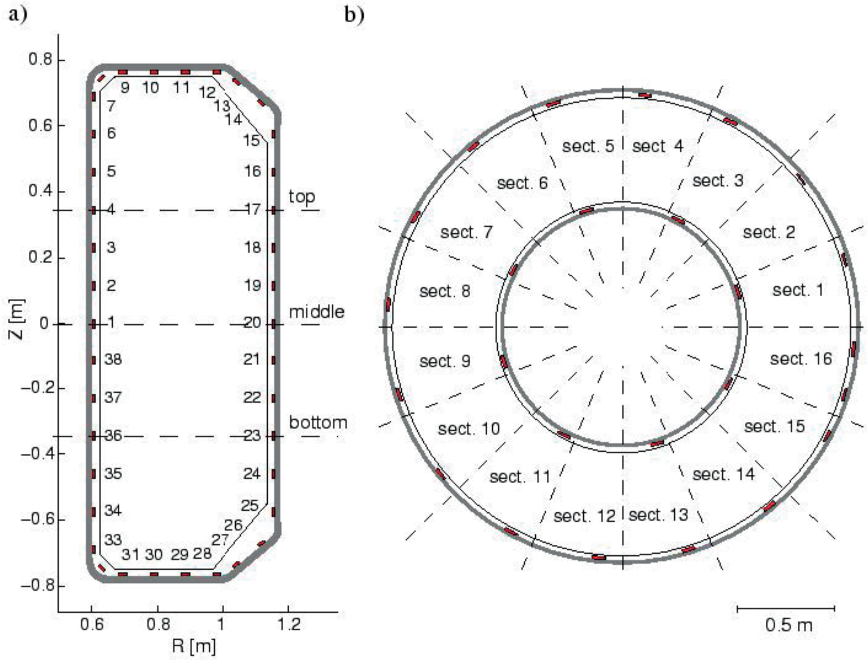

Figure 2.9: Layout of the magnetic probes on the poloidal (a) and toroidal (b) cross-sections of the TCV vessel [4].

Currently 203 magnetic probes arranged in poloidal and toroidal arrays are installed on TCV, as shown (partly) in Figure 2.9. Three pairs of toroidal arrays are installed at the mid-plane of the vacuum vessel, and 35 cm above and below it, respectively. Each pair includes 8 magnetic probes on the high field side (HFS) and 16 probes on the low field side (LFS) located at equidistant toroidal angles. Four poloidal arrays at four poloidal cross sections toroidally separated by 90° are equipped with 38 almost evenly spaced magnetic probes each.

2.3.2 Doppler backscattering system

The Doppler backscattering system is a fluctuation diagnostic that can be used to measure density fluctuations as well as the perpendicular flow velocity. This is achieved by deliberately tilting a standard reflectometer with an angle θ to the plasma density gradient/cutoff layer normal, as shown in Fig. 2.10. The microwave beam is refracted as it propagates into the plasma $k_\mathrm{i}^2 = N^2 k_0^2$, and eventually reaches the cutoff where it is reflected. Consider a slab geometry, for normal incidence the cutoff layer is at $N = 0$ where the local probing wave number $k_\mathrm{i} = 0$, however for a tilted wave front the cutoff layer is at $N^2 = \sin^2\theta$ where $k_\mathrm{i} = k_0 \sin\theta$, i.e., the component parallel to the cutoff layer. Backscattering of the probing beam happens when there are density fluctuations with wave number satisfying the Bragg condition:

$$k = -2k_\mathrm{i} = -2k_0 \sin\theta \tag{2.16}$$

If the fluctuations propagates with a velocity $\mathbf{v}$, the returning microwave frequency spectrum is modulated by a Doppler shift:

$$\delta\omega = \mathbf{v}\cdot\mathbf{k} \tag{2.17}$$

We recall that the wave-vector of density fluctuations in a magnetized plasma is perpendicular to the magnetic field $\mathbf{k} \perp \mathbf{B}$, therefore the Doppler shift $\delta\omega$ results only from the velocity component perpendicular to the magnetic field, i.e., in the $E\times B$ velocity direction. The velocity consists of two components: the $E \times B$ velocity and the phase velocity of the fluctuations:

$$v_\perp = v_{E\times B} + v_\mathrm{ph} \tag{2.18}$$

Gyrokinetic simulations confirm that the phase velocity of the turbulence in tokamaks is usually much smaller than the $E \times B$ velocity and thus can be neglected in the Doppler shift. This allows one to use the turbulence as a tracer to measure the $E \times B$ flow velocity and its fluctuations, such as zonal flows and GAMs. However, in experiment, non-negligible phase velocities have been measured [41, 42].

TCV has had on loan at different times various heterodyne Doppler backscattering systems, including a tunable instrument between 50 and 75 GHz (V-band) from Laboratoire de Physique des Plasmas (LPP) [43] and a 45 GHz (U-band) instrument from Forschungszentrum Julich (FZJ), coupled to a monostatic steerable antenna which is a replica of the ECH launchers. In the experiments before 2014, this diagnostic launcher was at $z = 0$, while in 2016 after the TCV upgrade, it was moved to $z = 0.46$ m.

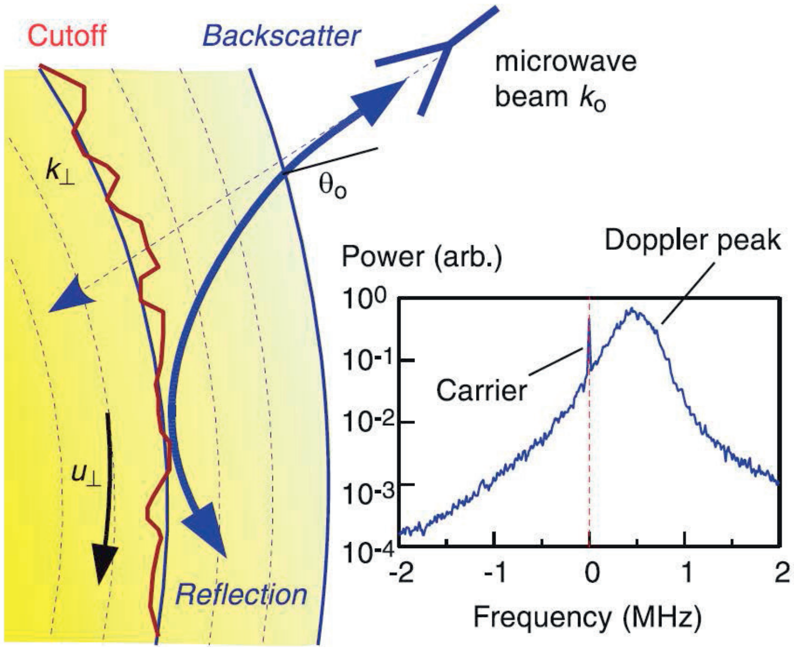

Figure 2.10: Schematic drawing of principle of Doppler backscattering on the left and a typical Doppler shifted spectrum from the DBS system on the right [5].

2.3.3 ECE diagnostics

The electron cyclotron emission (ECE) radiometers are used on TCV to measure electron temperature profiles, based on the fact that the electron cyclotron frequency is proportional to the magnetic field strength and hence to the radial position in the tokamak. A schematic drawing of the ECE system on TCV is shown in Fig. 2.11. Two horizontal lines-of-sight are installed inside the chamber on the central column at $z = 0$ and $z = 21$ cm on both the HFS and LFS. The total frequency bandwidth is 78 – 118 GHz for the HFS and 65 – 100 GHz for the LFS with full coverage of the vessel, notch filters are used to prevent the 82.7 GHz X2 ECH signals affecting the measurements. The bandwidth of each channel is 750 MHz, which corresponds to ~ 1 cm spatial resolution in major radius. Alternatively, the steerable antenna described above, shared with the DBS system with smaller spot size, can be used for oblique measurements.

A correlation ECE (cECE) system is used for the measurement of electron temperature fluctuations $\tilde{T}_e$. The working principle relies on the spectral decorrelation properties of the thermal EC emission, i.e., that the micro-scale $\tilde{T}_e$ components of the signals from two close channels are correlated while the thermal noise components are not. The cECE system on TCV can cover the frequency intervals between 67 – 79 GHz or 88 – 100 GHz depending on the chosen mixer. In this work, the cECE diagnostic is used to measure the temperature oscillation component of the GAM.

For both ECE and cECE system, a sufficient optical thickness of the EC emission volume is required for the measurements. However, the optical thickness at the edge of relatively

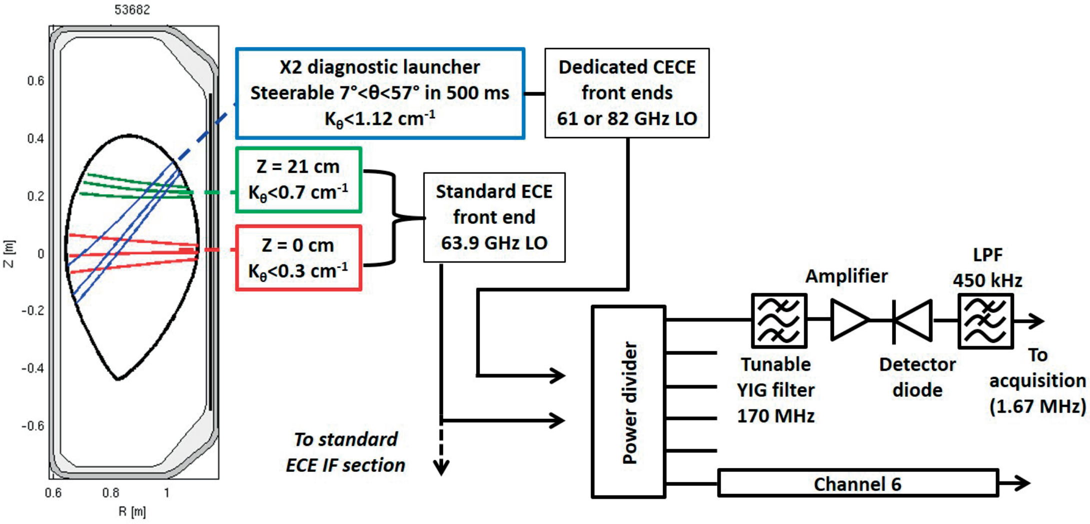

Figure 2.11: Schematic drawing of current ECE system on TCV. *Source: Matteo Fontana.* Currently the two lateral receivers at LFS are typically used for standard ECE, whereas the steerable launcher is dedicated for correlation ECE.

low density TCV plasmas is often low. This reduces the localization of temperature measurement, also causing the measured cECE fluctuation signal to be a mixture of $\tilde{T}_e$ and $\tilde{n}_e$. Therefore, careful treatment is required for measurements at the plasma edge such as in the GAM experiments.

2.3.4 Langmuir probes

The Langmuir probe is one of the most fundamental plasma diagnostics, originally developed by I. Langmuir and H. M. Mott-Smith. It is essentially an electrode immersed in the plasma and connected to a power supply capable of applying a bias voltage V_b. The dependence of the current received from the probe I on the biasing voltage yields the $I - V_b$ characteristic curve shown in Fig. 2.12.

When the Langmuir probe is biased with a large negative voltage, the electrons are strongly repelled while the ions are attracted by the probe. In this range the current is mainly composed of ion flux and is called the *ion saturation current*. According to the Bohm criterion, the ion saturation current is determined by:

$$I_{\mathrm{i,sat}} = eZn_{\mathrm{i,s}}c_{\mathrm{s}}A_{\mathrm{probe}} = 0.606eZn\sqrt{\frac{T_{\mathrm{e}}}{m_{\mathrm{i}}}}A_{\mathrm{probe}} \tag{2.19}$$

where eZ presents the ion charge; c_s is the ion sound speed; $n_{i,s}$ is the ion density at the sheath boundary which is equal to $0.606n$ with n being the plasma density before the pre-sheath; A_{probe} is the effective probe surface.

In contrast, when the biasing voltage is larger than the plasma potential $V_b \geq V_p$, the electrons

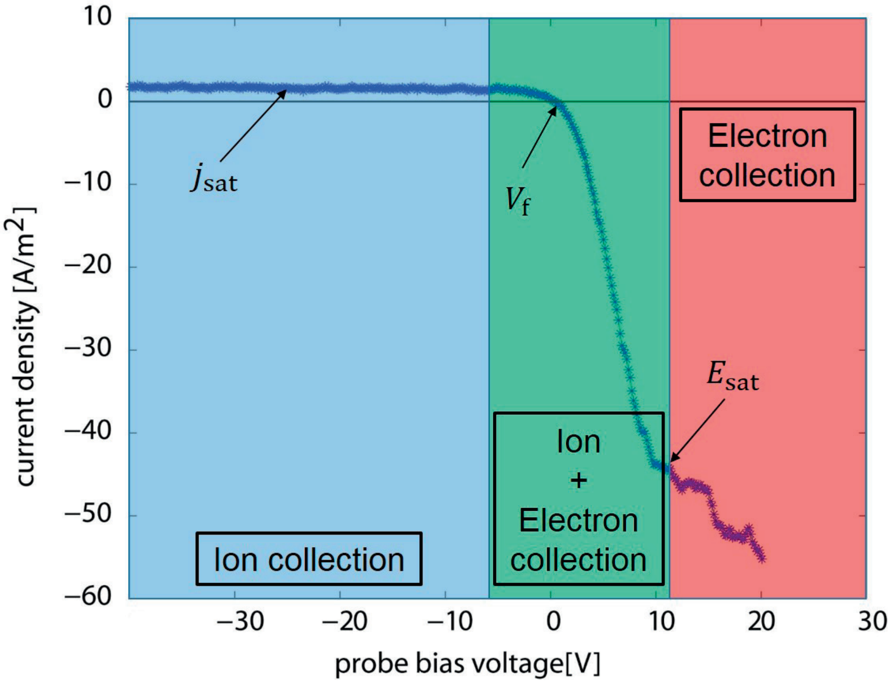

Figure 2.12: Schematic of a I-V characteristic curve obtained from a Langmuir probe. *Source: Plasma diagnostics course by Ivo Furno.*

dominate electric shielding of the probe. The *electron saturation current* can be estimated from the unidirectional electron flux:

$$I_{\mathrm{e,sat}} = \frac{1}{4} ne\bar{c}_{\mathrm{e}} = ne\sqrt{\frac{kT_{\mathrm{e}}}{2\pi m_{\mathrm{e}}}} A_{\mathrm{probe}} \tag{2.20}$$

For a biasing voltage $V_{\mathrm{b}} \le V_{\mathrm{p}}$ but not too negative, the current is composed of both electron and ion contributions. The electron contribution comes from those whose kinetic energy is larger than the electric potential difference $V_{\mathrm{b}} - V_{\mathrm{p}}$. Therefore, assuming a Maxwellian electron velocity distribution and unit ion charge $Z = 1$, the probe current in this region is:

$$\begin{aligned} I_{\mathrm{probe}} &= I_{\mathrm{i,sat}} + I_{\mathrm{e,sat}} \exp\left[\frac{e(V_{\mathrm{b}} - V_{\mathrm{p}})}{kT_{\mathrm{e}}}\right] \\ &= I_{\mathrm{i,sat}} \left\{1 - \exp\left[\frac{e(V_{\mathrm{b}} - V_{\mathrm{fl}})}{kT_{\mathrm{e}}}\right]\right\} \end{aligned} \tag{2.21}$$

Here V_{fl} is the floating voltage, defined as the biasing voltage with which the net current from the probe is zero. The relation between the floating and plasma voltage is:

$$V_{\mathrm{p}} = V_{\mathrm{f}} + \Lambda \frac{T_{\mathrm{e}}}{e} \tag{2.22}$$

where Λ is typically 3 for hydrogen or helium, but it should be determined experimentally since the magnetic field would affect the electron saturation current.

The temperature can be interpreted by fitting the measured Langmuir probe I-V characteristic curve with Eq. 2.21, and the density flux can be obtained from Eq. 2.19 with the probe in ion saturation mode. Modifications are required to consider the effect of sheath expansion and secondary electron emission.

TCV has 96 wall-mounted Langmuir probes, located on the floor and both the HFS and LFS wall of the vacuum vessel. The layout of this Langmuir probe set allows measurements with sweeping strike points from the HFS to the LFS, poloidal flux expansion scans, X-point target divertor, super-X divertor and snowflake divertor. The spatial separation of the probes is approximately $1-2$ cm depending on the location. In this work, Langmuir probes are used to measure the GAM oscillations in the ion saturation current, with each Langmuir probe biased to a constant -100 V to measure $I_{\mathrm{i,sat}}$.

2.3.5 D_α emission photodiodes

The D_α photodiodes measure the line radiation produced by the excitation of $D^{\mathrm{n=3}}$ to $D^{\mathrm{n=2}}$. For hydrogen, at $T_\mathrm{e} > 13.6$ eV, the ratio of the excitation rate to the ionization rate becomes constant. The line intensity measured by the D_α photodiodes can then be considered to be proportional to the number of ionizations per time [44]:

$$\frac{\#\text{ionizations}}{\text{time}} = n_\mathrm{D} n_\mathrm{e} \langle \sigma_\mathrm{i} v_\mathrm{e} \rangle \propto \frac{\# D^{3\rightarrow 2}}{\text{time}} \tag{2.23}$$

Here n_D is the density of neutral particles (deuterium), $\langle \sigma_\mathrm{i} v_\mathrm{e} \rangle$ is the ionization rate.

During the flattop of a plasma discharge, the signals from D_α photodiodes mainly depend on the neutral density at the SOL where the ionizations occur, which is determined mostly by recycling, and thus particle flux in the SOL. As an example, the D_α emission signal drops at the L-H transition due to reduced transport in the H-mode phase, and appears as spikes due to the expulsion of heat and particles when the Edge Localized Modes (ELMs) occur.

A set of 15 photodiodes (PD) are installed in TCV to measure the radiation emitted from the plasma in the visible range of the electromagnetic spectrum, and 6 of them have a D_α filter (656.3 nm). One of the D_α photodiodes views vertically from the top, and the others views horizontally from the LFS to $z = \pm 40$ cm and $z = 0$ (the midplane), respectively. In this work, we focus on the oscillations in D_α emission signals at the GAM frequency, which are interpreted as particle flux modulations by the GAMs. The sampling frequency of the PDs was especially set to 125 kHz rather than the usual 50 kHz, so that the GAMs (typically around $20-40$ kHz) could be detected.

2.4 Data analysis techniques

This section describes several statistical techniques that will be used in the data analysis process to extract the relevant physical information from the raw data of density fluctuations $\tilde{n}(x,t)$ measured by TPCI, where x denotes the position in the object plane, i.e., the plasma.

The basic statistical quantities such as rms values, auto- and cross-spectral density functions in the frequency domain, auto- and cross-correlation functions in the time domain are calculated over time intervals in which the plasma parameters do not change drastically, so that one can assume the turbulence characteristics are the same over the integration time. The calculation in the frequency domain is evaluated using standard Fast Fourier Transform (FFT) procedures. In the wavenumber domain, due to the limited number and uneven spacing between the detectors, an iterative row-action method for interval constraints with entropy optimization was employed to calculate the conditional spectrum $S(k|f)$ [45], which provides information on the form of the wave-number spectrum as a function of frequency, factoring out the absolute dependence on frequency. The method of calculation is discussed in section 2.4.1. The two-dimensional frequency-wavenumber spectrum $S(k,f)$ is then calculated by multiplying the conditional spectrum by the frequency spectrum. Finally the wavenumber spectrum $S(k)$ can be calculated by integrating $S(k,f)$ over the frequency domain. Higher order Fourier analysis such as the bispectrum $B(f_1,f_2)$ [46], which is an ensemble average of a product of three spectral components, is used in this thesis to study the nonlinear interactions between the GAMs and background turbulence, as described in section 2.4.2.

2.4.1 Conditional spectrum calculation

The conditional spectrum $S(k|f)$ is defined as the spatial Fourier transform of the complex coherence function:

$$\begin{aligned} &S(k|f) = \mathrm{FT}(C_{xy}(f)) \\ &C_{xy}(f) = \frac{G_{xy}(f)}{\sqrt{G_x(f)G_y(f)}} \end{aligned} \tag{2.24}$$

where $G_{xy}(f)$ and $G_x(f)$ are the cross and auto power spectral density function. In the case of spatially uniform turbulence, it has the relation:

$$S(k|f) = S(k,f)/S(f) \tag{2.25}$$

The spatial Fourier transform described in Eq. 2.24 cannot be directly evaluated by FFT due to the low number (nine) and irregular spacing of the spatial points available from the diagnostic. The alternative method is to find a conditional spectrum whose inverse Fourier transform matches the complex coherence function $C_{\mathrm{xy}}(f)$ to within the error bars. A generalized iterative row-action method for interval convex programming [47, 48] is used to minimize a function of the conditional spectrum $S(k|f)$ subject to the interval constraints, with the real and imaginary part of the complex values treated separately,

$$C - \mathrm{d}C \le A * S \le C + \mathrm{d}C \tag{2.26}$$

where C and $\mathrm{d}C$ are the complex coherence function and its error, $A * S$ is the inverse Fourier transform of $S(k|f)$.

First some relevant quantities used in this method are defined as follows: details on the mathematical derivations can be found in reference [48, 49]. The most basic one is the Bregman function $f(S)$ for minimization, and also the *D-function associated with the function* $f(x)$:

$$D(x,y) = f(x) - f(y) - \left\langle \nabla f(y), x-y \right\rangle \tag{2.27}$$

The *D-projection of the point* y *onto a set* Ω is defined by the point $x^* \in \Omega$ where the minimum of the D-function is found.
A hyperplane is defined as a set of the form

$$H = \{x | \langle a, x \rangle = b\}, \tag{2.28}$$

the D-projection λ_k of $S^{(k)}$ on the hyperplane $\left\{S \in \mathbf{R}^n | \left\langle A_{i_k}, S \right\rangle = b_{i_k}\right\}$ can be calculated as follows:

$$\lambda_k \left[b_{i_k} - \left\langle A_{i_k}, S^{(k)} \right\rangle \right] = D(S^{(k+1)}, S^{(k)}) + D(S^{(k)}, S^{(k+1)}) \tag{2.29}$$

In general, the iterative method starts with an initial guess taken as $\nabla f(S^{(0)}) = -A^{\mathrm{T}} z^{(0)}$. The typical step of one iteration is:

$$\begin{aligned} \nabla f(S^{(k+1)}) &= \nabla f(S^{(k)}) + c^{(k)} A_{i_k} \\ z^{(k+1)} &= z^{(k)} - c^{(k)} e_{i_k} \end{aligned} \tag{2.30}$$

Here $c^{(k)}$ is the median of the three real numbers $z_{i_k}^{(k)}$,$\Delta^{(k)}$ and $\Gamma^{(k)}$), where $\Delta^{(k)}$ and $\Gamma^{(k)}$ are the parameters associated with the D-projection of $S^{(k)}$ onto the hyperplanes corresponding to $b_{i_k} = C_{i_k} - dC_{i_k}$ and $b_{i_k} = C_{i_k} + dC_{i_k}$, respectively.
Two practically significant Bregman functions are mostly used in this method. The first is to minimize the norm $\|S\| = \sqrt{\sum_{j=1}^{n} S_j^2}$, the Bregman function is chosen as:

$$f(S) = \frac{1}{2} \|S\|^2 \tag{2.31}$$

In this case, the algorithm reduces to Hildreth's method for interval constraints [47]:

$$\begin{aligned} \nabla f(S) &= S \\ D(S_1, S_2) &= \frac{1}{2} \|S_1 - S_2\|^2 \\ \lambda_k &= \frac{b_{i_k} - \left\langle A_{i_k}, S^{(k)} \right\rangle}{\left\| A_{i_k} \right\|^2} \end{aligned} \tag{2.32}$$

The other method which is used in this work and also in [34] chooses the entropy function:

$$f(S) = \sum_{j=1}^{n} S_j \ln S_j \tag{2.33}$$

This method allows the iteractive solution of entropy optimization problems. The relevant functions can be derived from Eq. 2.30, 2.27 and 2.29:

$$\begin{aligned}
\nabla f(S) &= \ln S + 1 \\
D(S_1, S_2) &= \sum_{j=1}^{n} \left[S_1 \ln \frac{S_1}{S_2} - (S_1 - S_2) \right] \\
\lambda_k &= \frac{b_{i_k} - \langle A_{i_k}, S^{(k)} \rangle}{\sum_{j=1}^{n} A_{i_k}^2 S^{(k)}}
\end{aligned} \tag{2.34}$$

In practice, the real and imaginary part of equation 2.26 are treated separately, because the conditional spectrum $S(k|f)$ is real and positive. The inverse Fourier transform matrix is defined as:

$$A_{\mathrm{ij}} = \frac{dk}{2\pi} \bullet \begin{pmatrix} \cos(r_{\mathrm{i}} k_{\mathrm{j}}) \\ \sin(r_{\mathrm{i}} k_{\mathrm{j}}) \end{pmatrix} \tag{2.35}$$

The real and imaginary part of the complex coherence function $C_{\mathrm{xy}}(f)$ can be written as:

$$\begin{aligned}
\mathrm{Re}\left[C_{\mathrm{xy}}(f)\right] &= \frac{1}{2\pi} \int_{-\infty}^{\infty} S(k|f) \cos(r_{\mathrm{i}} k_{\mathrm{j}})\, \mathrm{d}k \\
\mathrm{Im}\left[C_{\mathrm{xy}}(f)\right] &= \frac{1}{2\pi} \int_{-\infty}^{\infty} S(k|f) \sin(r_{\mathrm{i}} k_{\mathrm{j}})\, \mathrm{d}k
\end{aligned} \tag{2.36}$$

The error of the real and imaginary part of $C_{\mathrm{xy}}(f)$ is calculated using error propagation with the statistical error of the squared coherence and cross phase.

2.4.2 Bi-spectral analysis

Linear spectral analysis techniques such as the power spectrum $P(f)$ (second-order spectra), which describe the frequency distribution of power of statistically uncorrelated waves, has long been successfully utilized in the study of fluctuations in plasmas. However they are of limited value when various spectral components nonlinearly interact with one another. These nonlinear interactions result in new spectral components being formed which are phase coherent, and thus can be detected by higher order spectral techniques such as the bispectrum $B(f_1, f_2)$ (third-order spectrum).
The bispectrum $B(f_1, f_2)$ is defined as the third-order cumulant spectra:

$$B(f_1, f_2) = E[X_{f_1} X_{f_2} X^*_{f_1+f_2}] \tag{2.37}$$

where $E[\bullet]$ denotes an expected value. It represents the contribution of the spectral components at f_1 and f_2 of area $(\Delta f)^2$ to the cumulant $C[x^3(t)]$, where $x(t)$ is a fluctuating quantity and $C[\bullet]$ denotes the cumulant average. Therefore integrating the bispectrum over the 2-D frequency domain f_1 and f_2 yields $E[x^3(t)]$. An analogy can be found in the power spectrum $P(f) = E[X_f X^*_f]$ as the second-order cumulant spectra, and integrating the power spectrum over the frequency domain yields the variance $E[x^2(t)]$. From Eq. 2.37 the symmetry condition of the bispectrum is:

$$\begin{aligned} B(f_1,f_2) &= B(f_2,f_1) = B^*(-f_1,-f_2) \\ B(f_1,f_2) &= B(-f_1-f_2,f_2) = B(f_1,-f_1-f_2) \end{aligned} \tag{2.38}$$

Consider three waves at f_1, f_2 and f_1+f_2, if they are spontaneously excited, their phases are statistically independent, and thus the sum phase of these three spectral components will be randomly distributed. A statistical averaging will vanish the bispectrum due to the random phase mixing effect. On the other hand, if they are nonlinearly coupled to each other, the total phase will not be random and the statistical averaging will leave a non-zero value of the bispectrum.

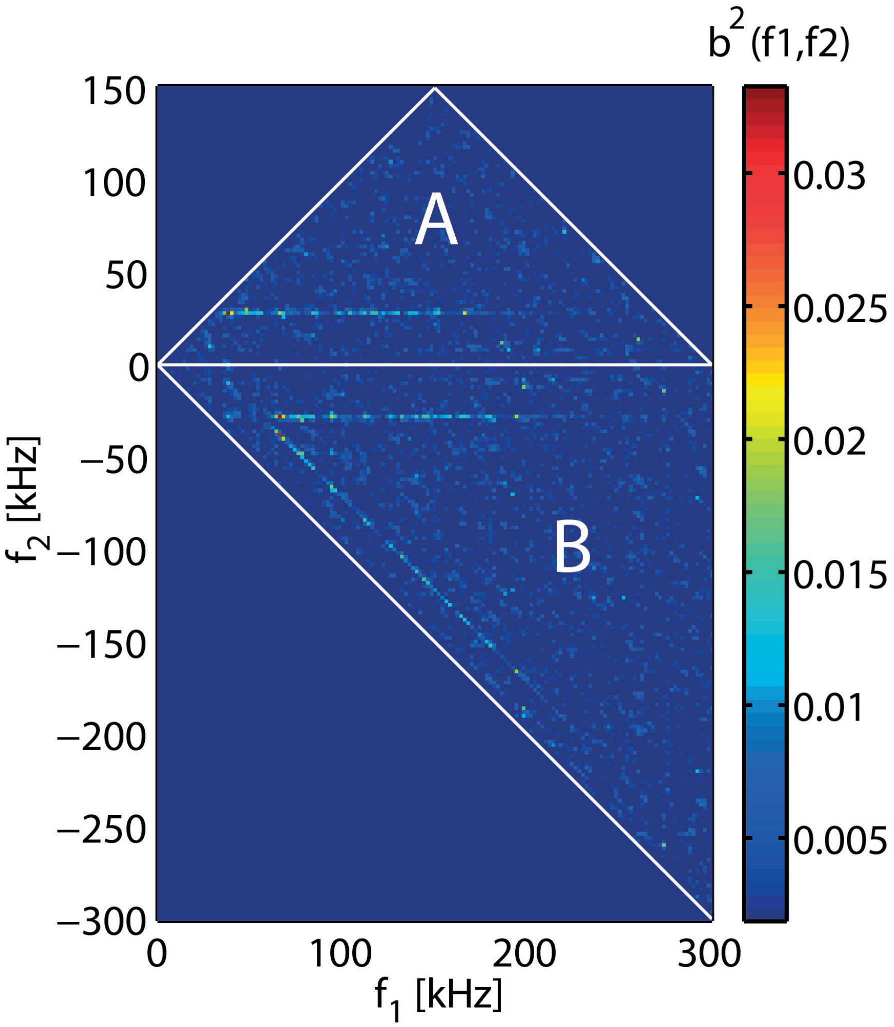

Figure 2.13: Schematic of squared bicoherence $b^2(f_1,f_2)$ of density fluctuations measured by TPCI in a TCV discharge.

The most commonly used quantity to measure the three-wave coupling is the squared bicoherence $b^2(f_1, f_2)$, defined as:

$$b^2(f_1, f_2) = \frac{|B(f_1, f_2)|^2}{E[|X_{f_1} X_{f_2}|^2] E[|X_{f_1+f_2}|^2]} \tag{2.39}$$

It measures the coherence between three waves due to the wave coupling, i.e., the fraction of power at $f_1 + f_2$ due to the three-wave coupling.

For a random process $\tilde{x}(t)$, the bispectrum and squared bicoherence are calculated as follows:

$$\begin{aligned} \hat{B}(f_1, f_2) &= \frac{1}{M} \sum_{i=1}^{M} X_{f_1}^{(i)} X_{f_2}^{(i)} X_{f_1+f_2}^{*(i)} \\ \hat{b}^2 &= |\hat{B}(f_1, f_2)|^2 [(\frac{1}{M} \sum_{i=1}^{M} |X_{f_1}^{(i)} X_{f_2}^{(i)}|^2)(\frac{1}{M} \sum_{i=1}^{M} |X_{f_1+f_2}^{(i)}|^2)]^{-1} \end{aligned} \tag{2.40}$$

where $X_f^{(i)}$ denotes the fth component of the Fourier series of realization i in the ensemble and M is the number of realizations.

An example of the squared bicoherence spectrum applied to data from TPCI can be seen in Fig. 2.13. Here region A is for the sum interactions and region B is for the difference interactions, although they are interchangeable by changing variables such that $f_1 \rightarrow -f_2$, $f_2 \rightarrow f_1 + f_2$ and using the symmetry relation in Eq. 2.38. It can be seen that the squared bicoherence has large value at $f_1 \approx \pm 30$ kHz (the two horizontal lines) and $f_1 + f_2 \approx 30$ kHz (the 45° tilted line). The frequency range in f_2 of the line in region A is about 30 – 200 kHz. This illustrates the nonlinear coupling between a coherent mode at 30 kHz and broadband turbulence from 30 to 200 kHz.

3 Dependence of plasma turbulence on shape

3.1 Motivation

In tokamaks, the shape of the plasma poloidal cross-section has been observed to have a strong influence on a number of plasma properties. Previous research has revealed in particular the effect of plasma vertical elongation κ on the stability limits in plasma current I_p and normalized β. Here β is defined as the ratio of plasma pressure p to the magnetic field pressure:

$$\beta = p/(B^2/2\mu_0) \tag{3.1}$$

Higher elongation κ brings a higher global energy confinement time and permits the attainment of higher β compared to a circular plasma, until hitting the absolute axisymmetric stability limit $\kappa \leq 2.58$. As a consequence, the D-shaped plasma with an elongation of about 1.6 has become the design standard for many tokamaks including ITER. The effect of triangularity δ on plasma properties, on the other hand, has been addressed less. The unique shaping capabilities of the TCV tokamak provided opportunities for investigations of the triangularity effects.

Previous studies [10, 11] on TCV have documented the effect of triangularity on energy confinement and electron heat transport. The energy confinement time significantly benefits from negative edge triangularity compared to standard positive triangularity. For a L-mode plasma with $\delta < 0$, only half the central electron cyclotron heating power was required to obtain the same electron temperature and density profiles as in the $\delta > 0$ case, as shown in Fig. 3.1. Here we use the normalized radius as:

$$\rho_{\mathrm{vol}} = \sqrt{V/V_{\mathrm{LCFS}}} \tag{3.2}$$

where V and V_{LCFS} are plasma volumes enclosed by the flux surfaces at ρ and at the last closed flux surface.

One of the most interesting but not yet fully understood observations is that the electron heat transport level $\chi_e = Q_e/n\nabla T_e$ is reduced at all radial locations in the outer half of the

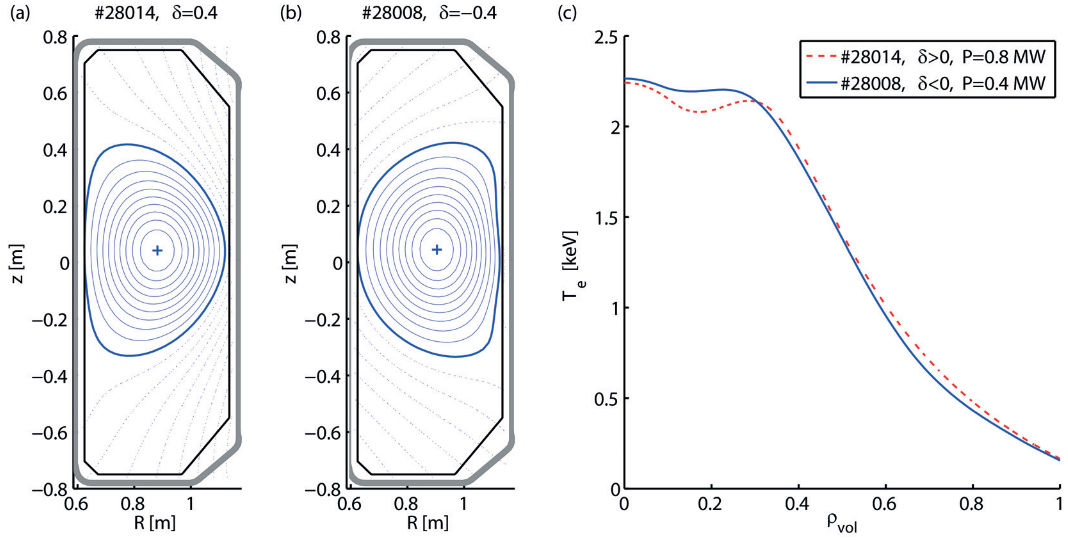

Figure 3.1: (a,b) Equilibrium reconstructions for TCV discharges #28014 and #28008 with, respectively, positive ($\delta = 0.4$) and negative ($\delta = -0.4$) triangularities. (c) Electron temperature profile as a function of ρ_{vol} for these two discharges. The profiles are similar with different EC heating power. [6]

plasma, while the triangularity has a finite radial penetration depth. A more complete study [7] must also include the effective collisionality ν_{eff}, which normalizes the electron-ion collision frequency ν_{ei} to the curvature drift frequency ω_{De}. An approximate expression of effective collisionality can be written as:

$$\nu_{\text{eff}} = 0.1 R n_{\text{e}} Z_{\text{eff}} / T_{\text{e}}^2 \tag{3.3}$$

Here R is the major radius, n_{e} and T_{e} are the electron density and temperature, Z_{eff} is the effective ion charge. Experimental results demonstrate that the electron heat diffusivity χ_{e} decreases significantly with increasing ν_{eff} and decreasing δ. The dependence on triangularity is strong in low collisionality EC heated L-mode plasmas while weak in high collisionality Ohmic L-mode plasmas, as shown in Fig. 3.2. The reason is believed to be the stabilizing role of finite collisionality on TEM-type instabilities, shown by gyrokinetic simulations [50].

A recent study of plasma density and temperature profile stiffness [6] suggests that the triangularity dependent non-stiffness of the plasma edge may be enough to potentially explain the global increase of the electron temperature in the core. Here the stiffness is defined as follows: if the profile is stiff, there exists a critical gradient, and increasing the heating power once this gradient is reached would only result in increased turbulence and transport level with no further increase in the temperature inverse scale length $R/L_{T_{\text{e}}}$. The normalized gradient for a quantity X is defined as:

$$R/L_X = -R\nabla X/X \tag{3.4}$$

While the *stiff* core part of the plasma outside the inversion radius keeps a constant R/L_{T_e} independent of the triangularity, the edge plasma (typically $\rho > 0.8$) can be described with a uniform gradient ∇T_e, which is dependent on plasma parameters such as I_p and δ. Therefore although the confinement improvement is localized near the edge, the higher edge temperature gradient ∇T_e acts to increase T_e everywhere. These conclusions are at odds with earlier measurements [7] which explicitly revealed a dependence of the core heat diffusivity on the edge triangularity. The discrepancy is currently unresolved, though it is believed that a careful analysis of the measurement uncertainties is required to resolve it.

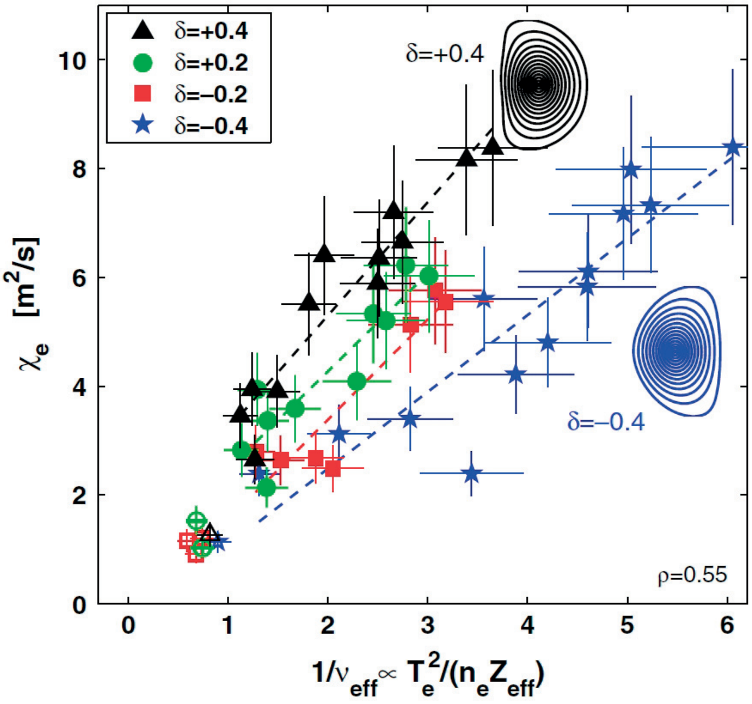

Figure 3.2: Dependence of the experimental electron heat diffusivity χ_e on edge triangularity δ and effective collisionality ν_{eff} in EC heated L-mode plasmas (full symbols) and high collisionality Ohmic plasmas (open symbols). The dashed lines indicate the offset-linear fits. [7]

The hypothesis of a δ effect on the non-stiff edge is partly supported by local flux-tube [51, 52] gyrokinetic simulation results, indicating that the beneficial effect of negative triangularity is only significant at the plasma edge where the local triangularity is large, while it is negligible in the core. The flux-tube GENE simulations also suggested that the strongest effect exerted by negative triangularity is an increase of the critical gradient [52]. Another possible candidate to explain the discrepancies between experimental measurements and flux-tube simulation results is finite ρ_* effects, and global simulations are required to correctly account for such effects. Recent results from gradient-driven global simulations [53] show a very strong global effect, i.e., a reduction in electron heat flux profiles at all radii with negative δ compared to positive δ case.

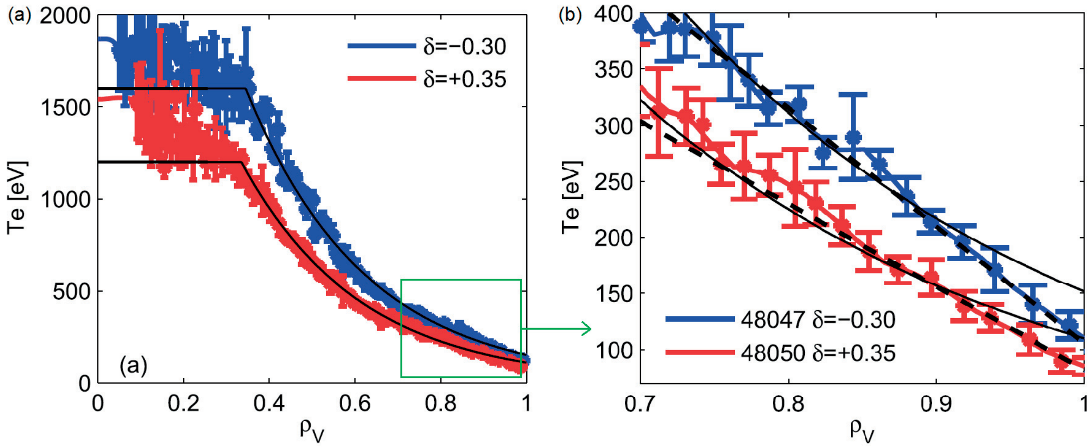

Figure 3.3: (a) T_e profiles versus ρ_{vol} obtained with positive (red) and negative (blue) triangularities with same 0.4 MW EC heating power. (b) Zoom of edge part profiles in Fig. 3.3(a) including the exponential (solid lines) and linear (dashed) fitting. [6]

3.2 Experimental setup

TCV plasma discharges were performed with typical toroidal magnetic field $B_T \approx 1.3$ T, plasma current $I_p = 250$ kA, edge elongation $\kappa \approx 1.4$. The effect of triangularity is studied mainly in limited L-mode plasmas with constant ECH input power. ECH power scans and Ohmic density scans were also performed to investigate the effect of collisionality. The typical central density is around $2-3\times10^{19}$ m^{-3}, except in the Ohmic density ramp, where the central density varies from 1.5 to 6.5×10^{19} m^{-3}. The auxiliary heating is applied in the form of electron cyclotron resonance heating (ECRH) at the second (X2) harmonic, the input power used in this work varying from 0.2 to 1.35 MW. With this strong electron heating, a large difference in electron and ion temperatures ($T_e/T_i > 3$) can be observed in the core of a typical L-mode plasma in TCV, and the type of turbulence responsible for the electron transport is believed to be mainly the trapped-electron mode (TEM). The dominating turbulence type only changes from TEM to ion-temperature gradient mode (ITG) in a high density Ohmic plasma.

The main diagnostic used to study the GAM regime transition is the tangential phase contrast imaging (TPCI) diagnostic [2]. With the spatial filtering technique, the measurements are localized at the point where the laser is tangent to the magnetic flux surfaces, and the selected turbulence wave vector is mainly in the radial direction k_ρ. The relative amplitude of density fluctuations $\tilde{n}/n$ is calculated as the root mean square (rms) value of the TPCI signal normalized by the effective integration length and by the local electron density measured by the Thomson scattering diagnostic. Because the TPCI diagnostic was in a preliminary configuration without absolute calibration, the absolute value of $\tilde{n}/n$ is not addressed. Nevertheless, an acoustic wave calibration was performed at the beginning of each plasma discharge to allow a relative comparison between different channels.

In this work, the experimental data was down sampled to 800 kHz sampling rate with a digital anti-aliasing filter. This allowed us to avoid the 400 kHz pick-up noise that is observed during the ECH phase; also experimental observations had shown that the turbulence spectral amplitude above 300 kHz is negligible compared to low frequency components. A high-pass filter normally at 10 kHz was always applied to exclude the effect of vibrations; in many cases when there were coherent modes such as MHD modes and GAMs present, the high-pass frequency limit was increased to exclude these large amplitude modes when calculating the broadband turbulence amplitude.

The 5 cm diameter laser beam is subdivided by the detection geometry into 9 parallel and co-planar unevenly spaced chords. The range of wavenumber is $k_c < k < 9.4$ rad/cm, with the lower cutoff k_c defined by the width of the phase plate groove and equal to $k_c = 1.01$ rad/cm in most experiments in this work except where otherwise noted. The wavenumber resolution is essentially limited by the beam diameter $\delta k \approx 1.25$ rad/cm, while the plots of k-spectra appear smoother due to the row-action method used in the calculation.

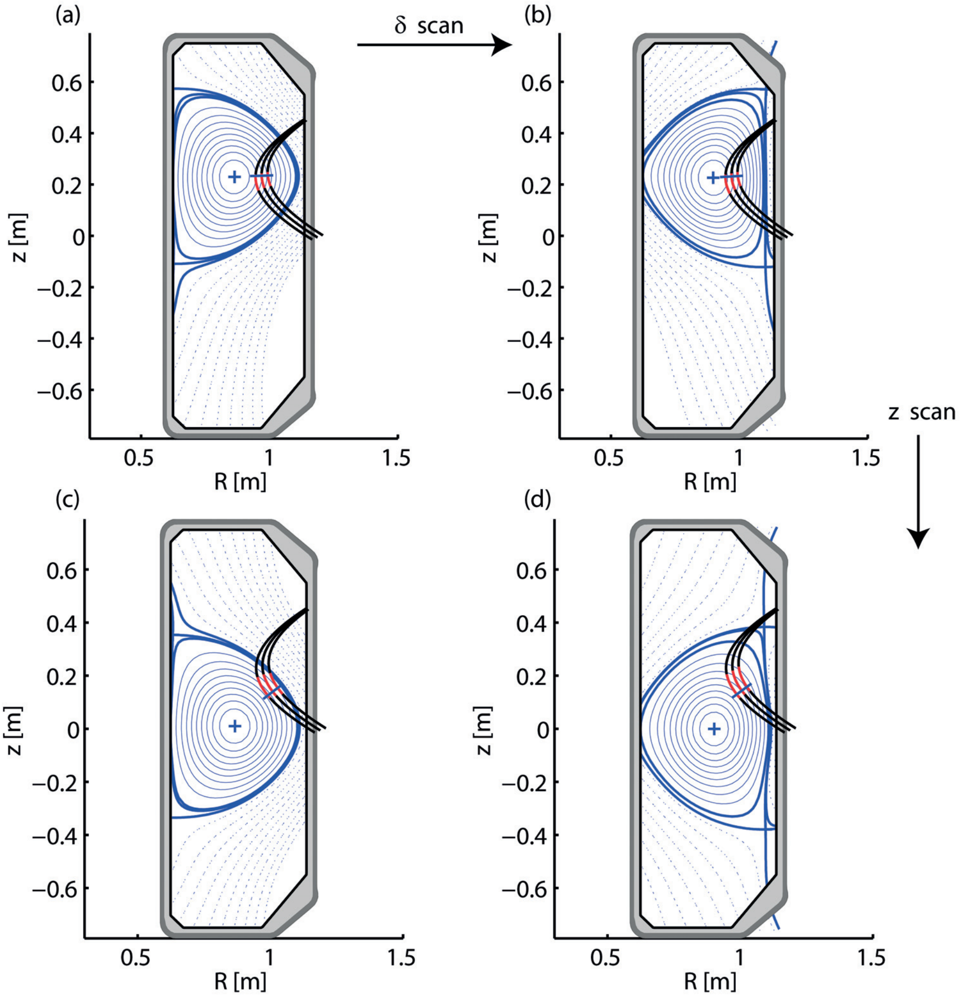

Figure 3.4: Plasma equilibrium of (a) $\delta > 0$, $z = 0.23$ m, (b) $\delta < 0$, $z = 0.23$ m, (c) $\delta > 0$, $z = 0$ m, (d) $\delta < 0$, $z = 0$ m discharges on TCV. The black curves denote the poloidal projection of the TPCI laser beam, with the beam path selected by the spatial filter highlighted in red. The blue straight line denotes the tangent wave-vector.

A large radial range from core to edge plasma can be resolved by shifting the plasma column vertically in the highly-elongated TCV vacuum vessel. Ideally the angle of the spatial filter needs to be optimized at each vertical position to achieve the highest radial resolution; however, for practical reasons in this work it is placed at a median angle so that the tangent point is always covered by the 60° wedge angle in the entire range of vertical shift. Two types of scans (see Fig. 3.4) were performed for the turbulence measurement in this work to exploit the radial accessibility of TPCI: one is to vary the vertical position at constant triangularity for each shot, the other is to vary the triangularity at constant vertical position. In the latter case, the radial range of measurement in terms of ρ is different with different δ during the scan because of different geometries: when the magnetic axis of the plasma is at $z = 0.23$ m where the laser is closest to the magnetic axis, i.e., optimized for core measurement, the radial range is about $0.34 < \rho_{\text{vol}} < 0.51$ at $\delta = 0.5$ and $0.24 < \rho_{\text{vol}} < 0.41$ at $\delta = -0.5$, and the radial resolution is $\Delta\rho \approx 0.04-0.08$; when the magnetic axis is at the vessel midplane for edge measurements, the radial range is about $0.73 < \rho_{\text{vol}} < 0.93$ at $\delta = 0.5$ and $0.63 < \rho_{\text{vol}} < 0.77$ at $\delta = -0.5$, and the radial resolution is $\Delta\rho \approx 0.1$ for each chord; the optimized radial resolution $\Delta\rho \approx 0.02$ can be achieved at $z = 0.15$ m. Therefore the plasmas need to be at different vertical positions for different triangularities for a direct comparison at fixed radial position. Multiple triangularity and vertical scans were performed to have a complete coverage of δ and ρ_{vol}.

In order to investigate the complex nature of plasma turbulence, transport and profiles, two different approaches are taken in this work: one is to heat the plasma with the same ECH power with different δ: the resulting T_{e} profiles are different; the other is to heat the plasma to achieve the same T_{e} profiles with different ECH power at different δ.

The majority of discharges were performed with the first approach due to the simplicity of operation. This also allows a direct verification of the edge non-stiffness hypothesis (see Fig. 3.3). In this approach, in comparison to a $\delta > 0$ plasma, the $\delta < 0$ plasma has reduced turbulence and transport level and better confinement, resulting in a higher T_{e}, ∇T_{e} and lower effective collisionality ν_{eff}, which would in turn tend to increase the turbulence and transport level. Therefore Ohmic density scans and ECH power scans were also performed in addition to investigate the collisionality effect independently. Experimental data were combined in a $< \delta, \rho_{\text{vol}}, \nu_{\text{eff}} >$ multi-parameter database for the analysis. In the second approach, plasma discharges were performed with gas input and ECH power optimized to achieve similar density and electron temperature profiles. The aim was to exclude the effect of gradients and collisionality and also provide direct comparison with results from gradient-driven global nonlinear gyrokinetic simulations.

3.3 Density fluctuations comparison between positive and negative triangularity

In this section, we compare the density fluctuations measured by TPCI in two similar discharges, except for the difference in shape: one with $\delta > 0$ and the other with $\delta < 0$. As mentioned in Sec. 3.2, two different approaches were taken: one with the same heating power, the other with the same density and temperature profiles. The experiments were carried out in two different TCV campaigns: the "equal heating" approach was in 2013 and the "equal profiles" one was in 2016. The results from the "equal heating" approach are presented in Sec. 3.3.1, and results from the "equal profiles" approach are addressed in Sec. 3.3.2. Our aim is to present a general description of the phenomenology, including all relevant spectral quantities and spatial dependence, in all conditions studied.

3.3.1 Results with same heating

As a first step, we took the "equal heating" approach: both discharges have equal 0.45 MW ECH central heating. The difference in density fluctuations is studied by comparing the spectra from TPCI between two similar discharges with $\delta > 0$ and $\delta < 0$, respectively. Vertical scans were performed from $z = -0.1$ m to 0.15 m to cover the radial range from the core plasma $\rho_{\mathrm{vol}} \approx 0.5$ to the edge, while the ECH launchers were moved accordingly to follow the magnetic axis of the plasma.

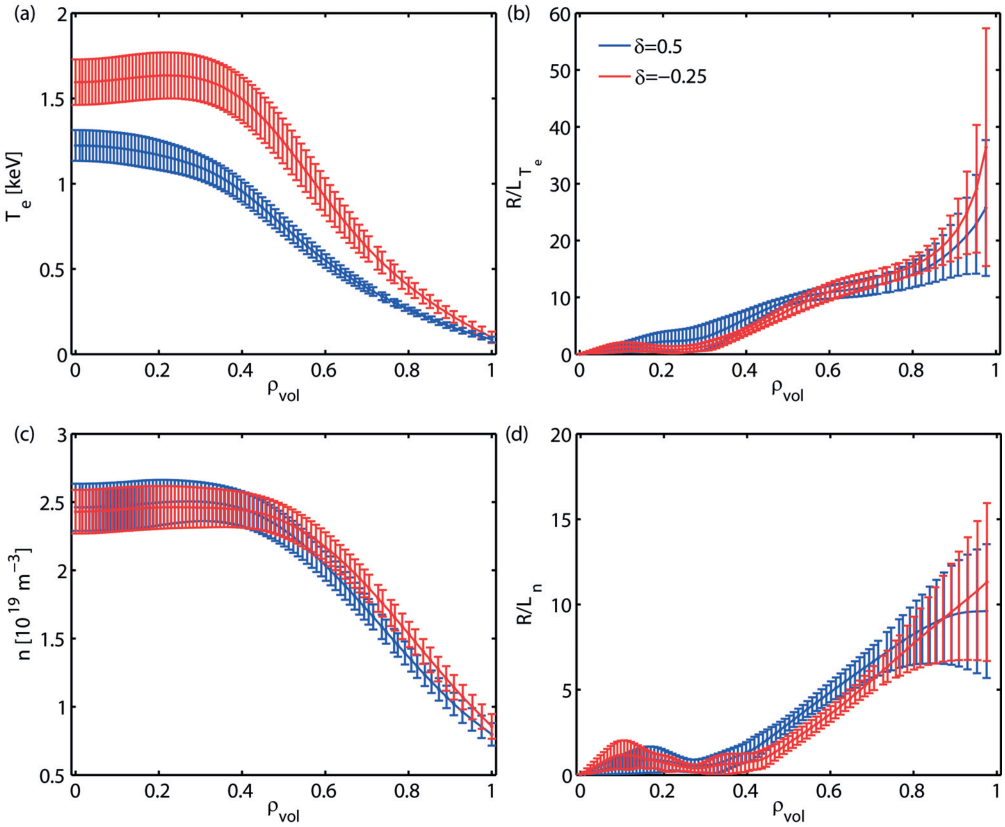

Figure 3.5: Radial profiles of (a) electron temperature, (b) normalized electron temperature gradient, (c) electron density ,(d) normalized density gradient, taking the average value in the time range $t = 0.6 - 1.8$ s in TCV discharge #49052 (blue) and #49051 (red).

Figure 3.5 shows the T_{e}, n_{e}, $R/L_{\mathrm{T_e}}$, R/L_{n} radial profiles averaged in the time interval $0.6 - 1.8$ s, during which the plasma parameters stay nearly constant. The central electron temperature in the negative triangularity discharge is about 30% higher than with positive triangularity, as expected. The density profiles of these two discharges are nearly identical, as shown in Fig. 3.5 (c), although the $\delta < 0$ discharge has slightly higher density outside $\rho = 0.5$. Figure 3.5 (b) shows that R/L_{T_e} in both discharges has a flatter region in the core around $10 < R/L_{T_e} < 15$ (stiff core) and a steeper edge (non-stiff edge), which is consistent with the hypothesis in reference [6]. The radial range of the stiff region is $\rho_{\mathrm{vol}} = 0.5 - 0.8$ for $\delta > 0$ and around $0.6 - 0.8$ for $\delta < 0$. Regarding R/L_{n}, the $\delta > 0$ discharge #49052 has a flatter region around $R/L_{\mathrm{n}} = 8$ at the edge, while in #49051 ($\delta < 0$) the normalized gradient increases monotonically over the entire radial range. Note that both R/L_{T_e} and R/L_{n} fluctuate considerably over time at the plasma edge, and what is shown in Figs. 3.5 (b) and (d) is only the average value over the time. The errorbars of the normalized gradients denote their standard deviation.

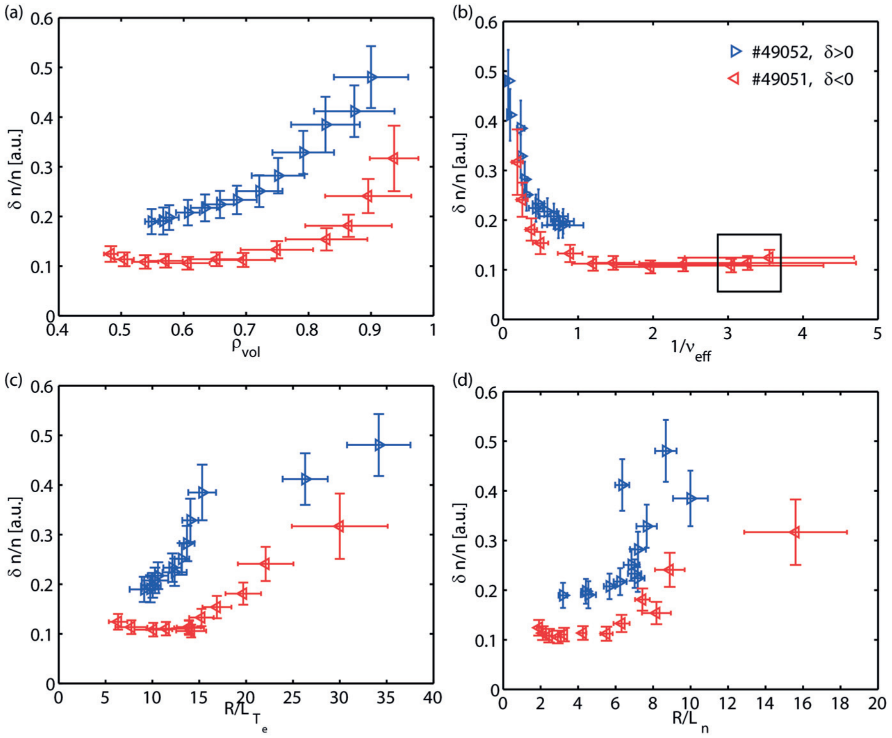

Figure 3.6: Relative density fluctuation amplitude $\tilde{n}/n$ as a function of radial position ρ_{vol} (a), reciprocal of effective collisionality $1/\nu_{\mathrm{eff}}$ (b), normalized gradients R/L_{T_e} (c) and R/L_{n} (d) in a $\delta = 0.5$ (blue) and a $\delta = -0.25$ (red) TCV discharge; both discharges have 0.45 MW EC heating the plasma center. Each data is calculated over 100 ms with frequency resolution 0.1 kHz, normalized by the selected integration length and local density n [10^{19} m^{-3}] measured by the Thomson scattering system.

In Fig. 3.6 (a) we plot the relative density fluctuation amplitude $\tilde{n}/n$ as a function of radial position ρ_{vol} measured on the TPCI central chord in these two discharges, normalized by the selected integration length and local density n. The data were taken again in the time interval $0.6 - 1.8$ s, when the plasma parameters stay nearly constant. The angle of the spatial filter was set to be optimal for core measurements, thus the uncertainty in radial localization increases when moving towards the edge. In #49052, the relative density fluctuation amplitude $\tilde{n}/n$ increases when moving outwards, the slope being steeper at the edge ($\rho_{\text{vol}} > 0.7$) than in the core region; in #49051, $\tilde{n}/n$ decreases slightly when moving outwards inside $\rho_{\text{vol}} = 0.55$, then keeps nearly constant for $0.55 < \rho_{\text{vol}} < 0.7$, and finally increases at the edge. At all radial positions, $\tilde{n}/n$ is about 2 times higher in the $\delta > 0$ discharge compared to the $\delta < 0$ case. This result is consistent with previous observations that electron heat transport χ_{e} is about 2 times lower at $\delta < 0$ [7].

Previous studies [7] have also pointed out the effect of gradients and collisionality, which are the main parameters that strongly influence the heat transport other than triangularity. The gradients serve the role of free energy source for the turbulence, and the effective collisionality plays a major role in the stability of TEM turbulence, which is dominant in TCV ECH L-mode plasmas. The dependence of the turbulence amplitude on the normalized gradients $R/L_{T_{\text{e}}}$ and R/L_{n} is shown in Figs. 3.6 (c) and (d). Here the data from the core to the edge at different radial positions $0.45 < \rho_{\text{vol}} < 0.95$ were considered as a whole. In #49052, as shown in Fig. 3.6 (c), $\tilde{n}/n$ increases with $R/L_{T_{\text{e}}}$ in the range of $10-14$, where most data points are located except the outermost two. This suggests a critical gradient around 10, which is consistent with the observation that the core T_{e} profile is stiff for $0.5 < \rho < 0.8$ as shown in Fig. 3.5 (b). It is also very sensitive to R/L_{n} at $R/L_{\text{n}} \approx 7-8$, indicating a possible critical gradient in R/L_{n}; figure 3.5 (d) indeed shows a flat region at the edge, albeit with large errorbars. In #49051, $\tilde{n}/n$ is independent of $R/L_{T_{\text{e}}}$ for $R/L_{T_{\text{e}}} < 14$ and $R/L_{\text{n}} < 6$ (at $\rho_{\text{vol}} < 0.7$), whereas above these thresholds it increases with both gradients, but with a flatter slope than in #49052, indicating less stiffness; the number of data points at the $R/L_{T_{\text{e}}} = 14$ is only $3-4$, much less than in #49052, consistent with the narrower stiff region. To summarize, the effect of negative triangularity on turbulence amplitude appears in three different aspects:

- The critical gradient has a higher value (14) for $\delta < 0$ than $\delta > 0$ (< 10).
- Above the critical gradient, the increase in turbulence has a weaker dependence on $R/L_{T_{\text{e}}}$ for $\delta < 0$.
- The radial range where the critical gradient is seen (stiff region) is narrower ($\rho_{\text{vol}} = 0.6-0.8$) for $\delta < 0$ compared to $\rho_{\text{vol}} \approx 0.5-0.8$ for $\delta > 0$.

The second and third observations both show that the stiffness in the core region is less pronounced for $\delta < 0$, so that the normalized gradient can reach a higher value, as indicated by the first observation. Note that although from Fig. 3.5 (b) it can be seen that the stiff region starts from $\rho_{\text{vol}} = 0.5$ at $R/L_{T_{\text{e}}} = 10$, the innermost measurement is limited to $\rho_{\text{vol}} = 0.53$, thus it is not clear whether $\tilde{n}/n$ is independent of $R/L_{T_{\text{e}}}$ below the critical gradient as in #49051.

On the other hand, the role of ν_{eff} as shown in Fig. 3.6 (b) needs to be treated with caution, as the dependence of $\tilde{n}/n$ on ν_{eff} might change at different radial positions. It also must be noted that a volume averaged Z_{eff} is used in this work, whereas experimentally Z_{eff} is known to vary in the radial direction; unfortunately, reliable Z_{eff} profile measurements were not available for this study. Nevertheless, the decrease of $\tilde{n}/n$ when moving outwards inside $\rho_{\text{vol}} = 0.55$ can likely be explained by a decrease of $1/\nu_{\text{eff}}$ (the 3 data points inside the black box in Fig. 3.6 (d)): the details will be addressed later in Sec. 3.4.2.

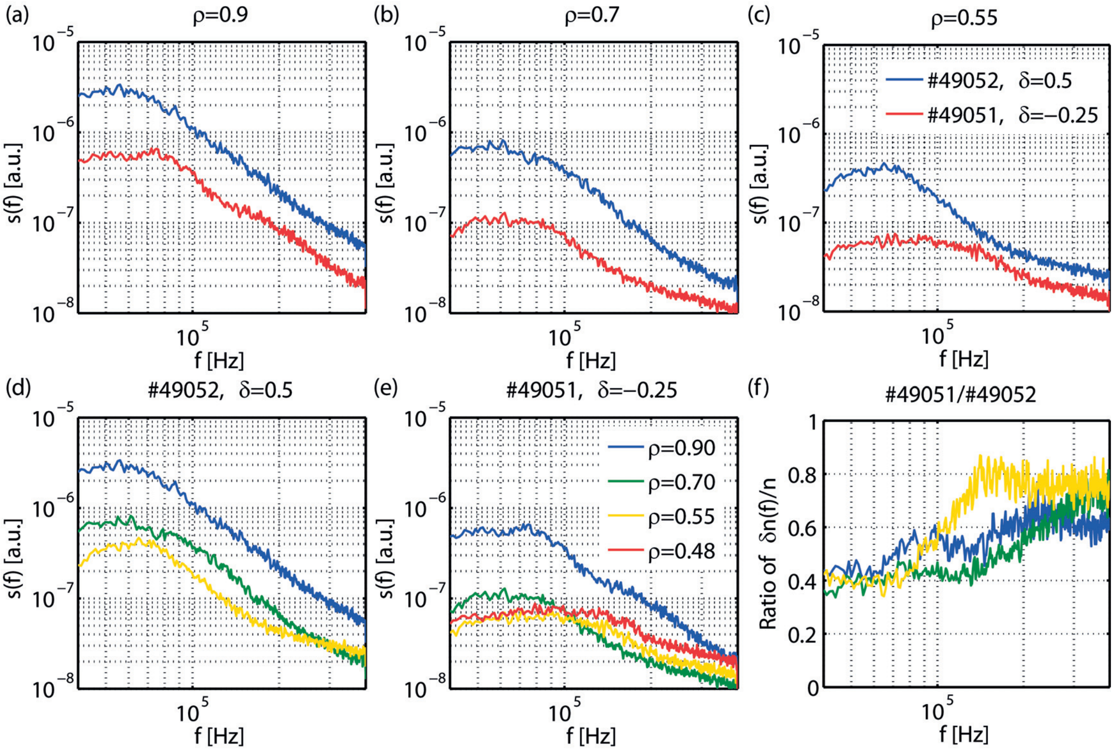

Figure 3.7: Power spectra of normalized density fluctuations $\tilde{n}/n$ at different radial positions: $\rho_{\text{vol}} = 0.9$ (a), 0.7 (b), 0.55 (c) for TCV discharges #49052 and #49051. Same spectra overlayed for all values of ρ_{vol} for #49052 (d) and #49051 (e), the latter with an extra radial point added. The spectra are averaged over 100 ms with frequency resolution 1 kHz, normalized by the square of the selected integration length and local density n [10^{19} m^{-3}]. (f) Ratio of $\tilde{n}/n$ spectral amplitude as a function of frequency between the two discharges.

In Fig. 3.7 we plot the power spectra of normalized density fluctuations $\tilde{n}/n$ for the two discharges from $f = 40$ to 400 kHz. Three radial locations were chosen around $\rho_{\text{vol}} = 0.9$ (a), 0.7 (b) and 0.55 (c) for both discharges; additionally, $\rho_{\text{vol}} = 0.48$ was added for #49051. Figure 3.7 (d) shows that in #49052, from $\rho_{\text{vol}} = 0.9$ to 0.7, the spectrum decreases monotonically with frequency reduced in the entire frequency range, with an inverse-power-law exponent for $f > 70$ kHz equal to about -2.2; from $\rho_{\text{vol}} = 0.7$ to 0.55, the behavior changes, and two distinct inverse-power-law exponents can be observed: $f^{-2.4}$ in the range $80 < f < 150$ kHz and $f^{-0.8}$ for $f > 150$ kHz. In #49051, as shown in Fig. 3.7 (e), a similar frequency spectral dependence can be observed from $\rho_{\text{vol}} = 0.9$ to 0.7, however in the high frequency range $f > 200$ kHz the reduction is less so that the inverse-power-law exponent is about -0.8; from $\rho_{\text{vol}} = 0.7$ to 0.55, the frequency spectrum broadens and flattens considerably, such that the integrated power becomes nearly constant with ρ_{vol}, as seen in Fig. 3.6; finally from $\rho_{\text{vol}} = 0.55$ to 0.48, the high frequency components are larger still while the low frequency components are roughly unchanged, so that $\tilde{n}/n$ is actually larger than in the outer neighboring region. The inverse-power-law exponent in the high frequency range $f > 200$ kHz for discharge #49051 is always around -0.8 in the radial range $\rho_{\mathrm{vol}} < 0.7$. In general, the turbulence spectrum in negative triangularity has a lower (in absolute value) inverse-power-law exponent than the positive case, indicating a reduction in the decorrelation time. The reduction of turbulence amplitude occurs mainly in the low frequency range, as shown in Fig. 3.7 (f): the relative density fluctuation amplitude of #49051 is only 40% of the case of #49052 in the low frequency range at all radial locations, although the reduction is less pronounced in the high frequency range.

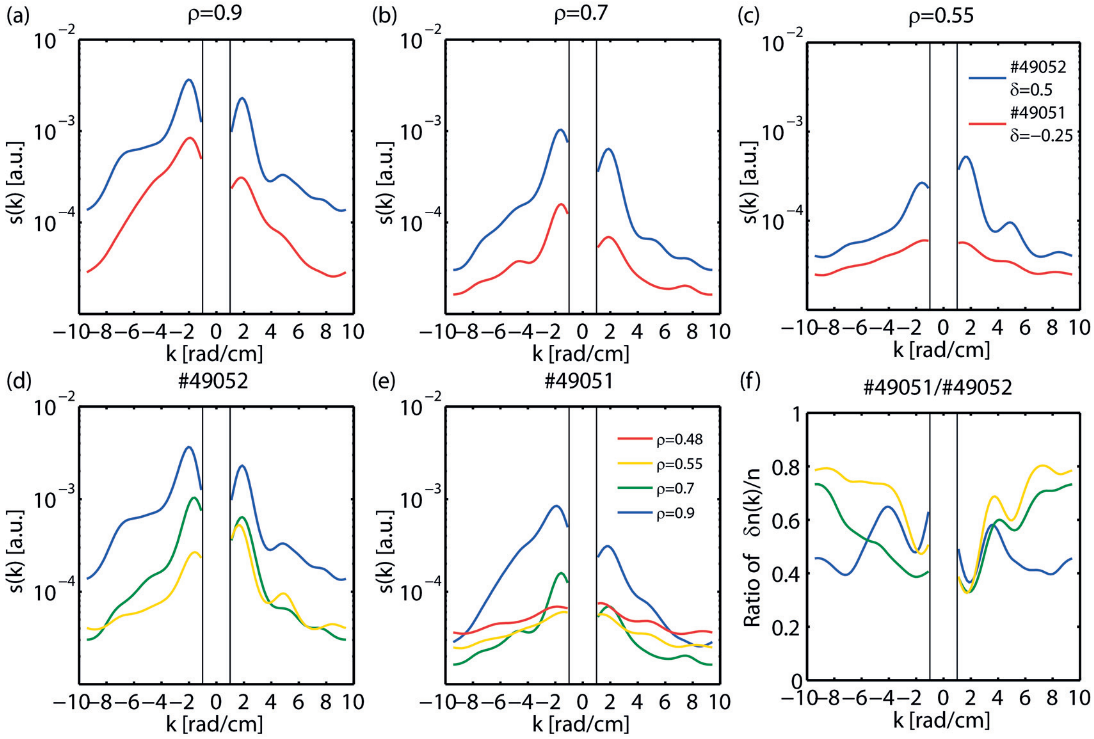

Figure 3.8: Wavenumber spectra of normalized density fluctuations $\tilde{n}/n$ at different radial positions, the order of subplots and data integration time being the same as in Fig. 3.7. The blank region around $-1 < k < 1$ rad/cm indicates the instrumental cutoff; the Nyquist wavenumber is at $k_{\mathrm{N}} = 9.4$ rad/cm.

The wave number spectra of the two discharges are plotted in Fig. 3.8 with the same plot organization as in Fig. 3.7. The spectrum $s(k)$ is normally double peaked with the two peaks at approximately symmetric positive and negative values. Figures 3.7 (a-c) show that in general, the wavenumber spectrum for $\delta < 0$ is wider than for $\delta < 0$. Note that in these experiments the TPCI measurements were mainly in the radial direction, this shows that the radial correlation length of the turbulence density fluctuations is reduced in $\delta < 0$ plasmas. Figure 3.7 (d) shows that in #49052 the $k < 0$ component keeps decreasing when moving inward, while the $k > 0$ component does not change much from $\rho_{\mathrm{vol}} = 0.7$ to 0.55: therefore, the dominant propagating direction changes from inward ($k < 0$) to outward ($k > 0$) in this range. An irregular structure at high k can be seen at $\rho_{\mathrm{vol}} = 0.9$ and disappears at $\rho_{\mathrm{vol}} = 0.7$. For #49051, a similar spectral reduction overall and especially for the irregular high k structure can also be observed from $\rho_{\text{vol}} = 0.7$ to 0.9. From $\rho_{\text{vol}} = 0.55$ to 0.7, the high k components for both the positive and negative k domains increase; this broader spectrum indicates that although the overall $\tilde{n}/n$ amplitude doesn't change, the turbulence correlation length is shorter in the core plasma of the $\delta < 0$ discharge. From $\rho_{\text{vol}} = 0.48$ to 0.55, the spectral power increases everywhere while keeping the same shape.

Figure 3.9 shows the two dimensional frequency-wavenumber spectrum $s(k, f)$ of the density fluctuations, using all 9 chords of the 5 cm diameter laser beam. The information it contains has already been addressed for the most part in the discussions over Fig. 3.7 and Fig. 3.8. Note that the amplitude in this figure is plotted in logarithmic scale. Another useful spectral quantity is the conditional spectrum $s(k|f)$ (see Eq. 2.25), shown in Fig. 3.10. The fact that it factors out the absolute dependence on frequency highlights several interesting points:

- The $k < 0$ component, moving from core to edge, in #49052 gradually increases, and its width also gradually expands in both frequency and wavenumber space. In #49051, from $\rho = 0.55$ to 0.7 the spectral power first increases at low f and low k, then from $\rho = 0.7$ to 0.9 it expands to higher f and k without a change in its peak amplitude.
- The $k > 0$ component, moving from core to edge, in #49052 actually decreases. Note that the frequency range $f < 40$ kHz is not addressed here, where the GAM ($k > 0$) amplitude increases. In #49051 the $k > 0$ component is always very weak, with the spectral peak shifting down from > 100 kHz in the core to 50 kHz at the edge.

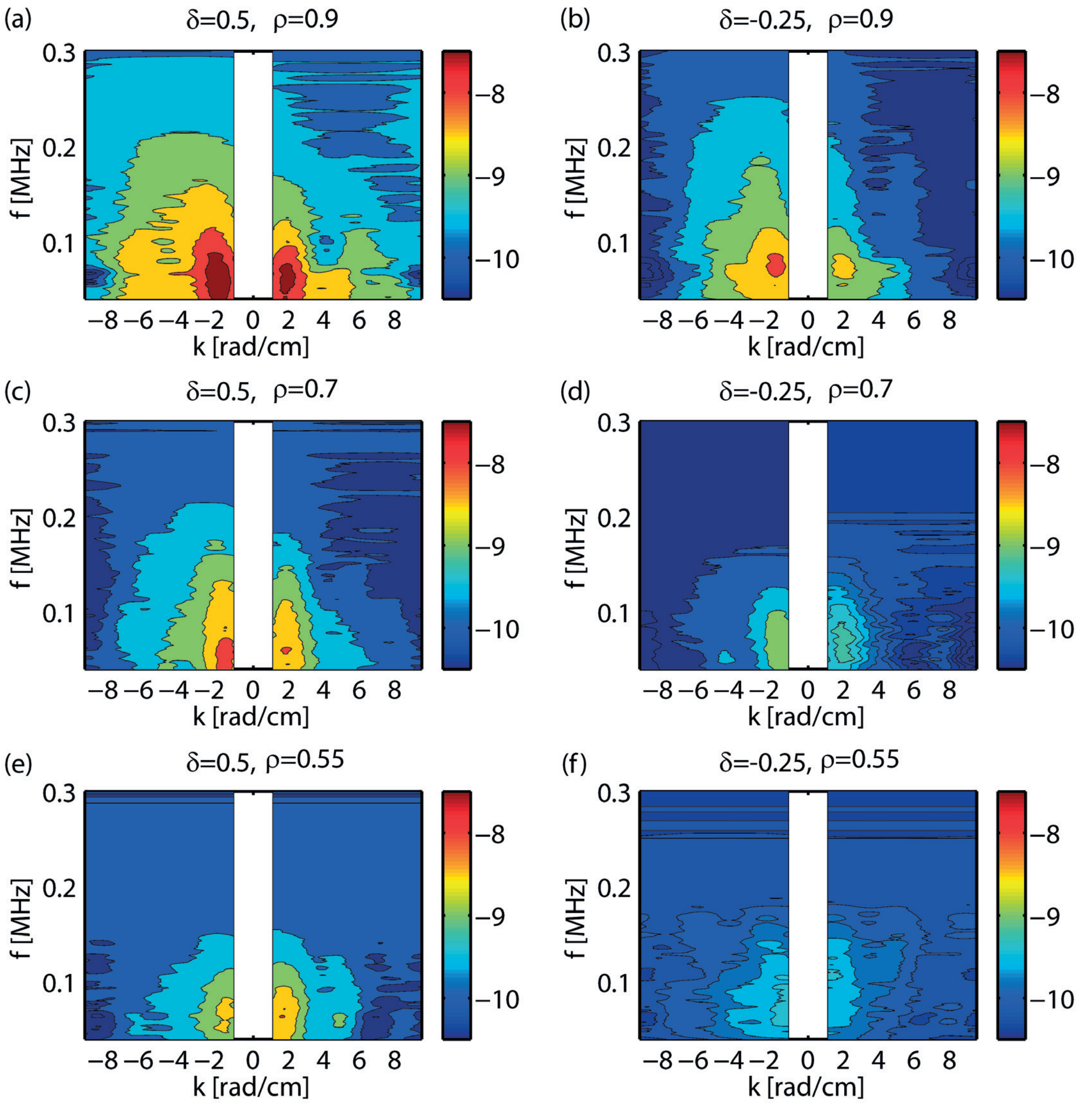

Figure 3.9: Two-dimensional frequency-wavenumber spectra $s(k, f)$ of normalized density fluctuations $\tilde{n}/n$ for TCV discharge #49052 (left) and #49051 (right) at $\rho = 0.9$ (top), 0.7 (middle) and 0.55 (bottom). The integration time and frequency resolution are as in Fig. 3.7. The contours are drawn in logarithmic scale with 10 kHz smoothing, and data with spectral power below 10^{-10} were neglected.

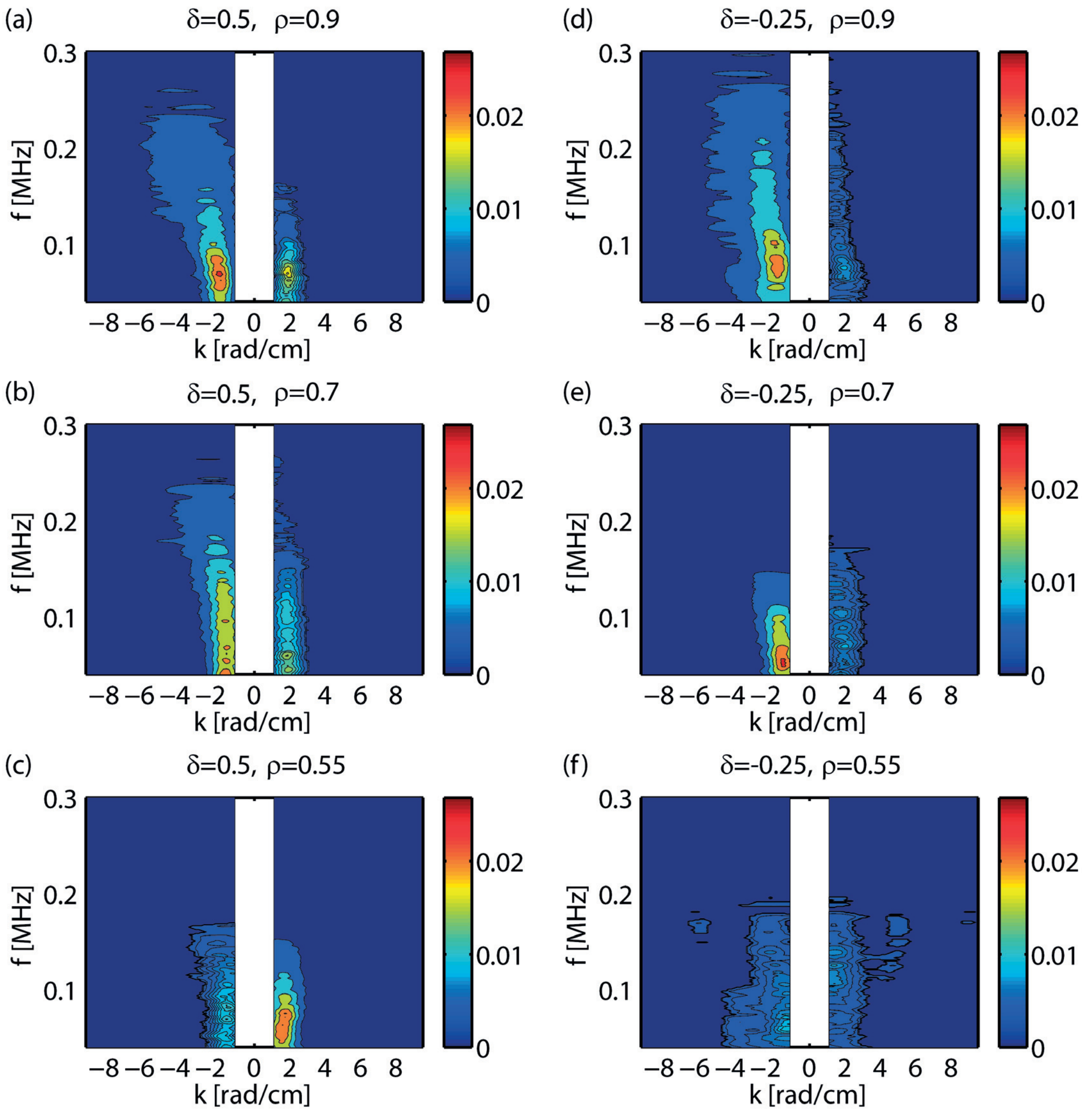

Figure 3.10: Conditional spectrum $s(k|f)$ of normalized density fluctuations $\tilde{n}/n$, with the same configuration as Fig. 3.9. The contours are drawn in linear scale with 10 kHz smoothing, and data with spectral power below 0.003 were neglected.

3.3.2 Results with matched profiles

Another set of 4 discharges were performed in the 2016 TCV campaign in an attempt to have the same profiles at two triangularities and two vertical positions for core and edge measurements. Similar core and edge electron temperature can be achieved with 0.9 MW EC central heating for $\delta = 0.55$ plasmas and with 0.2 MW EC central heating for $\delta = -0.5$ plasmas. Density control was applied to keep the line-integrated density at 1.2×10^{19} m^{-2} for $\delta < 0$, and at 0.9×10^{19} m^{-2} for $\delta > 0$. The difference in line-integrated density is due to the different integration length from shape difference, the goal being to have the same *line-averaged* density. The final achieved profiles are not exactly the same, as shown in Fig. 3.11. For each triangularity, two similar discharges were carried out at different vertical positions in order to have measurement both at core and edge. The major difference is in the density profiles as shown in Fig. 3.11 (c). The performance of the Thomson scattering system in these discharges was not optimal, in that there was a significant error bar in density which might be due to the misalignment of one laser. The time intervals for the analysis were selected such that the two other correctly functioning, independently triggered lasers of the Thomson system were used for measurement.

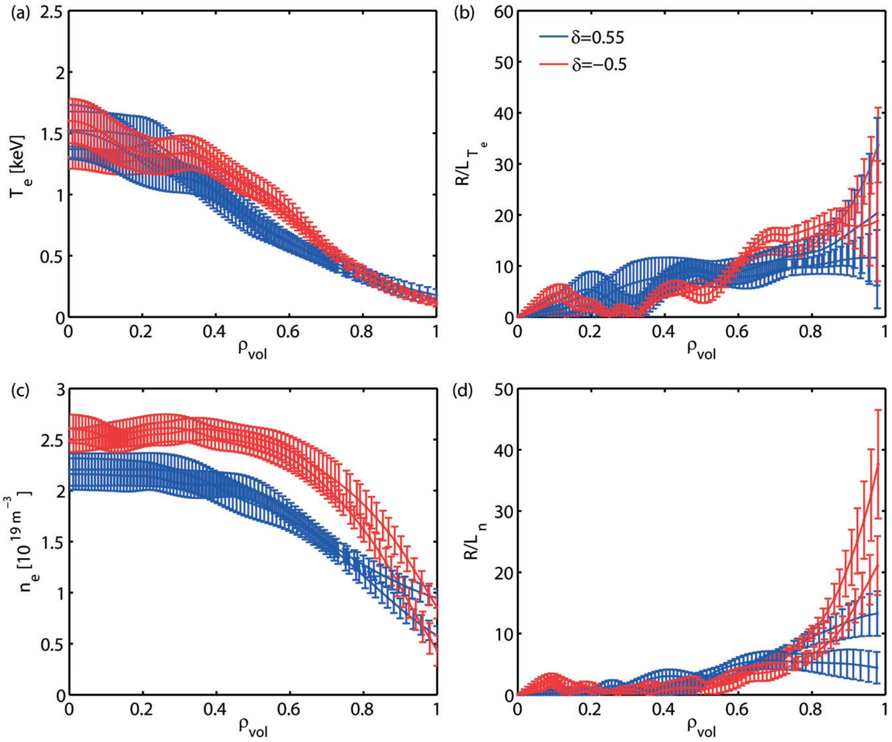

Figure 3.11: Radial profiles of (a) electron temperature, (b) normalized electron temperature gradient, (c) electron density ,(d) normalized density gradient, in TCV discharge #54565 and #54990 (blue) with $\delta = 0.55$, #55849 and #55850 (red) with $\delta = -0.5$.

Figure 3.11 (a) shows that the electron temperature profiles have similar values with more than 4 times heating power in the $\delta > 0$ plasma compared to $\delta < 0$, and the density is about

20% lower, as shown in Fig. 3.11 (c). The stronger heating indeed results in higher central temperature in $\delta > 0$, however in the range of $0.4 < \rho_{\mathrm{vol}} < 0.7$ where the $\delta > 0$ plasma meets the critical gradient at $R/L_{T_e} \approx 8 - 11$, as shown in Fig. 3.11 (b), the T_e profiles were exceeded by the $\delta < 0$ plasma, in which the same radial range is non-stiff. The stiff region for $\delta < 0$ is only from $\rho_{\mathrm{vol}} = 0.7$ to 0.8 at $R/L_{T_e} \approx 14$. Note that the value of critical gradients for both triangularities are similar to the ones discussed in the "equal power" approach previously, only the radial range of the stiff region is extended towards the plasma center for $\delta > 0$ with a higher heating power, and reduced for $\delta < 0$ with a lower heating power.

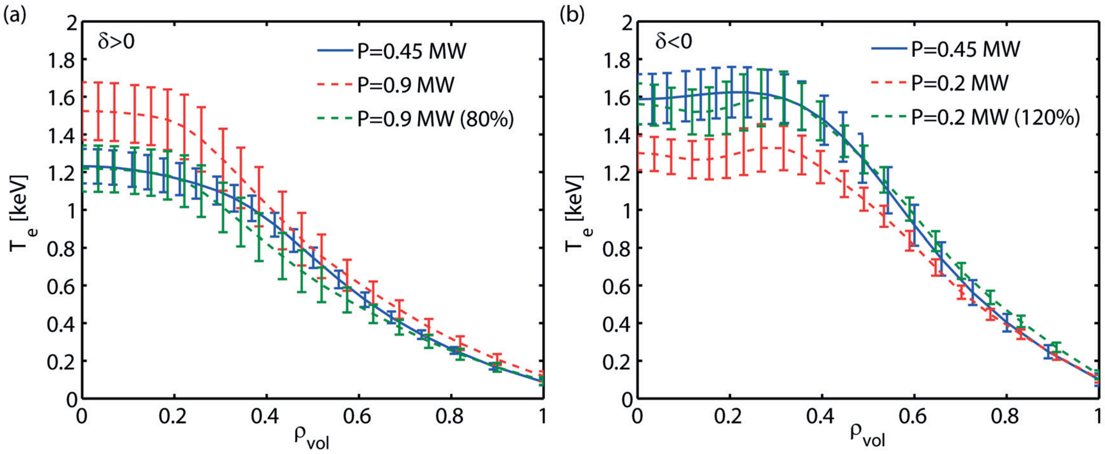

Figure 3.12: Radial T_e profiles of TCV discharges with (a) $\delta > 0$ and (b) $\delta < 0$. In both subplots the solid blue curves are with 0.45 MW EC central heating. In (a), the dashed red curve has 0.9 MW heating power and artificially decreasing it to 80% yields the green curve; in (b), the dashed red curve has 0.2 MW heating power and artificially increasing it to 120% yields the green curve.

Comparisons of the electron temperature profiles to the ones with 0.45 MW constant heating power for both $\delta > 0$ and $\delta < 0$ plasmas are shown in Fig. 3.12. It can be seen that the doubled heating power for $\delta > 0$ only increases by about 25% the temperature in the center and almost leaves it unchanged for $\rho_{\mathrm{vol}} > 0.4$: artificially decreasing the T_e profile of the plasma with 0.9 MW heating to its 80% can roughly match the central temperature, but have lower temperature in the core region for $0.3 < \rho_{\mathrm{vol}} < 0.8$. On the other hand, for the $\delta < 0$ plasma, by artificially increasing the T_e profile of the plasma with 0.2 MW heating to 120%, the temperature profile for $0 < \rho_{\mathrm{vol}} < 0.6$ can roughly be matched. This is consistent with the observation that the stiff region in R/L_{T_e} profile in $\delta < 0$ plasma is much narrower than $\delta > 0$. Figure 3.13 shows the relative density fluctuation amplitude $\tilde{n}/n$ measured by TPCI in the core ($\rho_{\mathrm{vol}} \approx 0.45$) and at the edge ($\rho_{\mathrm{vol}} \approx 0.75$). It can be seen that at the edge the $\delta > 0$ discharge has about twice as large a turbulence amplitude as the $\delta < 0$ discharge; in the core the reduction is less ($\sim 40\%$) but still substantial. The dependence of $\tilde{n}/n$ as a function of normalized gradients is shown in Fig. 3.14, with the results with 0.45 MW heating also drawn for reference. It can be seen that the density fluctuation amplitudes in the $\delta = -0.5$ plasmas are almost on the same curve as the reference, while for $\delta = 0.55$ they are slightly higher. It is necessary to note that the experiments were carried out in different TCV campaigns, and therefore the data points shouldn't be directly compared to the references. However this shows that the ratio of $\tilde{n}/n$ from $\delta > 0$ to $\delta < 0$ is slightly higher with similar profiles than with the same heating power.

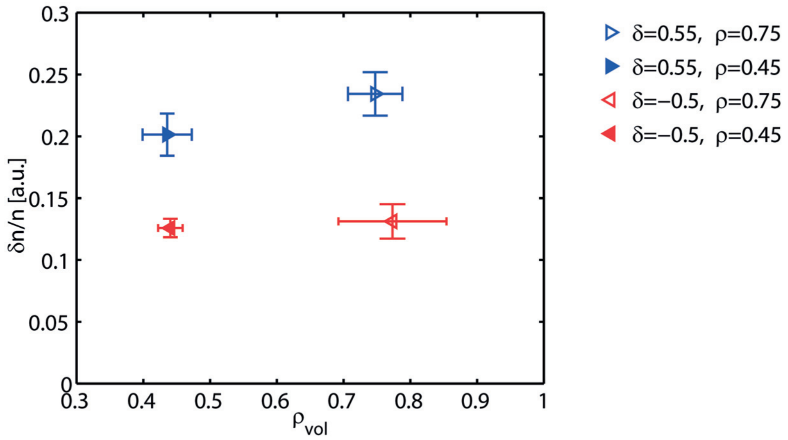

Figure 3.13: Relative density fluctuation amplitude $\tilde{n}/n$ as a function of radial position ρ_{vol} in the core (open symbols) and at the edge (solid symbols) in $\delta > 0$ (blue) and $\delta < 0$ (red) plasmas; the $\delta > 0$ discharge is with 0.9 MW ECH while the $\delta < 0$ discharge is with 0.2 MW ECH. Each data point is averaged over 100 ms with frequency resolution 1 kHz, normalized by the selected integration length and local density n [10^{19} m^{-3}] measured by the Thomson scattering system.

A similar reduction of turbulence amplitude and decorrelation time as in Sec. 3.3.1 can also be seen from the power spectrum at $f = 40 - 400$ kHz, as shown in Figs. 3.15 (a) and (b). The inverse-power-law exponent for $\delta > 0$ is -2.8 in the core and -2.2 at the edge from 80 to 140 kHz and around -1 for $f > 160$ kHz; for $\delta < 0$ in the core the spectrum follows a $f^{-2.3}$ scaling from 80 to 140 kHz, whereas in the high frequency part as well as in the entire frequency range at the edge the exponent is around -1.

As a conclusion for Sec. 3.3, the beneficial effect of negative triangularity on confinement is observed as a substantial (40 – 50%) reduction of turbulent density fluctuation amplitude, as well as of the decorrelation time and radial correlation length, over a large radial region from the plasma core to the edge in ECH L-mode plasmas. Plasmas with negative triangularity have a narrower and less stiff region with higher critical gradient values, compared to the ones with positive triangularity. Increase the heating power extends the stiff region further towards the core and thus further reduces the heating efficiency.

3.4 Impact of collisionality

The effective collisionality ν_{eff} plays an important role in the stability of TEMs, which have been predicted to be dominant in TCV ECH L-mode plasmas. The collisionality has been found to have a strong impact on electron heat transport experimentally and also from gyrokinetic simulations [7]. The dependence of heat transport on $1/\nu_{\mathrm{eff}}$ is approximately offset-linear.

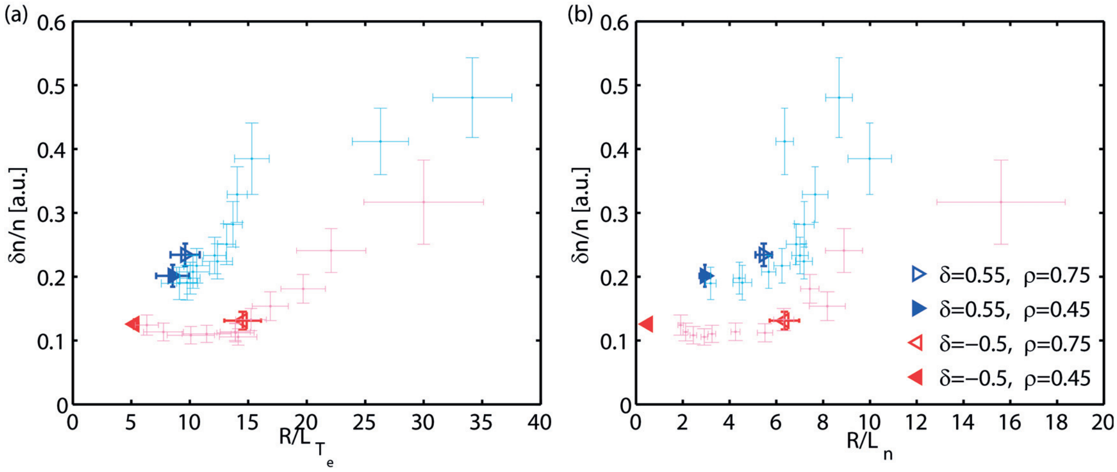

Figure 3.14: Relative density fluctuation amplitude $\tilde{n}/n$ as a function of normalized gradients R/L_{T_e} (a) and R/L_n (b) in the core (open symbols) and at the edge (solid symbols) in $\delta > 0$ (blue) and $\delta < 0$ (red) plasmas; the $\delta > 0$ discharge is with 0.9 MW ECH while the $\delta < 0$ discharge is with 0.2 MW ECH. The same curves (dots) of $\tilde{n}/n$ in Fig. 3.6 (c) and (d) are also drawn for reference. Each data point is averaged over 100 ms with frequency resolution 1 kHz, normalized by the selected integration length and local density n [10^{19} m^{-3}] measured by the Thomson scattering system.

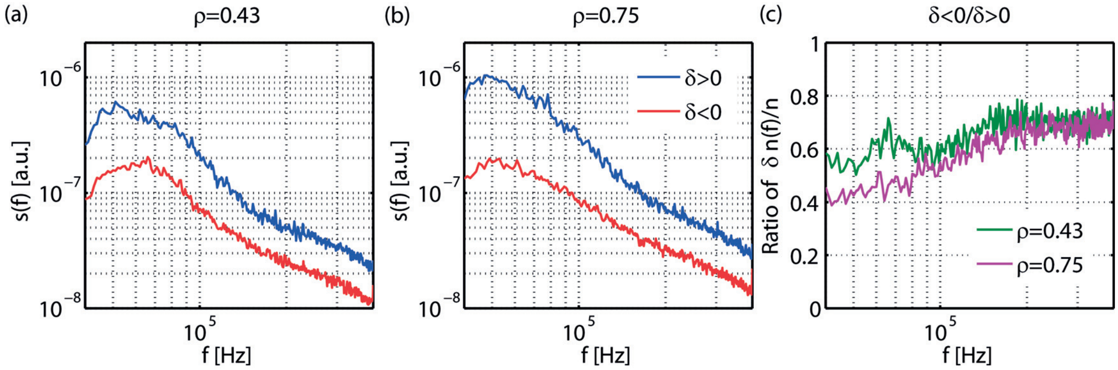

Figure 3.15: Power spectra of normalized density fluctuations $\tilde{n}/n$ at different radial positions: $\rho_{\text{vol}} = 0.43$ (a) and 0.75 (b). The spectra are averaged over 100 ms with frequency resolution 1 kHz, normalized by the square of the selected integration length and local density n [10^{19} m^{-3}]. (c) Ratio of $\tilde{n}/n$ spectral amplitude as a function of frequency between the two discharges.

The slope of the $1/\nu_{\mathrm{eff}}$ dependence varies with triangularity, that is, χ_{e} is more sensitive to ν_{eff} in a $\delta > 0$ plasma than in the $\delta < 0$ case; on the other hand, the triangularity effect tends to disappear when ν_{eff} is too high such as in high density Ohmic plasmas. The analysis of the collisionality effect needs to be made at similar radial positions. The first reason is that the impact of collisionality dominates in the range where the transport is independent of the normalized gradients [54]. In the edge plasma, although the collisionality is usually higher than in the core due to lower temperature, the turbulence level is still much higher because the critical gradients are exceeded and turbulence has a stronger dependence on gradients. In addition, as mentioned in Sec. 3.3.1, no radial profile measurement of Z_{eff} was available for the experiments, and Z_{eff} has a radial dependence.

In Sec. 3.4.1, we describe different results of density fluctuation measurements from two triangularity scans, one Ohmic and the other with 1.35 MW EC heating. The difference in the triangularity effect can be explained by including the impact of collisionality. More specific results from dedicated density and ECH power scans are described in Sec. 3.4.2.

3.4.1 Results from triangularity scans

In addition to the radial scans described in Sec. 3.3.1, triangularity scans from positive to negative δ in a single discharge were also performed. As mentioned in Sec. 3.2, due to the geometry of the TPCI diagnostic, the radial position of measurement changes in a δ scan even with the plasma at the same vertical position. The shift in ρ is larger at the outermost position, and can be neglected at $z = 0.23$ m.

Here we present the results from two discharges at $z = 0.23$ m, one Ohmic (#48971) and the other (#48972) with 1.35 MW ECH. The radial profiles of T_{e}, n_{e}, $R/L_{T_{\mathrm{e}}}$, R/L_{n} are shown in Fig. 3.16. The central electron temperature increased about $15-20\%$ in #48971 from $\delta > 0$ to $\delta < 0$, and about 40% in #48972. #48971 has twice the central density of #48972 and one third of the central electron temperature. Both discharges have stiff core T_{e} profiles: the radial range is $0.4 < \rho_{\mathrm{vol}} < 0.8$ in #48971 regardless the triangularity; in #48972 it is wider at $\delta = 0.5$ ($\rho_{\mathrm{vol}} = 0.25-0.6$), and the core is becoming non-stiff except for $\rho_{\mathrm{vol}} = 0.7-0.8$ at $\delta = -0.2$. In terms of density, on the other hand, #48971 does not have a stiff core, while for #48972 and $0.5 < \rho_{\mathrm{vol}} < 0.7$ the normalized density gradient is nearly constant.

The TPCI measurement is around $0.3 < \rho_{\mathrm{vol}} < 0.36$, where the profiles are mostly non-stiff, and thus the dependence of $\tilde{n}/n$ on the gradients can be neglected, except for #48972 when $\delta = 0.5$, as shown in Fig. 3.16. The plasma parameters at the radial location of measurement are listed in Table 3.1.

In Fig. 3.17 the relative density fluctuation amplitude is plotted as a function of edge triangularity δ (a) and $1/\nu_{\mathrm{eff}}$ (b). It can be seen that in #48971 $\tilde{n}/n$ decreases for about $15-20\%$ from ≈ 0.08 to 0.06, with δ changing from positive to negative, while the electron temperature increases roughly by the same percentage across the profile, as shown in Fig. 3.16 (a). In #48972, on the other hand, $\tilde{n}/n$ only decreases when δ drops from 0.4 to 0.3, then it stays at almost the same value throughout the discharge, even though the electron temperature has increased about 40%. This observation can be explained by including the impact of effective

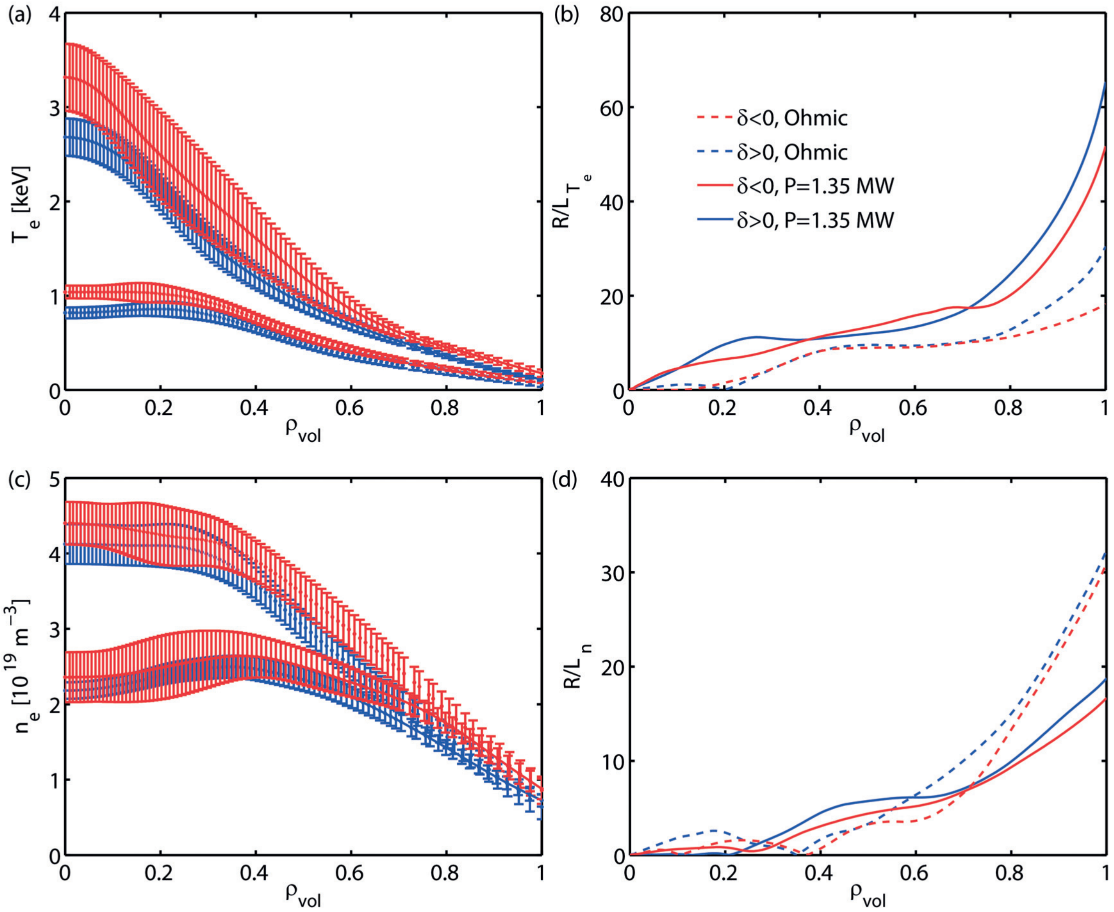

Figure 3.16: Radial profiles of (a) electron temperature, (b) normalized electron temperature gradient, (c) electron density ,(d) normalized density gradient, at the times when $\delta = 0.45$ (blue) and -0.22 (red) in an Ohmic triangularity scan #48971 (dashed) and an L-mode triangularity scan #48972 (solid) with 1.35 MW input power.

collisionality as shown in Fig. 3.17 (b). In an Ohmic triangularity scan, as δ decreases, the turbulence amplitude decreases as well, leading to a slight increase of both n and T_e, with little resulting change in collisionality. Note that in the Ohmic discharge the collisionality is high ($1/\nu_\mathrm{eff} \approx 1$), where the effect of triangularity is known to be small [7]. In the EC-heated discharge, the reduction in turbulence and transport engendered by a lower delta tends to increase the electron temperature T_e more, resulting in a higher $1/\nu_\mathrm{eff}$, which in turn increases the turbulence amplitude in a negative feedback loop. This is illustrated schematically by the arrows in Fig. 3.17 (b), in #48972 moving horizontally towards low collisionality without changing $\tilde{n}/n$, while in #48971 moving vertically.

The normalized frequency spectrum of TPCI measurements from $f = 40$ to 400 kHz in these two discharges is shown in Fig. 3.18. It can be seen that in #48971 the spectrum is peaked, the range of the peak shrinking from positive to negative δ from the low frequency side, with the peak frequency shifting from 100 to 150 kHz. For $f > 180$ kHz the spectra are essentially

Discharge type	T_e [keV]	n [10^{19} m^{-3}]	Z_{eff}	R/L_{T_e}	R/L_n	ν_{eff}
#48971, Ohmic	0.7 – 0.9	3.8 – 4.2	1.5 – 2.2	5.0 – 6.9	1.5 – 3.4	1.0 – 1.1
#48972, $P = 1.35$ MW	1.4 – 2.0	2.5 – 2.8	1.9 – 2.1	6.4 – 10.5	0.6 – 1.7	0.1 – 0.2

Table 3.1: Parameter range explored at the measurement radial position $\rho_{\text{vol}} = 0.33$, in two triangularity scan discharges.

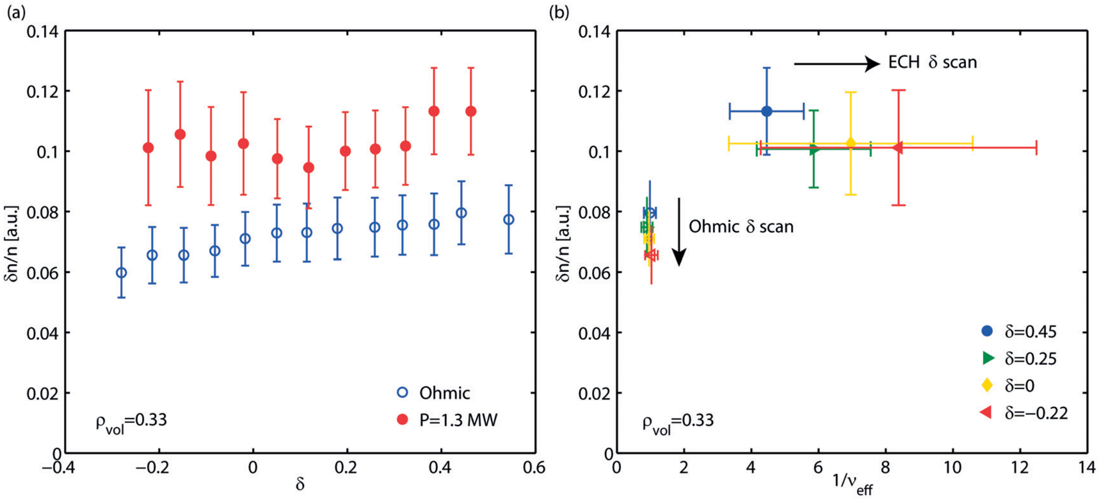

Figure 3.17: Relative density fluctuation amplitude $\tilde{n}/n$ as a function of triangularity δ (a) and reciprocal of effective collisionality $1/\nu_{\text{eff}}$ (b) in TCV discharges #48971 (blue) and #48972 (red); #48971 is Ohmic and #48972 features 1.35 MW EC heating in the plasma center. Each data point is averaged over 100 ms with frequency resolution 0.1 kHz, normalized by the selected integration length and local density n [10^{19} m^{-3}] measured by the Thomson scattering system.

identical. The reduction of turbulence amplitude therefore is dominated by the reduction in the low frequency range. The inverse-power-law exponent for $f > 220$ kHz is about −0.8, and for the fast decrease part from the peak to 200 kHz increases (in absolute value) from −2.8 to −4.4. In #48972, the only significant change in the frequency spectrum is from $\delta = 0.45$ to 0.25, where the low frequency part $f < 80$ kHz decreases, which corresponds to the initial drop of $\tilde{n}/n$ in Fig. 3.17. The reduction in decorrelation time at negative triangularity in Sec. 3.3.1 and Sec. 3.3.2 is not observed. This effect is presently not understood.

Figure 3.19 shows the k-spectra from the two triangularity scans. Here only the main peak at low k is presented. It can be seen that the $k > 0$ components are dominant in the core, which is the same as in previous cases. For #48971 in Fig. 3.19 (a), the spectral power of the $k > 0$ peak decreases during the δ scan without a change in the width, while in the frequency spectrum the range shrinks; for #48972 in Fig. 3.19 (b), the same decrease of spectral power for the $k > 0$ peak occurs from $\delta = 0.45$ (blue) to 0.25 (green), after which the width of the peak also starts to increase, i.e., the correlation length decreases, while the frequency spectrum remains largely unchanged in this range. This suggests that the negative triangularity can reduce the radial correlation length of the turbulence in the core of L-mode plasma, as shown previously

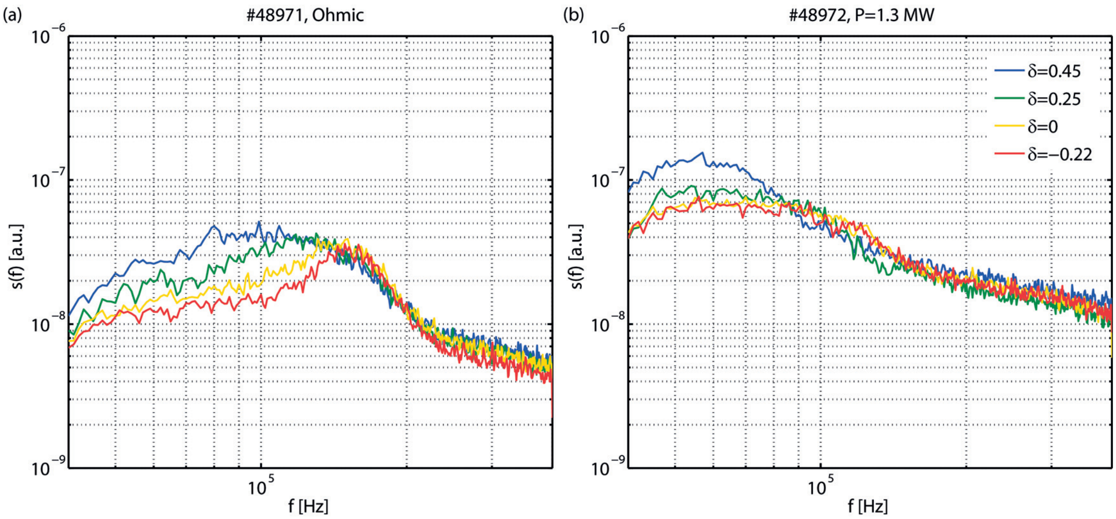

Figure 3.18: Power spectra of normalized density fluctuations $\tilde{n}/n$ at different triangularities: $\delta = 0.45$ (blue), 0.25 (green), 0 (yellow)and −0.22 (red) in TCV discharges #48971 (a) and #48972 (b). The spectra are averaged over 100 ms with frequency resolution 1 kHz, normalized by the square of the selected integration length and local density n $[10^{19}\ \mathrm{m}^{-3}]$.

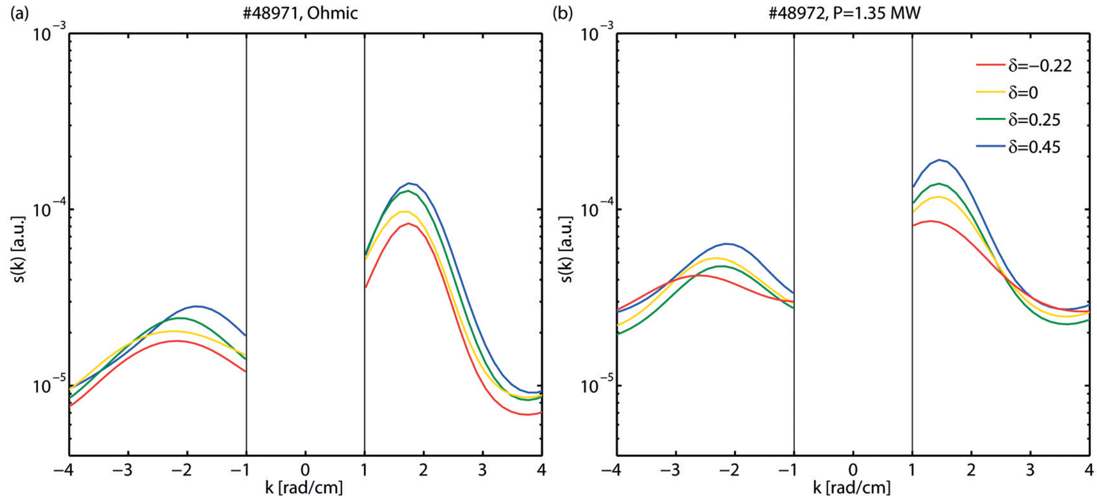

Figure 3.19: Wavenumber spectra of normalized density fluctuations $\tilde{n}/n$; the order of subplots and data integration time are the same as in Fig. 3.18. The blank region around $-1 < k < 1$ rad/cm indicates the instrumental cutoff; only the two main peaks at low k are presented.

in Fig. 3.8 (c), however not for the Ohmic plasma. Comparing the same colored curves in Figs. 3.19 (a) and (b), it can be seen the spectral width in k broadens from Ohmic to L-mode at $\delta < 0$ and doesn't change much at $\delta > 0$. The two dimensional frequency-wavenumber spectrum $s(k, f)$ and conditional spectrum $s(k|f)$ are plotted in Fig. 3.20 and 3.21. From the conditional spectrum of #48972 (right-hand side of Fig. 3.21), factoring out the absolute dependence on frequency spectrum, a similar frequency up-shift as in #48971 can also be observed from $\delta = 0.26$ to -0.22. In the spectrum $s(k, f)$, the information it contains has been mostly discussed earlier.

To summarize, in the core plasma where the local gradients are below the critical gradient, the impact of collisionality determines the turbulence amplitude. For a ECH L-mode plasma, because the temperature profile is non-stiff, the temperature with lower triangularity and thus better confinement can reach a higher value, until the decreased collisionality brings up the turbulence amplitude to the same level as higher triangularity cases; the improved confinement with negative triangularity can be characterized by reduced radial correlation length instead of the turbulence amplitude. On the other hand, for a TEM dominated Ohmic plasma, the triangularity effect only appears as a reduction in turbulence amplitude in the low frequency range, leaving the radial correlation length unchanged. This shows that the triangularity effect is less pronounced at high collisionality.

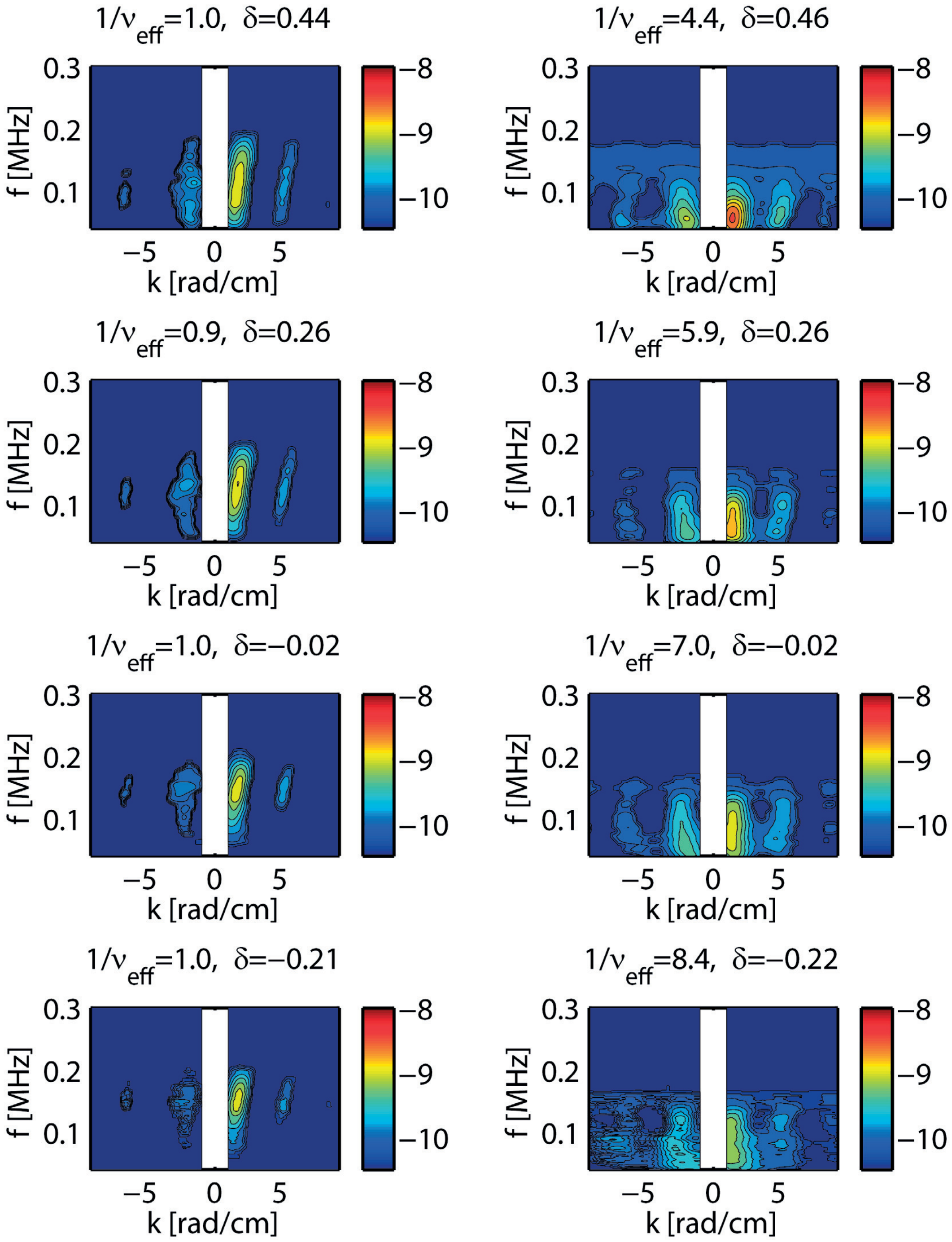

Figure 3.20: Two-dimensional frequency-wavenumber spectra $s(k, f)$ of normalized density fluctuations $\tilde{n}/n$ in #48971 (left) and #48972 (right) at $\delta = 0.45$ (top), 0.25 (second row), 0 (third row) and −0.22 (bottom). The integration time and frequency resolution are as in Fig. 3.18. The contours are drawn in logarithmic scale with 10 kHz smoothing; data with spectral power below 10^{-10} were neglected.

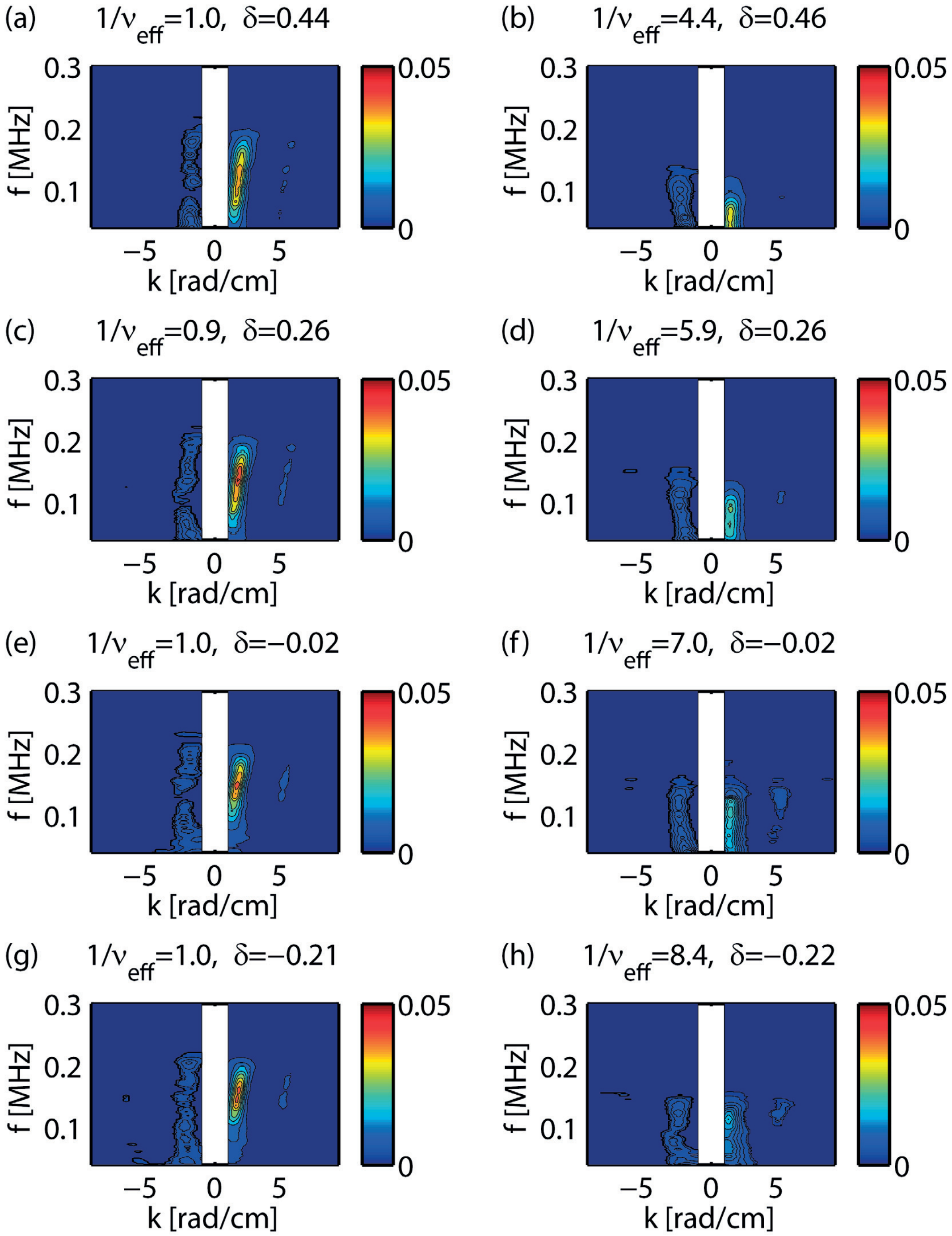

Figure 3.21: Conditional spectrum $s(k|f)$ of normalized density fluctuations $\tilde{n}/n$, with same configuration as Fig. 3.20. The contours are drawn in linear scale with 10 kHz smoothing; data with spectral power below 0.003 were neglected.

3.4.2 Results from collisionality scans

In order to investigate the impact of collisionality on density fluctuations, dedicated experiments including one Ohmic density scan with positive δ and two ECH power scans with both positive and negative δ were carried out. These discharges were performed around $z = 0.2$ m for core measurement around $\rho_{\mathrm{vol}} = 0.43$. In this radial range the normalized gradients $R/L_{\mathrm{T_e}}$ and R/L_{n} are typically below the critical gradient so that the dependence of $\tilde{n}/n$ on the gradients can be neglected. In fact, as shown in Table 3.2, the variation of local $R/L_{\mathrm{T_e}}$ and R/L_{n} are mostly within the range of ±1.5 for all 3 discharges with external ECH power varying from 0 to 1.2 MW. The absolute values are also well below the observed threshold ($R/L_{\mathrm{T_e}} = 10$ for $\delta > 0$ and 14 for $\delta < 0$) for turbulence increase shown in Fig. 3.6. The effective collisionality $\nu_{\mathrm{eff}} \propto T_{\mathrm{e}}^2/(n_{\mathrm{e}} Z_{\mathrm{eff}})$ in the core plasma, on the other hand, varies significantly enough to have a strong impact on heat transport, as shown in Fig. 3.2.

Discharge type	T_e [keV]	n [10^{19} m^{-3}]	Z_{eff}	$R/L_{\mathrm{T_e}}$	R/L_{n}	ν_{eff}
$\delta > 0$, n scan	$0.4 - 0.7$	$3.2 - 7.1$	$1.4 - 2.0$	$4.7 - 6.3$	$1.7 - 3.4$	$1.3 - 4.5$
$\delta > 0$, P scan	$0.7 - 1.1$	$2.9 - 3.0$	$2.1 - 2.5$	$5.5 - 7.8$	$1.6 - 2.7$	$0.5 - 1.1$
$\delta < 0$, P scan	$1.1 - 1.6$	$2.4 - 3.0$	$4.2 - 4.7$	$4.8 - 6.9$	$0.2 - 2.0$	$0.3 - 0.9$

Table 3.2: Parameter range explored at measurement radial position $\rho_{\mathrm{vol}} = 0.43$, in the study of the impact of collisionality on density fluctuations.

The normalized density fluctuation amplitude $\tilde{n}/n$ measured by TPCI is plotted as a function of $1/\nu_{\mathrm{eff}}$ in Fig. 3.22, for two triangularities $\delta \approx 0.5$ and $\delta \approx -0.4$. The four innermost points from the $\delta = -0.25$ radial scan \$49051 are also included, below the critical gradient. The reduction in $\tilde{n}/n$ with increasing ν_{eff} can be observed for both triangularities, while at the same ν_{eff} the $\delta > 0$ discharge has higher fluctuation amplitude than the $\delta < 0$ one. The difference in $\tilde{n}/n$ between the two triangularities is smaller at high collisionality, especially when $1/\nu_{\mathrm{eff}} < 1$. This result is consistent with previous experimental observations on electron heat transport [7], and also with the observations in Ohmic triangularity scan in Sec. 3.4.1. Indeed Fig. 3.2 [7] and Fig. 3.22 show very a similar trend for turbulence and transport as functions of effective collisionality. It must nevertheless be pointed out that the radial position of turbulence measurements is further inside ($\rho = 0.43$) than the transport experiments ($\rho = 0.55$). In addition, the increase of turbulence amplitude moving inward for the 3 innermost points in #49051 (see Fig. 3.6 (b)) can also be explained: the effective collisionality is lower further in the core due to higher temperature, resulting in a higher $\tilde{n}/n$, which is independent of $R/L_{\mathrm{T_e}}$ below the critical gradient.

The data for $\delta > 0$ (blue) in Fig. 3.22 show that the increase of turbulence amplitude is mainly around $0.5 < 1/\nu_{\mathrm{eff}} < 1.5$, which corresponds to the transition from low density Ohmic phase to low ECH power L-mode phase. In fact, while P_{ECH} has increased from 0.6 to 1 MW, most data in the $\delta > 0$ power scan are localized around $1/\nu_{\mathrm{eff}} = 1.5$. The local electron temperature and density keep nearly constant around $T_{\mathrm{e}} = 0.9 - 0.95$ keV, $n = 3 \times 10^{19}$ m^{-3}. On the other hand, the same range of ECH power applied to the $\delta < 0$ discharge doubles $1/\nu_{\mathrm{eff}}$ from 1.5 to

3. For the $\delta > 0$ Ohmic density ramp (blue open symbols), it can be seen that $\tilde{n}/n$ has almost no change at high density with $1/\nu_{\text{eff}} < 0.5$. The vanishing effect of ν_{eff} might be due to the dominant turbulence type changing from TEM to ITG during the LOC-SOC transition.

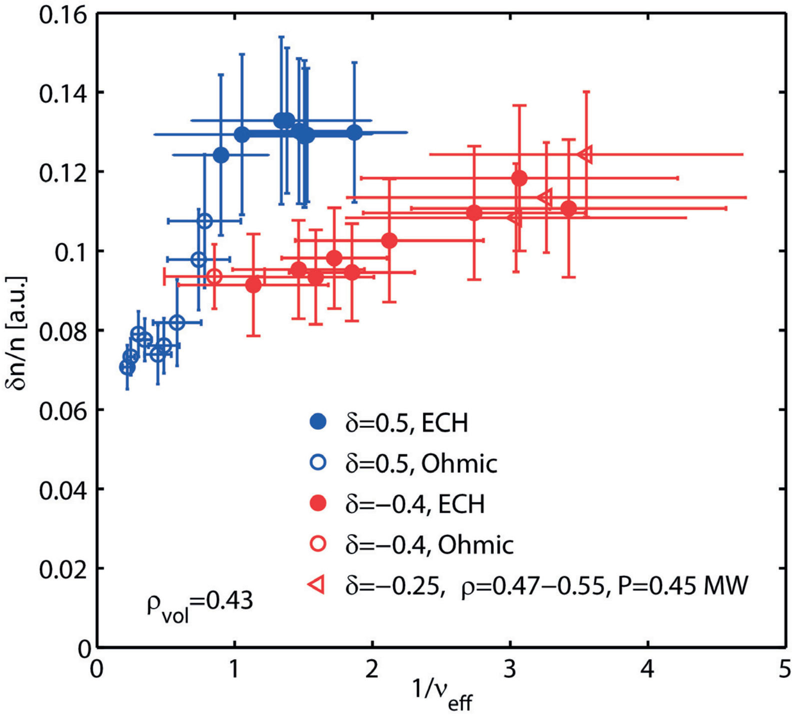

Figure 3.22: Relative density fluctuation amplitude $\tilde{n}/n$ as a function of the reciprocal of effective collisionality $1/\nu_{\text{eff}}$ in $\delta = 0.5$ (blue) and $\delta = -0.4$ (red), Ohmic (open symbols) and ECH L-mode (full symbols) TCV discharges. Each data point is averaged over 100 ms with frequency resolution 0.1 kHz, normalized by the selected integration length and local density n [10^{19} m^{-3}] measured by the Thomson scattering system.

To compare the turbulence spectra during the ν_{eff} scan between the two triangularities, we selected 3 different times: the first one is without external heating at $1/\nu_{\text{eff}} = 0.8$, the second one is with 0.6 MW heating power at $1/\nu_{\text{eff}} = 1.1$, and finally one at $1/\nu_{\text{eff}} = 1.8$ which is the lowest collisionality achieved in the $\delta > 0$ discharge. The power spectra of normalized density fluctuations at $f = 40 - 400$ kHz are plotted in Fig. 3.23. One additional curve (purple) in the high density Ohmic discharge before the LOC-SOC transition, i.e., in still TEM dominant conditions, at $1/\nu_{\text{eff}} = 0.5$ was added in Fig. 3.23 (d); the spectrum from the lowest collisionality achieved in the $\delta < 0$ discharge at $1/\nu_{\text{eff}} = 3$ (red) is also added in Fig. 3.23 (e).

Figures. 3.23 (a,b,c) show that the difference in the spectral power between the two triangularities is mainly in the low frequency range $f < 150$ kHz, whereas the $\tilde{n}/n$ ratio in the high frequency range is around unity as shown in Fig. 3.23 (f). The difference at $f < 150$ kHz is much larger with EC heating than in the Ohmic case, as has been discussed before in connection with Fig. 3.22. Figure 3.23 (d) shows that for the $\delta > 0$ plasma, from the high density to the low density Ohmic phase $1/\nu_{\mathrm{eff}}$ increases from 0.5 to 0.8, and the spectral power increases in the entire frequency range. It peaks around 90 – 100 kHz and the inverse-power-law exponent from 100 to 150 kHz is about −3.5. When the EC heating is applied, at $1/\nu_{\mathrm{eff}} = 1.1$, the flat and maximal region of the spectrum expands, and the exponent in 100 – 150 kHz increases (in absolute value) to −4.6; the peak of the spectrum shifts to lower frequency as the ECH power increases, and the exponent goes to −4 at $1/\nu_{\mathrm{eff}} = 1.8$. The high frequency range in $f > 200$ kHz always has a roughly $f^{-0.8}$ dependence. For the $\delta < 0$ case as shown in Fig. 3.23 (e), almost no difference can be observed from $1/\nu_{\mathrm{eff}} = 0.8$ to 1.8, except the peak of the spectrum expands to the low frequency side and shifts from centered at 90 kHz to around 70 kHz. The spectral power increases in the entire frequency range when $1/\nu_{\mathrm{eff}}$ increases from 1.8 to 3. A $f^{-1.1}$ dependence can be observed throughout the discharge in the range $f > 100$ kHz. Comparing the spectra of $\delta > 0$ and $\delta < 0$ again shows a reduction of decorrelation time with negative triangularity, and the change in collisionality does not change the shape of the spectrum much. The reduction in turbulence amplitude is only in the low frequency range, while the high frequency range the ratio of $\tilde{n}/n$ is close to 1, as shown in Fig. 3.23 (f).

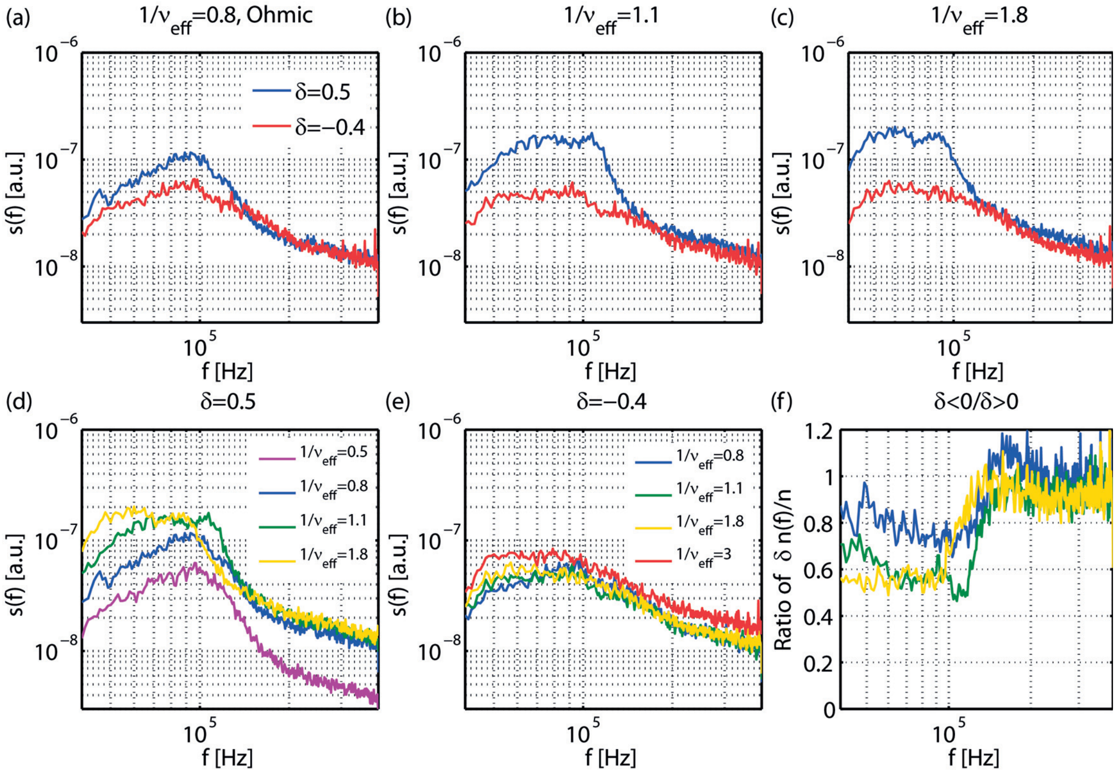

Figure 3.23: Power spectra of normalized density fluctuations $\tilde{n}/n$ at $\rho_{\mathrm{vol}} = 0.43$ at different collisionalities: $1/\nu_{\mathrm{eff}} = 0.8$ (a), 1.1 (b), 1.8 (c) in $\delta = 0.5$ and $\delta = -0.4$ discharges; same spectra overlaid for the $\delta = 0.5$ case (d) and the $\delta = -0.4$ case (e), in each case with one additional collisionality value added. The spectra are averaged over 100 ms with frequency resolution 1 kHz, normalized by the square of the selected integration length and local density n [10^{19} m^{-3}]. (f) Ratio of $\tilde{n}/n$ spectral amplitude as a function of frequency between the two triangularities.

Figures 3.24 and 3.25 show the two dimensional frequency-wavenumber spectrum $s(k,f)$ and conditional spectrum $s(k|f)$. We focus on the conditional spectrum in Fig.3.25 especially for the $\delta > 0$ case. It can be seen that the $k > 0$ component dominates, which is as expected from the trends observed in the radial scans shown in Fig. 3.10, although the measurement in the ν_{eff} scan is more inside. The down-shift of the frequency spectrum discussed before can be seen here too, and the amplitude actually decreases slightly after factoring out the absolute dependence on frequency. For the $\delta < 0$ discharge, the Ohmic $\delta < 0$ phase in Fig 3.25 (b) is the only one with a measurable signal. It has the $k < 0$ component peaking < 100 kHz and the $k > 0$ component peaking around 150 kHz, which resembles the conditional spectrum in Fig. 3.10 (f) with similar plasma condition. It is also visible that the spectrum width of the $\delta < 0$ discharge becomes wider with ECH comparing to the Ohmic case, while for the $\delta > 0$ discharge it does not change, as shown in Fig. 3.19.

To summarize, turbulent density fluctuations are also dependent on effective collisionality. The turbulence amplitude increases with the reciprocal of the collisionality above $1/\nu_{\text{eff}} = 0.5$, consistent with the stabilizing effect of collisionality on TEM-type turbulence; the decorrelation time is independent of the collisionality. The dependence of turbulence amplitude on $1/\nu_{\text{eff}}$ varies with triangularity: the increase of turbulence amplitude is faster for $\delta > 0$ than for $\delta < 0$; at the same collisionality, the $\delta < 0$ plasma features a reduction in turbulence amplitude in the low frequency range; the triangularity effect is more pronounced at low collisionality. These results are consistent with previous observations on electron heat transport. As discussed in previous section, the less pronounced triangularity effect at high collisionality might be due to the vanishing effect of radial correlation length reduction.

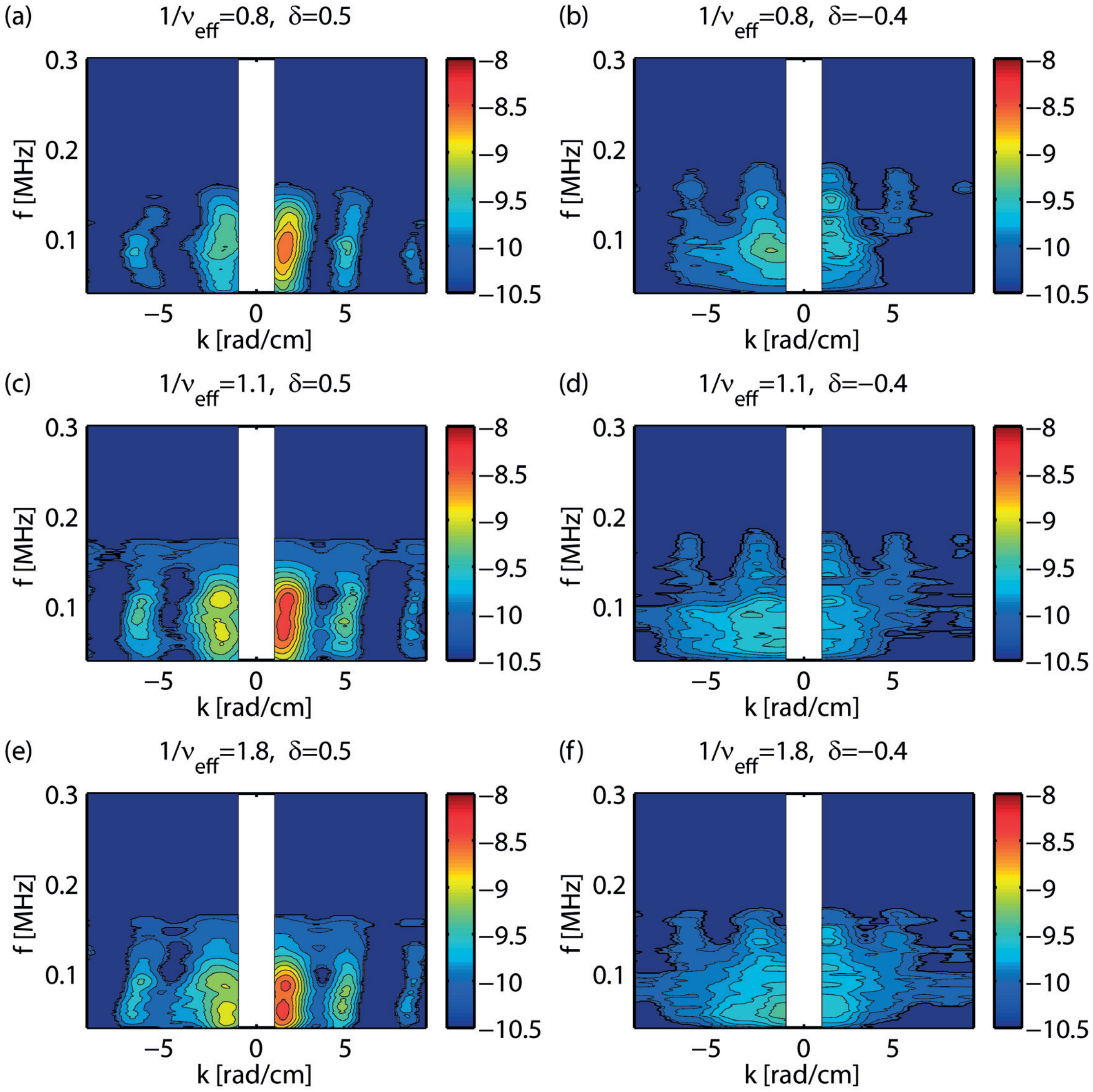

Figure 3.24: Two-dimensional frequency-wavenumber spectra $s(k,f)$ of normalized density fluctuations $\tilde{n}/n$ in $\delta = 0.5$ (left) and $\delta = -0.4$ (right) discharges at $1/\nu_{\text{eff}} = 0.8$ (top), 1.1 (middle) and 1.8 (bottom). The integration time and frequency resolution are as in Fig. 3.23. The contours are drawn in logarithmic scale with 10 kHz smoothing, data with spectral power below 10^{-10} were neglected.

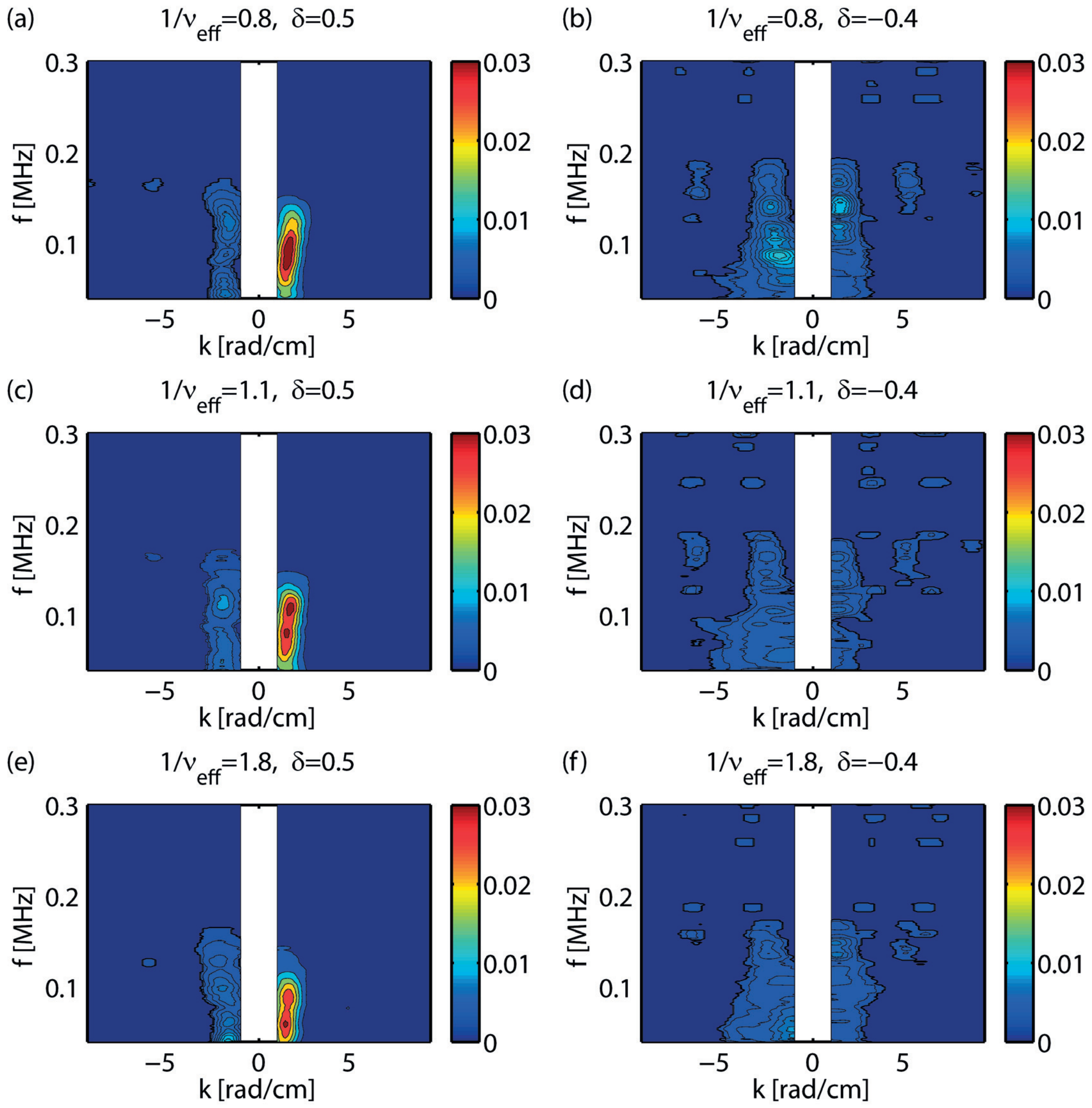

Figure 3.25: Conditional spectrum $s(k|f)$ of normalized density fluctuations $\tilde{n}/n$, with same configuration as Fig. 3.24. The contours are drawn in linear scale with 10 kHz smoothing; data with spectral power below 0.003 were neglected.

4 The geodesic acoustic modes in the TCV tokamak

The geodesic acoustic mode (GAM) [21] is a finite frequency branch of zonal flows (ZFs) [12, 13]. The zonal flows are excited exclusively by nonlinear interactions among all types of microinstabilities and in turn regulate transport the shear-decorrelation mechanism [15]. Understanding the turbulence/ZF self-organization mechanism is an important issue in magnetic confinement fusion research.

A full characterization of the GAMs in TCV has been reported and compared with gyrokinetic simulations performed with ORB5 [8]. The experimental results from this first phase of GAM investigations on TCV are reviewed in Sec. 4.1. Section 4.2 describes a transition from the local continuum regime to the radially extended regime observed in a single discharge in TCV, with comparisons to global non-linear gyrokinetic simulations. In Sec. 4.3, the interaction between the GAMs and the turbulence during a density ramp-up were investigated by bispectral techniques, and a quasi-coherent mode was also observed and characterized. Finally, in Sec. 4.4 we report the first observations of GAMs in the SOL by Langmuir probes, magnetic probes and D_α emission.

4.1 Multi-field characterization of GAMs

In TCV, the experimental investigations of GAMs started in the 2011 TCV campaign with the observations of the density component of the GAMs by the TPCI diagnostic. The studies were then extended in the 2013 TCV campaign to multiple fluctuating components of the GAMs: the $E \times B$ flow component measured by the Doppler backscattering diagnostic (DBS), the magnetic component by the magnetic probes, and the temperature component by the correlation ECE diagnostic.

The GAMs are essentially azimuthally symmetric ($n = 0$, $m = 0$) sheared zonal flows with a finite frequency. The propagation velocity of the fluctuating $\tilde{E} \times B$ flow was measured by the DBS system (see Sec. 2.3.2). The injection angle and incident frequency of the microwave beam were chosen to have the backscattering flux surface close to the LCFS where the GAM amplitude peaks. The backscattered radiation was Doppler-shifted by $\Delta\omega_\mathrm{D} = k_\perp v_\perp$: after subtraction of the mean velocity, the only statistically significant feature of the power spectrum

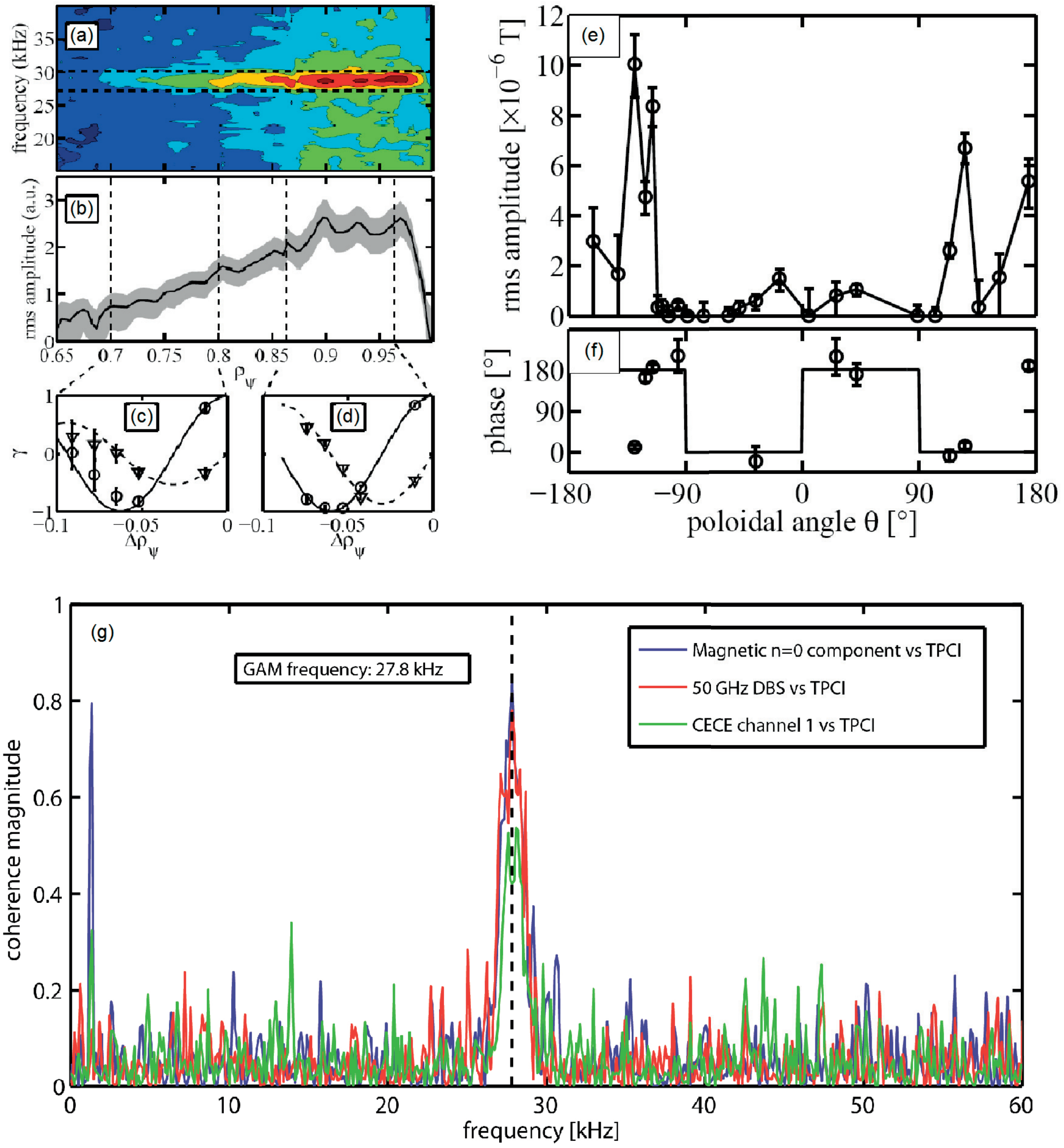

Figure 4.1: Auto-power spectrum (a), amplitude (b), real and imaginary parts of the complex coherence at the GAM frequency (c,d) of the density fluctuations measured by TPCI. GAM amplitude (e) and cross-phase (f) measured by magnetic probes. (g) squared coherence between the magnetic $n = 0$ component (blue), DBS (red) and cECE (black) to TPCI signals. The dashed line indicates the GAM frequency. [8]

of the propagation velocity was a peak at the GAM frequency. The GAMs had been detected by both the 50 – 75 GHz (V-band) system from LPP [43] and the 45 GHz (U-band) instrument from FZJ.

The pressure sideband, coupled with the flow component, has been predicted to be up-down-antisymmetric ($n = 0$, $m = 1$), as experimentally verified by reflectometry density fluctuation measurements in TEXTOR [55]. The density component of the GAM in TCV was measured by the TPCI system, with the spatial filter angle optimized for edge radial wave-vector measurements. Vertical shifts were performed in order to resolve the entire radial distribution of the GAM. The GAM has measurable amplitude for $\rho > 0.65$, with the peak located near the LCFS at $\rho \sim 0.95$, as shown in Fig. 4.1 (a,b) [8]. The frequency was found to be constant in the entire radial range of existence of the mode, over which the ion sound speed varies by a factor of 1.7. The radial wavenumber was around 2 rad/cm, i.e., $k\rho_s \approx 0.4 - 0.5$, predominantely outward propagating.

The temperature component, as the other possible contributor to the pressure sideband, was also detected by the cECE diagnostic in the edge plasma for $\rho > 0.78$. Some discrepancies were found between the density and temperature components: the radial wavenumber is 0.9 rad/cm inferred according to cECE; the propagation direction is found to be inward instead of outward; the GAM can be measured at the equatorial plane by ECE where the density component is predicted to be at a node. It is necessary to note that the estimated optical thickness at the edge is low and thus both electron temperature and density fluctuations contribute to the ECE signals. Gyrokinetic simulations from GENE [53] also suggest that the temperature and density components of the GAM might have different structures: the $\tilde{T}$ component has 2 dominant poloidal mode numbers $m = 0$ and $m = 1$, with anti-node on the midplane.

The magnetic component of the GAM has been predicted by MHD calculations [30], and observed by the magnetic probes in TCV. It was also reported from the DIII-D [25], T-10 [27] and Globus-M [56] tokamaks. The axisymmetric nature ($n = 0$) of the GAM was unambiguously confirmed from the symmetric component of 8 probes from the HFS toroidal array. The probes on the poloidal array showed 2 dominant anti-nodes at the HFS top and bottom wall (roughly $\theta = \pm 135°$), 4 nodes at the equatorial plane ($\theta = 0°$ and $180°$), as well as top and bottom vessel ($\theta = \pm 90°$); the cross phase with the $n = 0$ signal also shows a $m = 2$ standing wave structure, as shown in Fig. 4.1 (e,f). The hypothesis that the disappearance of the other 2 anti-nodes at the LFS wall $\theta = \pm 45°$ was related to the shape of the plasma ($\delta > 0$) was later verified by the observation of the 2 LFS anti-nodes in a $\delta < 0$ plasma in the 2016 campaign. Additional poloidal modes were also predicted from the MHD model extension to non-circular plasmas [29].

The GAM is observed coherently by all the 4 diagnostics, as shown in Fig. 4.1 (g). Here the $\tilde{n}$ component is used as reference, and the squared coherence at the GAM frequency between different components is around 0.6 – 0.8.

Initial studies of the GAMs on TCV [8] were mainly in limited L-mode plasmas, in which the GAMs appear mostly in the form of a radially extended single-frequency regime, as shown in Fig. 4.1 (a). On the other hand, although the measured GAM frequency is independent of *local* temperature, it still roughly follows the scaling law when the plasma temperature

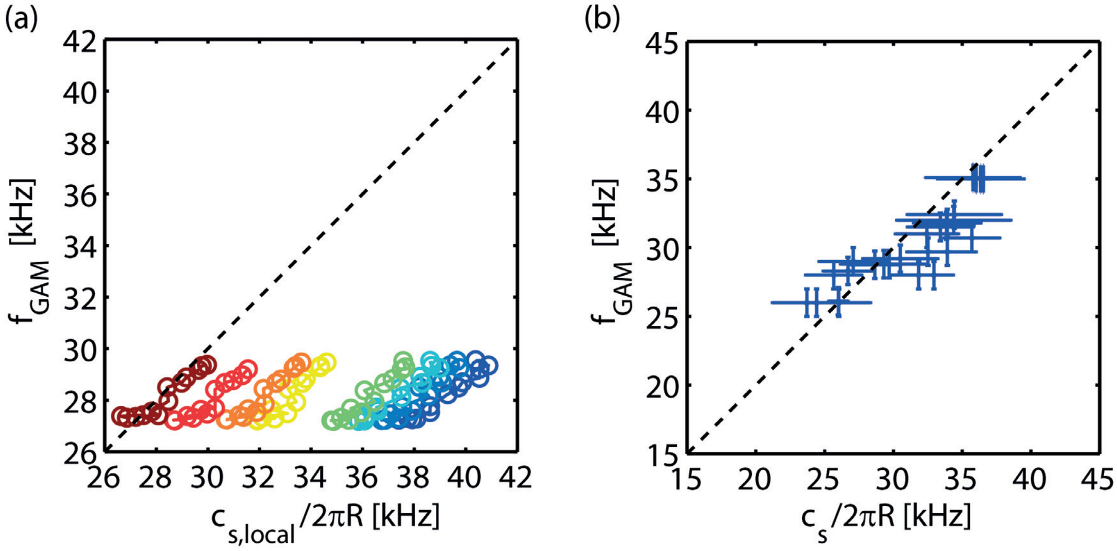

Figure 4.2: (a) Measured GAM frequency versus normalized ion sound speed in an ECH power scan, c_s calculated using local T_e measured by Thomson scattering. Different colors denote 8 different measurement chords of TPCI. (b) Same plot for a set of TCV discharges with T_e measured at $\rho = 0.95$.

is changed *globally*. Fig. 4.2 (a) shows the measured GAM frequency in a ECH power scan by 8 different chords of TPCI. The measured mode frequency roughly scales with the local calculated frequency at the outermost chord, where the GAM amplitude peaks as shown in Fig. 4.1 (b). The mode frequency measured by other inner chords is the same as the one at the outermost chord, thus lower than the theoretical frequency (dashed line). Fig. 4.2 (b) shows the measured GAM frequency by magnetic probes from the TCV database versus calculated GAM frequency using T_e measured at $\rho = 0.95$.

4.2 The radial structure of the GAM

The radial distribution and dispersion of GAMs differ between experiments. A continuum of GAM spectra has long been reported in many tokamaks [57]; in this case the mode frequency depends on radius according to the local analytical formula and following the radial variation of the temperature. In other cases however, radially extended regimes are also observed, i.e., a mode frequency that stays constant over a significant radial extent. In some cases there are several discrete coexisting frequencies [22, 25], whereas in others a single-frequency [26, 8, 27] is observed.

Analytical work [28] has shown that finite Larmor radius effects lead to the existence of global GAM eigenmodes, which tentatively could explain the observations. However, for the TCV experiments reported here, the single frequency regime is observed in regions below the local GAM frequency, whereas analytical theory predicts a propagation of the global GAM in regions above the local GAM frequency. Other possible explanations include a radially extended

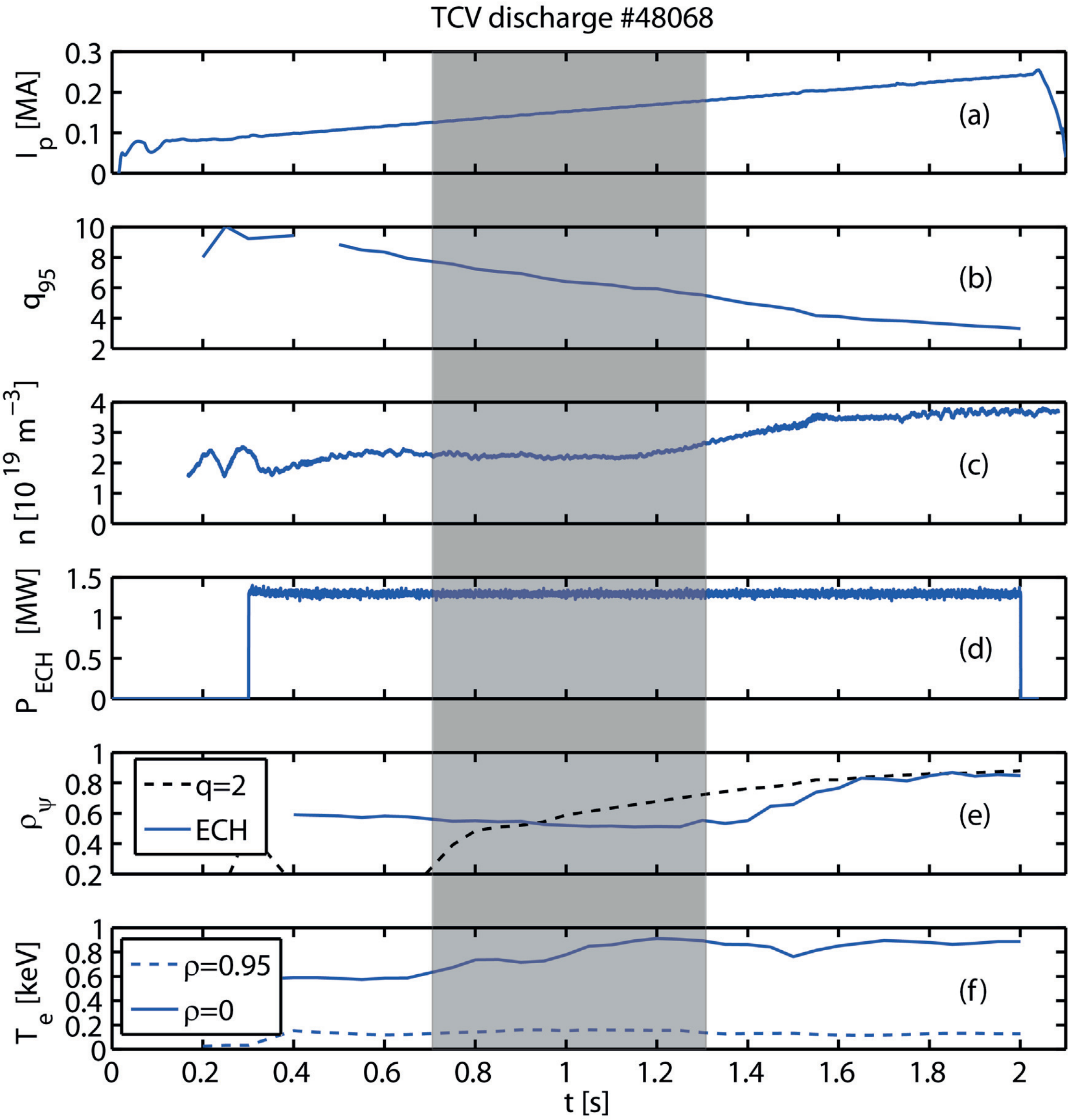

Figure 4.3: Time traces of (a) plasma current, (b) safety factor at 95% of poloidal magnetic flux, (c) line-averaged density from far infrared interferometer, (d) total ECH input power, (e) radial location of $q = 2$ surface and ECH absorption layer, (f) electron temperature measured by Thomson scattering at $\rho_\psi = 0$ and 0.95 in TCV discharge 48068. The shaded region indicates the time window for GAM regime transition analysis.

dominant component associated with the continuum GAM [29]. The mode observed in TCV, however, also has many features that would match the theoretical predictions for avalanches. However the identification of the mode in TCV as a global GAM [8] was driven by several observations: the axisymmetry, the magnetic $m = 2$ standing-wave dependence and the fact that its frequency varies globally proportionally to the square root of the temperature. Further, the continuum GAM regime is mutually exclusive with the radially extended regime. Further work in simulations and experiments appears necessary to identify and explain the mode, and if it is an avalanche, to understand its relation with the GAM, explaining the properties described above.

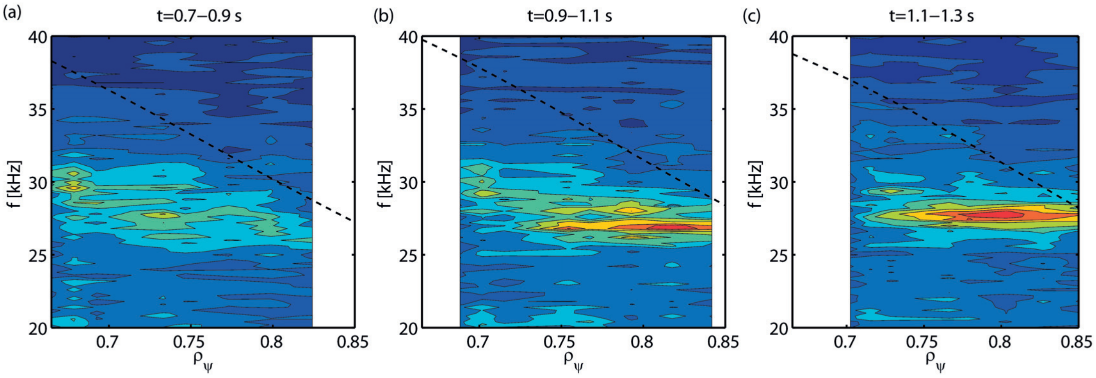

Figure 4.4: Auto-power spectrum of density fluctuations from TPCI measurement with 0.2 kHz frequency resolution in TCV discharge 48068. The dashed line indicates the analytical local GAM frequency.

A regime transition between continuum and single-frequency was observed in an ECH L-mode discharge in the course of a plasma current ramp-up. An overview of the plasma parameters for this shot is shown in Fig. 4.3. The Thomson scattering system measures a central density $n \approx 4 \times 10^{19}$ m^{-3}, while the edge density at $\rho_\psi = 0.95$ is around 1.2×10^{19} m^{-3}; the electron temperature T_e increases from 600 to 900 eV in the center while remaining relatively constant around 150 eV at $\rho_\psi = 0.95$; I_p increases from 100 to 180 kA during the transition, corresponding to a q_{95} ramp-down from 8 to 5.5; the shape of the plasma is nearly constant during the ramp, with edge elongation $\kappa = 1.52$ and triangularity $\delta = 0.5 - 0.6$. Three X2 ECH beams, each with 450 kW power, are injected into the plasma and the resonance layer is at $\rho_\psi = 0.5$. The ECH power is absorbed outside the $q = 2$ rational surface before $t = 0.9$ s and inside the $q = 2$ surface after.

The transition from the GAM continuum to a radially extended regime starts at about $t = 0.9$ s. The radial profile of the GAM during the transition is illustrated in Fig. 4.4, measured by 8 parallel chords of TPCI laser. The radial range of the measurement slightly changes during the time due to a shift of plasma vertical position. At $t = 0.7 - 0.9$ s, the GAM appears mainly as a frequency continuum with multiple distinguishable eigenmodes, the overall frequency being higher at small ρ and lower outside. From $t = 0.9$ s to 1.1 s, a mode at 27 kHz starts to dominate outside $\rho = 0.74$, with another, weaker, coexisting mode at 28.4 kHz; in the region $\rho < 0.74$ the mode frequency is still dependent on radius. Finally at $t = 1.1 - 1.3$ s, the GAM has fully developed into a coherent structure at 27.6 kHz over a radial range from $\rho = 0.72$ out to the outermost position of the measurement at $\rho = 0.85$. Another 29.4 kHz mode can still be observed only on the innermost chord. The measured frequency is always lower than the local analytical GAM frequency $f = \sqrt{2 + 1/q^2}\, c_s / 2\pi R$ (the dashed line in Fig. 4.4). Note that the mode frequency tends to match the analytical prediction at the outermost radial position. The radial wave number of the GAM density component measured by TPCI is $k_\rho = 2\ \mathrm{cm}^{-1}$, outward propagating, which is consistent with previous observations [8].

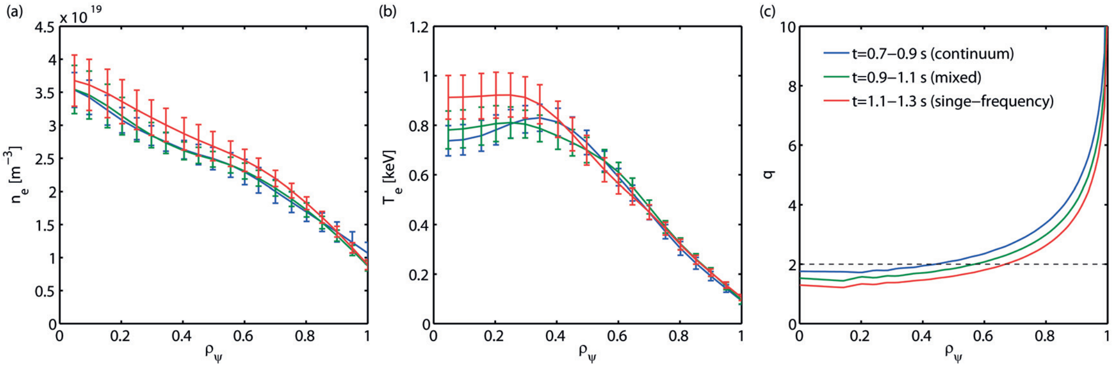

Figure 4.5: Electron density (a) and temperature (b) profiles of TCV discharge #48068 over the time range of GAM regime transition.

Local and global nonlinear gyrokinetic simulations have been performed with GENE with reference profiles from TCV experimental plasmas of both GAM continuum and radially coherent mode cases. Nonlinear flux-tube simulations show that the $E \times B$ velocity oscillation frequency is always dependent on the local temperature with both reference profiles, however downshifted from the local analytical GAM frequency. Results from nonlinear global simulations on the other hand are fairly consistent with experimental observations: a coherent, mostly outward propagating, single-frequency oscillation of the flux surface averaged $E \times B$ velocity is found to exist over the radial range from $\rho = 0.65$ to the simulation boundary, with T, n and q profiles from the radial extended GAM time slice; while the GAM frequency follows the local Rosenbluth-Hinton prediction with profiles from the GAM continuum time slice [53]. The origin of different GAM regimes can potentially be the different q profiles, and also different temperature and density as well as the corresponding gradient profiles, which would affect the turbulence driving the GAM. And in this discharge the ECH deposition position was passing the $q = 2$ surface at $t = 0.9$ s when the transition from continuum to radially extended mode started; however, the overall T_e and n_e profiles only increased after $t = 1.1$ s, except the edge density gradient, which already increased after $t = 0.9$ s, as shown in Fig. 4.5. In order to distinguish the two effects, another global nonlinear GENE run was carried out with mixed conditions: T and n profiles from the radially extended GAM time slice, and q profile from the continuum GAM time slice. The results show that in this case the GAM is in the radially extended regime. In contrast, the results from the simulation with reversed condition, i.e., T and n profiles from the continuum GAM discharge and q profile from the radially extended GAM time slice, show that the GAM is in the continuum regime [53]. Therefore the conclusion is that simply varying the safety factor is not sufficient to induce the transition from continuum to radially extended regime.

4.3 GAM-turbulence coupling in a density ramp-up

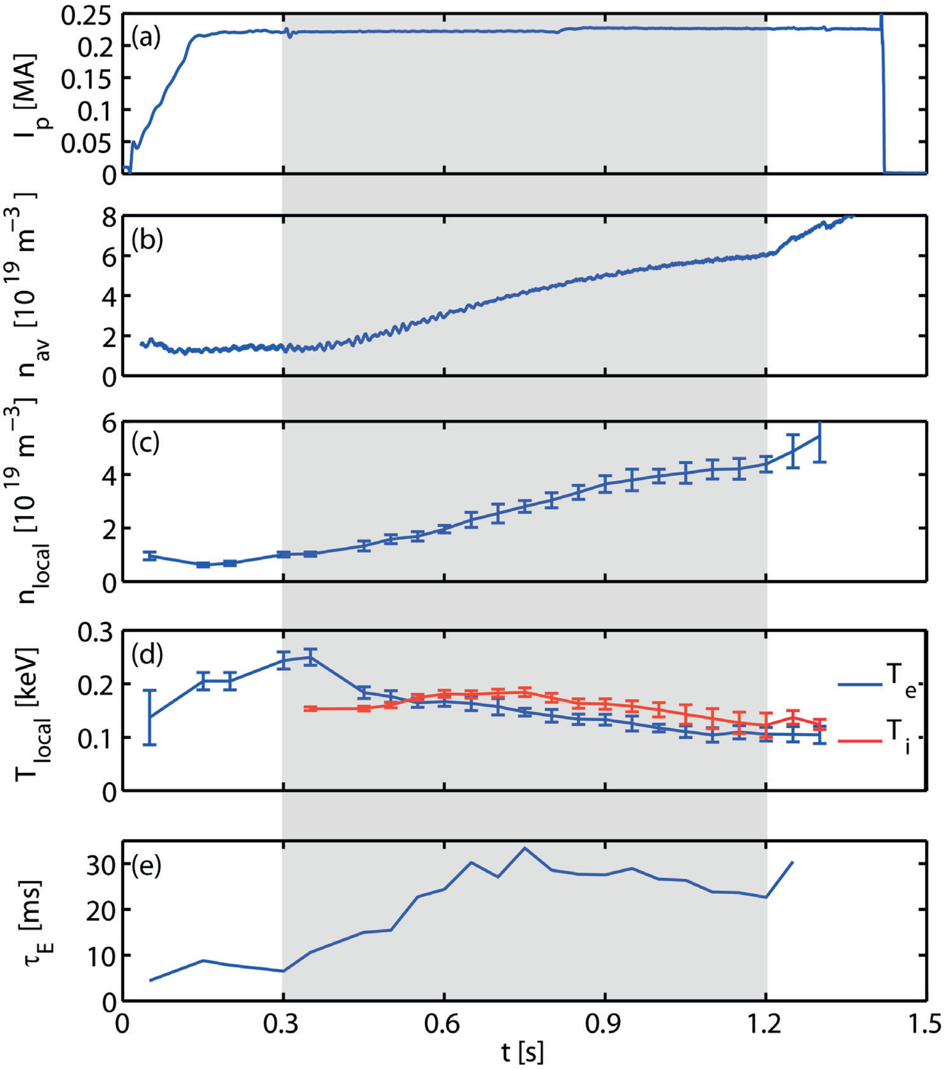

Figure 4.6: Time traces of (a) plasma current, (b) line-averaged density from far infrared interferometer, (c) local ($\rho_\psi = 0.9$) density measured by Thomson scattering, (d) local ($\rho_\psi = 0.9$) electron (blue) and ion (red) temperature measured by Thomson scattering and CXRS, respectively, (e) energy confinement time in TCV discharge 46068. Shaded region indicates the time range for analysis.

The GAMs, like the zero-frequency zonal flows, are driven by the nonlinear interactions within microinstabilities. The damping mechanism of the GAMs include Landau damping and collisional damping. In order to investigate the damping of GAMs, plasma current ramp-up to increase the Landau damping, or density ramp-up to increase the collisional damping can be performed. However, either a q scan or n scan would inevitably change the plasma profiles and turbulence level, which would in turn change the drive of the GAMs. Therefore, the interactions between the GAMs and the turbulence must be also taken into account to complete the study. The bispectrum analysis technique was employed to study the nonlinear coupling between GAMs and turbulence.

The drive and damping of GAMs are investigated in TCV discharge #46068 featuring a density ramp-up. An overview of the plasma parameters for this shot is shown in Fig. 4.6. The Thomson scattering system measures the central density increasing from 2 to 5×10^{19} m^{-3} from $t = 0.3$ to 1.2 s, while the edge density at $\rho_\psi = 0.9$ where the TPCI measurement is located is around 1 to 4×10^{19} m^{-3}. The local electron temperature T_e decreases from 250 to 100 eV, while the local ion temperature first increases from 150 to 180 eV at $t = 0.75$ s, then decreases to 120 eV. The electron/ion temperature ratio falls below 1 from $t = 0.55$ s. The plasma current and shape keeps nearly constant: $I_\mathrm{p} = 220$ kA, $\kappa = 1.4$ and $\delta = 0.4$. The energy confinement time first increases during the Ohmic density ramp from 10 to 30 ms, then keeps nearly constant. This indicates that the plasma is initially in the Linear Ohmic Confinement (LOC) regime and then in the Saturated Ohmic Confinement (SOC) regime.

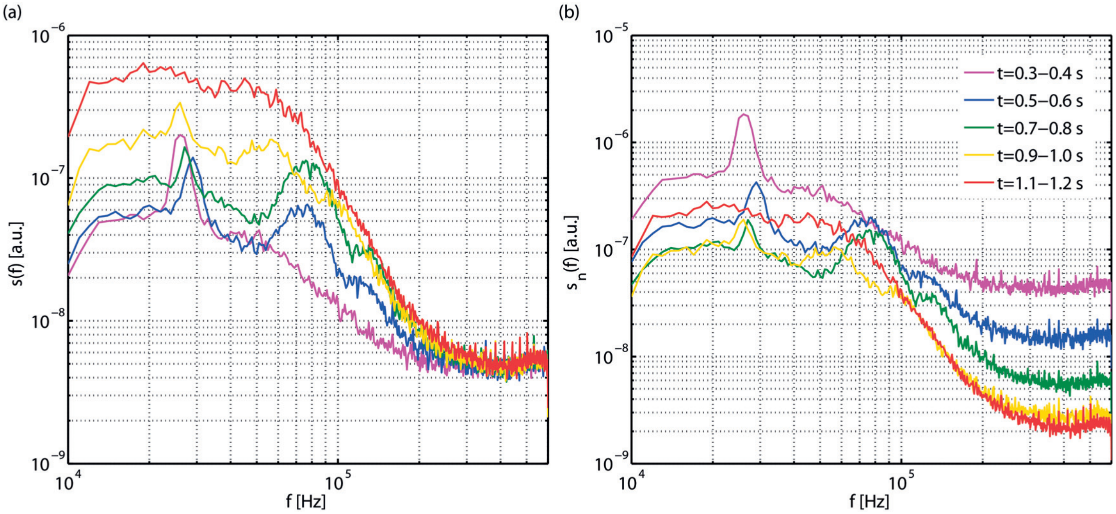

Figure 4.7: Power spectra of density fluctuations $\tilde{n}$ (a) and normalized density fluctuations $\tilde{n}/n$ by the square of local density n [10^{19} m^{-3}] (b). Each spectrum was calculated over 100 ms time window with 1 kHz frequency resolution.

The power spectra of density fluctuations $\tilde{n}^2$ and normalized density fluctuations $(\tilde{n}/n)^2$ are shown in Fig. 4.7 (a) and (b), respectively. The GAM peaks around 25 – 30 kHz, it is detectable until $t = 1.1$ s. Another more broadband quasi-coherent mode (QCM) can also be observed from $t = 0.5$ to 1 s centered around 60 – 80 kHz. From the conditional spectrum in Fig. 4.8 (b,c,d) it can be seen that this mode is coherent in the wavenumber space with nearly the same wavenumber as the GAM, however it is mainly inward propagating, which is opposite to the GAM. The coupling between the GAM and the turbulence is illustrated in the bicoherence spectrum in Fig. 4.9. From $t = 0.3$ to 0.6 s the bicoherence amplitude at the GAM frequency is visible, indicating the nonlinear coupling between the GAM and the turbulence. There is no significant bicoherence visible at $t = 0.6-0.7$ s, which is much earlier than the disappearance of the GAM on the frequency spectrum, however roughly coincides with the LOC-SOC transition time as shown in Fig. 4.6.

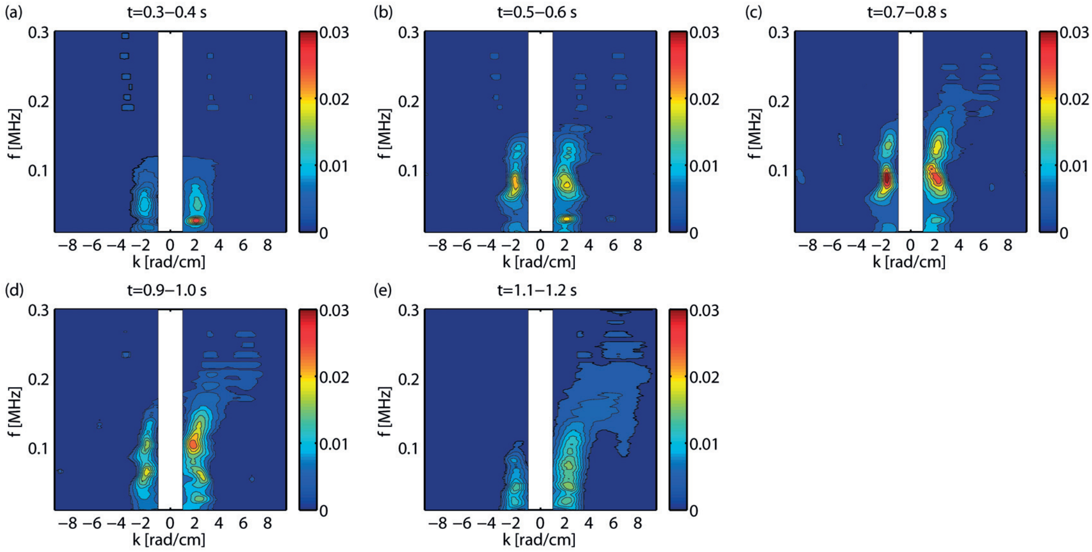

Figure 4.8: Conditional spectrum of TCV discharge #46068 from $t = 0.35$ s (a) to $t = 1.15$ s (e). The figures from (a) to (e) correspond to the same 5 selected time windows as in Fig. 4.7. Each spectrum was calculated over 100 ms time window with 1 kHz frequency resolution. The contours are drawn in linear scale with 10 kHz smoothing, data with spectrum power below 0.003 were neglected.

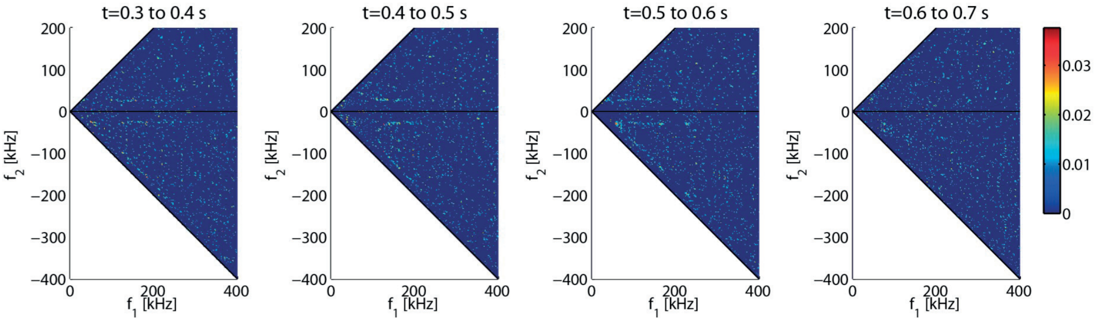

Figure 4.9: Squared auto-bicoherence in density fluctuations measured by TPCI of TCV discharge #46068 from $t = 0.3$ to 0.6 s. The bicoherence falls below the noise floor in $t = 0.6-0.7$ s. Each spectrum was calculated over 100 ms time window with 2 kHz frequency resolution.

Recent research from Tore Supra and TEXTOR [58, 59] has suggested a link between the QCM, TEM-type turbulence and LOC-SOC transition. Figure 4.10 (b) shows that the LOC-SOC transition happens around $n_{\mathrm{av}} = 4 \times 10^{19}$ m^{-3}. Correspondingly, the normalized broadband turbulence amplitude decreases with the density during the LOC regime and then keeps nearly constant, as shown in Fig. 4.10 (a). Figure 4.10 (c) shows that the normalized amplitude of the

QCM slight increases with the density and reaches its peak before the LOC-SOC transition, then it starts to decrease and finally vanishes from the spectrum. In the LOC regime, the increased collisionality leads to an increase in collisional electron-to-ion energy transfer and a decrease in electron and ion temperature ratio, as shown in Fig. 4.10 (d): the local ($\rho_\psi = 0.9$) T_e/T_i drops below 1 around $n_{av} \approx 2.5 \times 10^{19}$ m^{-3}, and drops further until entering the SOC, then it stays nearly constant in the SOC regime. Flux-tube gyrokinetic simulations [53] have also suggested that the dominant turbulence type changes from TEM at $n_{av} \approx 1.3 \times 10^{19}$ m^{-3}, to TEM-ITG mixed at $n_{av} \approx 3 \times 10^{19}$ m^{-3}, and finally to ITG at $n_{av} \approx 4.8 \times 10^{19}$ m^{-3}. This indicates that the fraction of ITG-type turbulence increases during the LOC regime and finally becomes dominant in the SOC regime. The disappearance of QCM in the ITG dominated SOC regime is consistent with the observations from Tore Supra and TEXTOR [59]. The relative amplitude of the GAM is similar to the trend of the broadband turbulence: it decreases during the LOC regime, but not damped with the increased collisionality in the SOC regime, instead it stays nearly constant. Even in the LOC regime when the GAM amplitude decreases with the density, the reason could still be the reduced broadband turbulence level and also less pronounced nonlinear coupling between the GAM and turbulence as shown in Fig. 4.9.

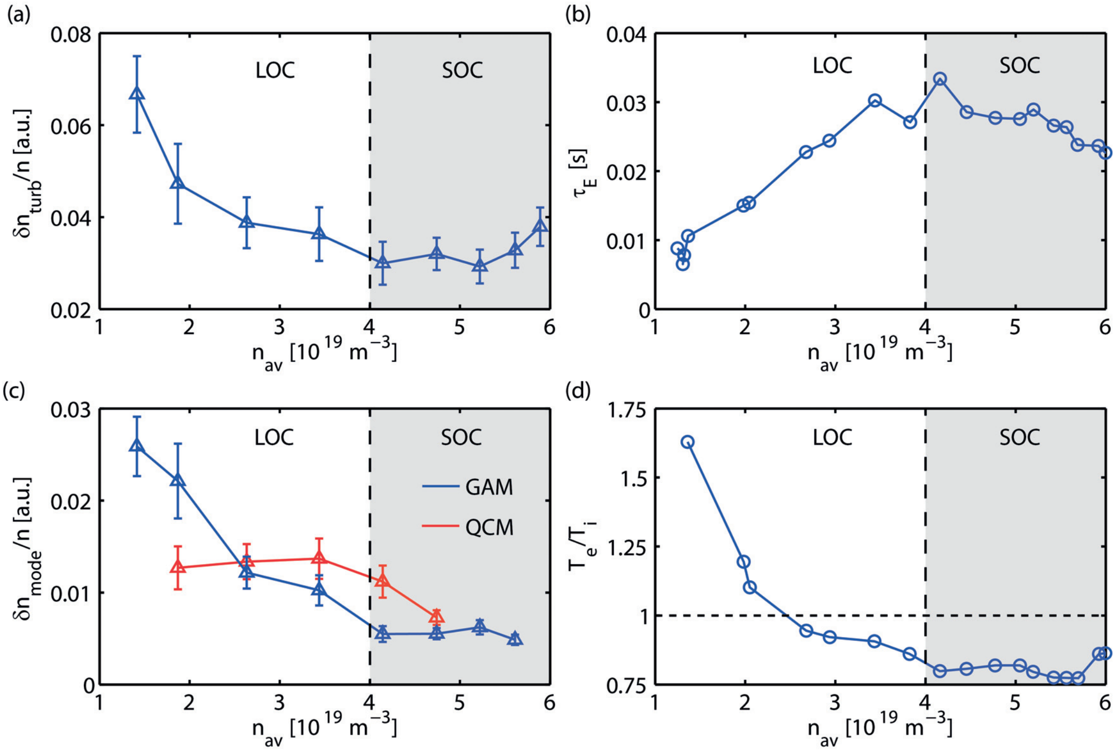

Figure 4.10: (a) Normalized broadband density fluctuation amplitude, (b) energy confinement time, (c) mode power of the GAM (blue) and the QCM (red), (d) local electron and ion temperature ratio as a function of the average plasma density [10^{19} m^{-3}] in TCV discharge #46068.

4.4 GAM-type oscillations in the scrape-off layer

In the 2016 TCV campaign, GAM-type oscillations were detected in divertor L-mode discharges by several scrape-off layer (SOL) diagnostics: magnetic probes (pickup coils) and Langmuir probes near the strike points, and also D_α emission signals. In order to understand these GAM-type oscillations, multi-diagnostic measurements have once again been performed: TPCI is employed for measurement of conventional GAMs inside the LCFS; the $\tilde{I}_{\mathrm{i,sat}}$ component is measured at the strike points by Langmuir probes; the $\dot{\tilde{B}}_\theta$ component can be detected on magnetic probes at the two conventional strong $m = 2$ anti-nodes at the HFS wall, as well as at the strike points, as shown in Fig. 4.11; on D_α emission, GAM-type oscillations are observed mainly along the vertical line-of-sight channel, but also sometimes on the lateral line-of-sight channel in the bottom part of the vessel when the mode is strong enough.

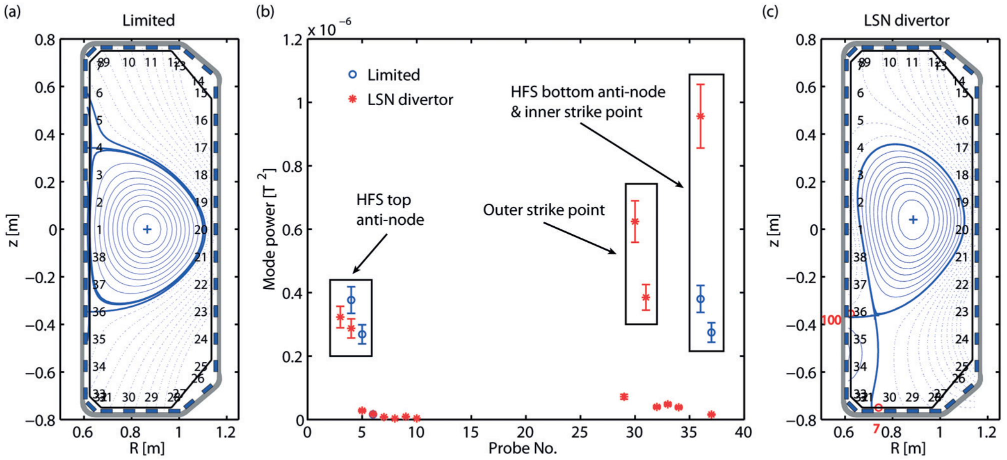

Figure 4.11: Plasma equilibrium of a limited #49052 (a) and a LSN divertor #52020 (c) TCV discharge. (b) GAM mode power on magnetic probes measured in these two discharges, calculated over a 100 ms time window with 1 kHz frequency resolution, subtracted from background turbulence.

4.4.1 Mode identification

The characteristics of these oscillations are found to be consistent with the standard GAM in three different aspects: frequency scaling, axisymmetry and mode-turbulence interactions, as illustrated in Fig. 4.12. Figure 4.12 (a) shows the spectrogram of a magnetic probe signal in an Ohmic discharge featuring a density ramp, at the outer strike point on the vessel floor; since this location is a node of the $m = 2$ magnetic component, the signal is assumed to be solely from the additional SOL component. The GAM frequency scales with the square root of the plasma temperature, and thus decreases during the Ohmic density ramp-up. As in this case the GAM appears as a radially extended mode, the calculated frequency uses T_e at $\rho = 0.95$, which is usually the outer limit of the GAM radial range. The other mode at 6 kHz is an MHD mode. Fig. 4.12 (b) and (c) show the squared coherence and cross phase between a reference magnetic probe and the other 7 in the bottom toroidal HFS bottom array. The coherence is close to unity at the GAM and the MHD mode frequency; the cross phases at the GAM frequency are all zero, while at the MHD mode frequency vary from $-\pi$ to π. This shows that the toroidal mode number of the GAM is $n = 0$. Finally, Figs. 4.12 (d) and (e) illustrate the strong bicoherence between the mode and the broadband turbulence from magnetic probes at the outer strike point, indicating nonlinear coupling between the mode and the turbulence. Therefore these modes are identified as GAMs.

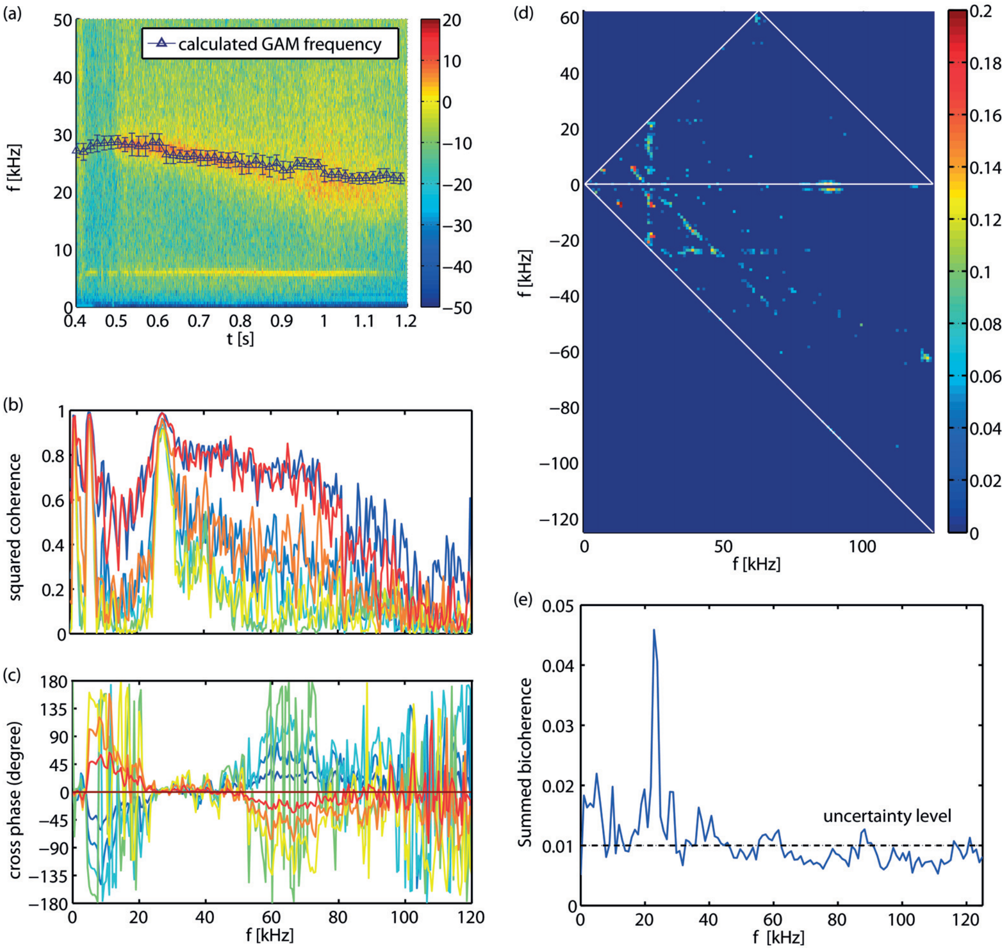

Figure 4.12: (a) Auto-power spectrogram of magnetic fluctuations at outer strike point in TCV discharge 52020 (the discharge with a density ramp); the triangle markers indicate the analytical GAM frequency. (b),(c) Squared coherence and cross phase of magnetic fluctuations between a reference magnetic probe and the other 7 in the toroidal HFS bottom array in TCV discharge 54490, calculated over a 40 ms time window with 0.5 kHz frequency resolution. (d),(e) Squared bicoherence (only points with bicoherence larger than statistical uncertainty level are shown) and summed bicoherence of magnetic fluctuations at outer strike point in TCV discharge 54490, calculated over a 100 ms time window with 1 kHz frequency resolution.

4.4.2 Coherence and cross phase between different components

The coherence and cross phase between these GAMs observed at the outer strike point and the conventional GAMs at the plasma edge inside LCFS are shown in Fig. 4.13 (a,b). The selected magnetic probe and Langmuir probe are both at the outer strike point (see Fig. 4.13 (c)), and the $\dot{\tilde{B}}$ and $\tilde{I}_{\mathrm{i,sat}}$ components are found to be in phase. The TPCI signal is obtained at $\rho_\psi = 0.97$; the coherence between this density component inside the LCFS and the SOL components at the GAM frequency is around 0.2. This value is well below what is usually measured in limited discharges between magnetic and TPCI signals (typically 0.8) [8], however the peak is clearly distinguishable from the background noise. The cross phase between $\tilde{n}$ and $\dot{\tilde{B}}$ is around $\pi/4$. High coherence is observed between the D_α emission signal and the magnetic component, and the cross phase is around π.

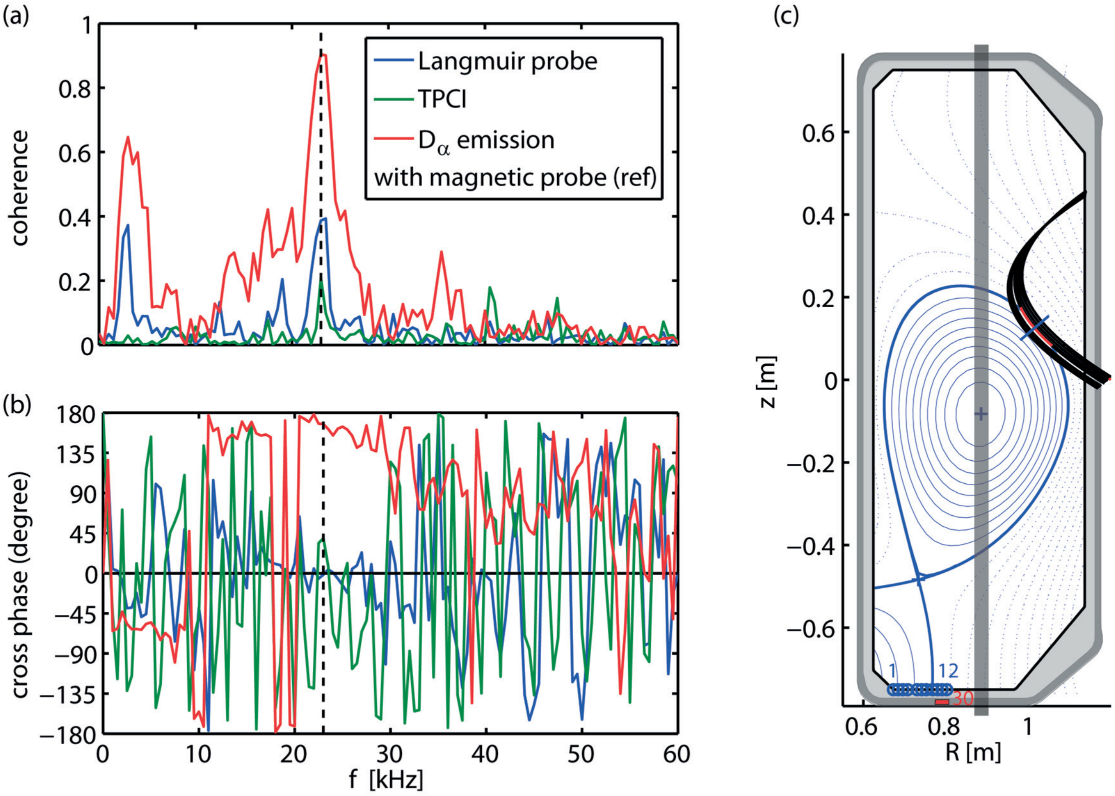

Figure 4.13: (a),(b) Squared coherence and cross phase of magnetic fluctuations (reference) and ion saturation current fluctuations at the outer strike point, density fluctuations at $\rho = 0.97$ and D_α emission intensity fluctuations in TCV discharge 54490, calculated in a 40 ms time window with 0.5 kHz frequency resolution. The black dashed line indicates the GAM peak at 23 kHz. (c) Plasma equilibrium and divertor configuration at $t = 0.45$ s in TCV discharge 54490. The black lines at the top right represent the poloidal projections of the TPCI laser chords, the red line highlight the chord used for analysis. The blue circles labeled from 1 to 12 represents the Langmuir probes, and the red square at $R = 0.79$ m labeled as 30 is the magnetic probe used for analysis. The gray rectangular box represents the vertical D_α line-of-sight.

4.4.3 Mode distribution near strike points

A strike point sweep was performed to study the localization of GAMs in the SOL, as shown in Fig. 4.14 (a). In this discharge, the outer strike point is swept from the HFS to the LFS during the LSN phase with nearly constant poloidal flux expansion ($f_x = 3-4$). Here we focus on the time interval $t = 0.4-0.5$ s with R_{SP} sweeping from 0.685 m to 0.858 m, through the Langmuir probe array from probe 1 to 19. At $t = 0.4$, 0.45, and 0.5 s, the strike point is roughly at the position of magnetic probes 31, 30 and 29, respectively. Fig. 4.14 (b) shows the spectrogram of signals from Langmuir probes $9-11$ at $t = 0.43-0.47$ s and Fig. 4.14 (c) shows the spectrogram of magnetic probes 31 to 29 at $t = 0.35-0.55$ s. The GAM frequency is about 24 kHz. It can be seen from the spectrogram that the time range in which GAMs can be observed on a given Langmuir probe is around 10 to 20 ms, while GAMs can last on a magnetic probe for more than 100 ms over the entire sweeping phase. The complete mode power profile at the target is reconstructed using all 19 Langmuir probes and 5 magnetic probes on the vessel floor, as shown in Fig. 4.14 (d) and (e) for the $\tilde{J}_{i,sat}$ and $\tilde{B}$ components respectively. The distribution of the $\tilde{J}_{i,sat}$ GAM mode power on the divertor target is very similar to the shape of the overall $\tilde{J}_{i,sat}$ distribution, which peaks about 1.2 cm outside the strike point in the common flux region and the full width half maximum (FWHM) is 3.7 cm, therefore it's almost absent in the private flux region; the target distribution of $\tilde{B}$ has a much larger FWHM (8 cm) and peaks inside the strike point (-1.15 cm), so it can be observed in both the common and the private flux region. Note that after $t = 0.5$ s when the outer strike point is on the LFS inclined wall structure, the GAM mode power vanishes, which is not reflected in the single curve shown in Fig. 4.14 (d) and (e). In addition to the dependence of the magnetic GAM signal on the location relative to the SP, there is a therefore also an overall decrease in signal as the SP moves towards to the LFS.

In a LSN flaring experiment, illustrated by Fig. 4.15, the amplitude of the $\tilde{B}$ component of the GAMs is found to increase with the poloidal flux expansion f_x. The outer strike point is slowly swept towards the HFS away from magnetic probe 30 from $t = 0.5$ to 1 s, with the distance between the two increasing from 9 to 17 cm during this time. However, the amplitude of the GAM increases during this sweep as shown in Figs. 4.15 (b) and (c), instead of decreasing as one would expect from Fig. 4.14 (e). This suggests that the distribution of the SOL $\tilde{B}$ component is affected by other parameters such as indeed the flux expansion. Fig. 4.15 (a) illustrates that although the strike point is moving away, the nearest flux surface to the magnetic probe 30 (within the resolution of the plot) is actually closer to the LCFS at $t = 1$ s than at $t = 0.5$ s, due to the effect of flux expansion. Therefore instead of the radial distance from the probe to the strike point, the radial distance at the outer midplane (upstream) from LCFS to the nearest flux surface to the probe is used for analysis, as shown in Fig. 4.15 (d). The mode power profile peaks on the SOL flux surface 1.5 cm outside LCFS with a very narrow 0.69 cm FWHM, and drops to nearly zero before reaching the LCFS. This contradicts with the observation that the SOL $\tilde{B}$ component peaks at the target as shown in Fig. 4.14 (e). Note that the curve in Fig. 4.14 (e) includes only data from a discharge with nearly constant flux expansion ($f_x = 3-4$). Therefore the GAM mode target distribution is modified by the flux expansion, further investigations are needed to understand this observation.

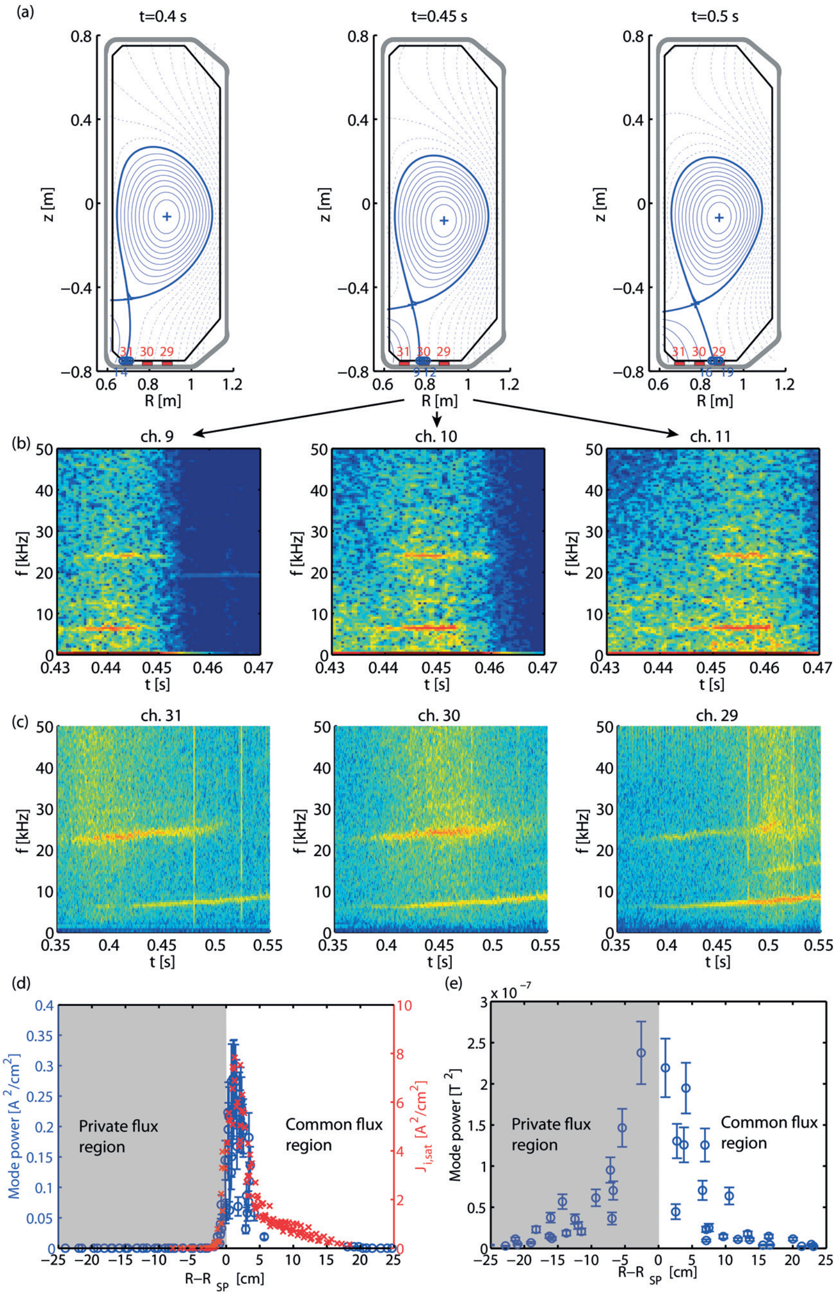

Figure 4.14: (a) Plasma equilibrium and divertor configuration at $t = 0.4$, 0.45 and 0.5 s in TCV discharge 54490. Langmuir probes and magnetic probes are represented in the same way as in Fig. 4.13. (b),(c) Auto-power spectrogram of ion saturation current fluctuations from Langmuir probes 9 to 11, and magnetic fluctuations from magnetic probes 31 to 29. Distribution of GAM mode auto-power component on (d) Langmuir probe and (e) magnetic probe signals along the target as a function of radial distance to the outer strike point; the mode power is integrated from 20 to 30 kHz in a 28 ms time window with 0.5 kHz frequency resolution. The red crosses indicate the total ion saturation current distribution. Shaded region indicates the private flux region.

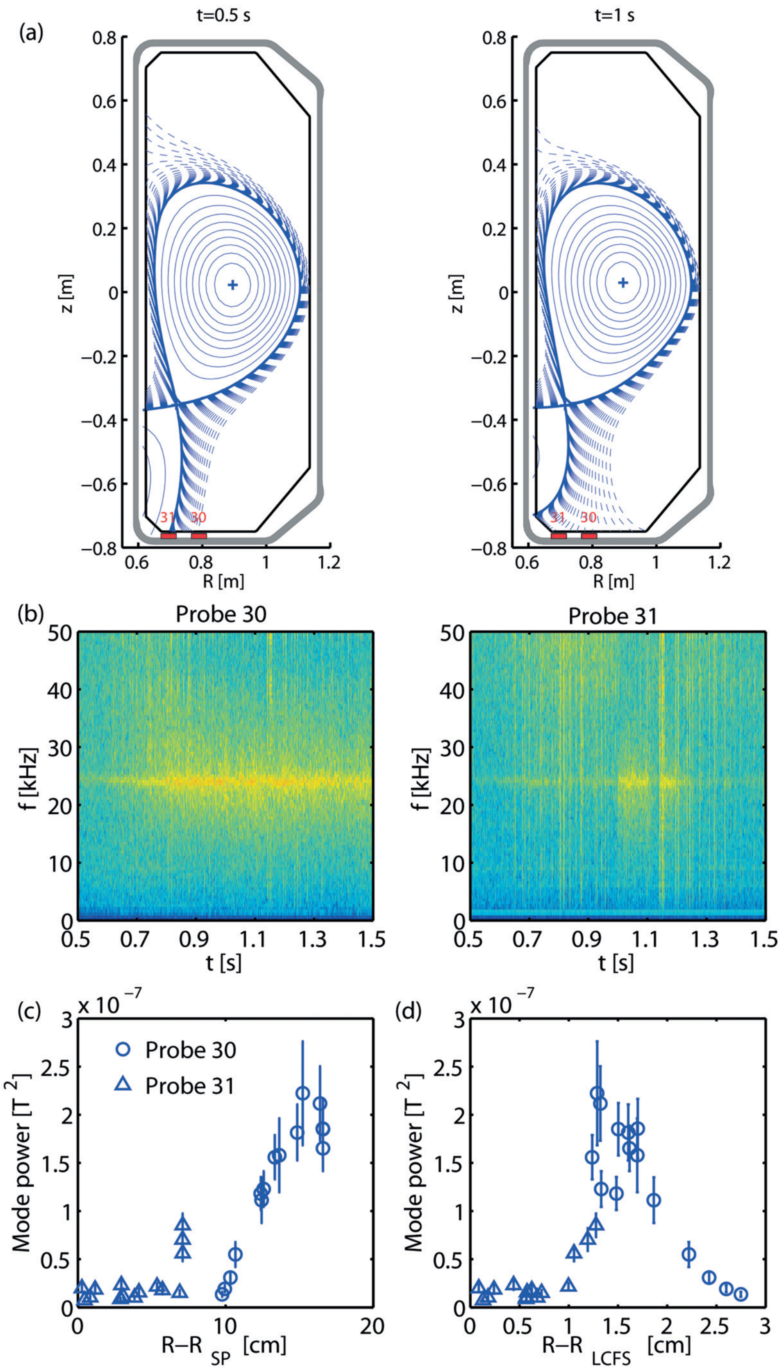

Figure 4.15: (a) Plasma equilibrium (solid curves) and SOL open flux surfaces (dashed curves) in TCV discharge 54816 at $t = 0.5$ and 1 s with low and high poloidal flux expansion, respectively. The magnetic probes are represented in the same way as in Fig. 4.13. (b) Auto-power spectrogram of magnetic fluctuations from magnetic probes 30 and 31. Distribution of GAM mode power on magnetic probes 30 and 31 as a function of (c) radial distance to the outer strike point, and (d) the distance to LCFS at midplane. The mode power is integrated from 20 to 30 kHz over a 28 ms time window with 0.5 kHz frequency resolution.

4.4.4 GAMs in snowflake and super-X configurations

The studies of GAMs in the SOL were also extended to snowflake (SF) divertor and Super-X divertor discharges in TCV. The $\tilde{I}_{\mathrm{i,sat}}$ component of the GAM can be observed on the inner primary strike point of the SF- configuration. This result is mainly consistent with the heat flux reduction at the target from SN to SF configurations on TCV [60]: GAMs are only detectable on the strike points on which the heat flux and particle flux remain high in going from the SN to the SF divertor configuration. The magnetic component, as shown in Fig. 4.16, can be detected over a larger range as expected: in the SF- configuration (Fig. 4.16(a)), the GAM is detectable around both primary SPs at probes 31 and 35, as well as the bottom secondary SP around probe 29; in the SF+ configuration, it is mainly localized around the inner primary SP at probe 35 and the bottom secondary SP at probe 29; in the Super-X divertor configuration, it is located from the inner SP to probe 29 in both LSN and Super-X configurations. The absence of GAMs at the outer primary strike point in the SF+ and Super-X configuration is consistent with the fact that the mode power tends to vanish as the outer strike point moves towards the LFS even for a SN configuration, as stated earlier in this chapter.

4.4.5 Discussion

The observations of GAM oscillations on the Langmuir probe signals suggest that a particle flux modulated at the GAM frequency travels along the SOL field lines to the strike points. The radial distribution of the $I_{\mathrm{i,sat}}$ component is consistent with the heat flux distribution. This hypothesis would also explain the GAM oscillations on the D_α emission intensity, as the particle flux hits the divertor target inducing recycling at the GAM frequency. We would like to note here that results from GENE simulations also show a particle and heat flux modulated at the GAM frequency, which suggests a coupling between GAM oscillations and avalanches since zonal flows cannot drive radial transport alone. So far, no non-Gaussian probability distribution function (PDF) of density fluctuations has been obtained from TPCI observations. We note, however, that this is not incompatible with avalanche processes, in which a non-Gaussian PDF of heat fluxes can be obtained with Gaussian PDFs of temperature and density fluctuations. Also as no X-point physics is available in GENE, the predictions were for limited plasmas, in which case we should stress that we haven't observed any GAM signal on any SOL diagnostics such as inner wall Langmuir probes or D_α photodiodes. Further studies should be carried out in the future on the relation between GAM and avalanches.

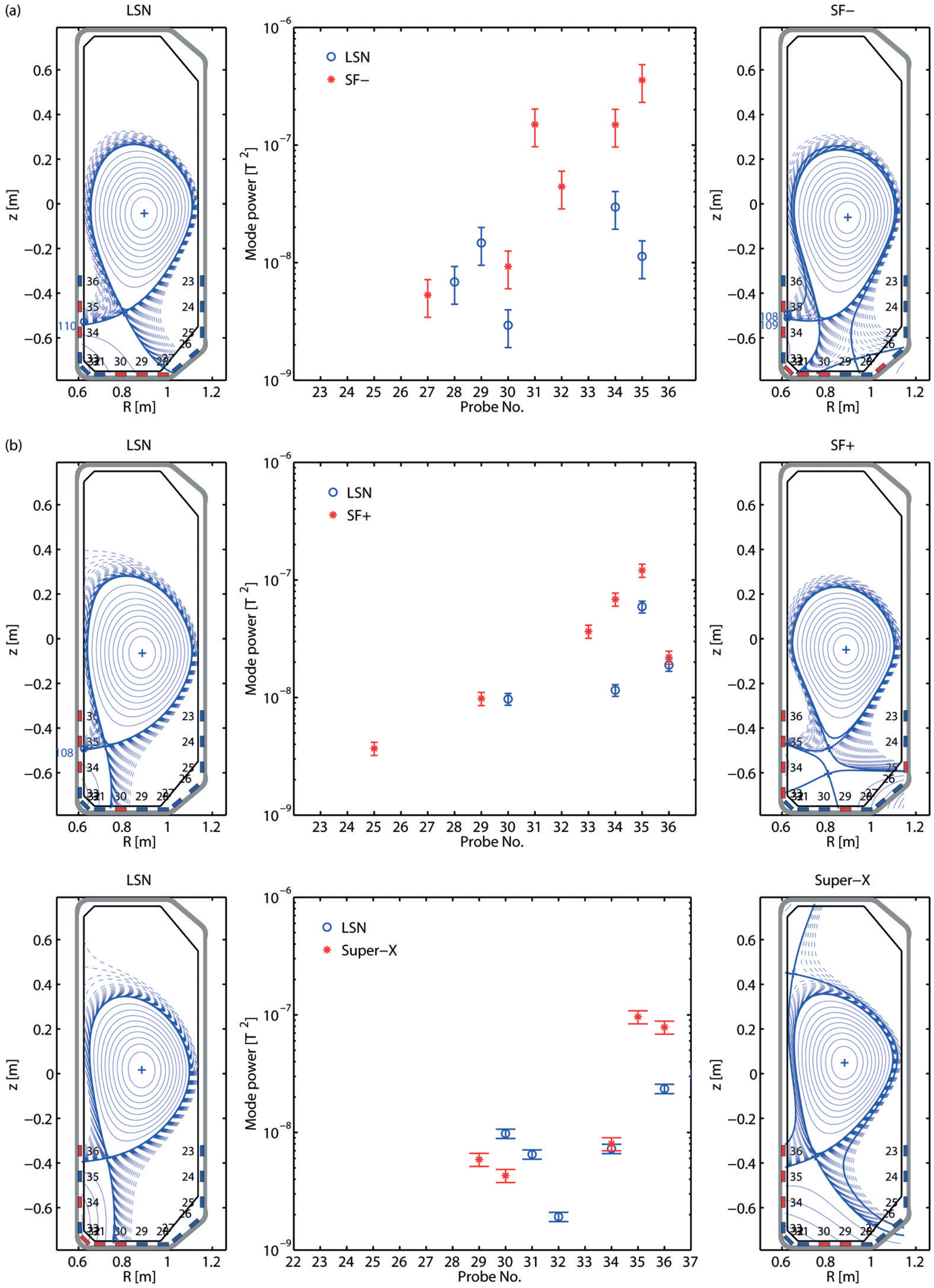

Figure 4.16: (Left and right) Plasma equilibrium of a SF- #54350 (a), SF+ #54378 (b) and a Super-X #54308 TCV discharge. The red squares highlight the magnetic probes on which the GAM is detectable; the blue circles represent the Langmuir probes. (Middle) GAM mode power on magnetic probes measured in these discharges, respectively. The blue circles indicate the LSN phase, the red stars indicate the SF/Super-X phase. The mode power is calculated by integrating the power spectrum over a 10 kHz frequency range around the GAM frequency, the spectrum is calculated over a 40 ms time window with 1 kHz frequency resolution.

5 Conclusions

In this thesis we studied the plasma turbulence in the TCV tokamak experimentally through density fluctuation measurements, primarily with the tangential phase contrast imaging diagnostic. Its physical principles and hardware setup are described in this thesis. The small-scale broadband turbulence was characterized in amplitude, frequency and wavenumber domain under different plasma conditions in order to understand the relation between the microinstabilities and the macroscopic transport phenomena. The geodesic acoustic mode was characterized with multiple diagnostics. Several novel phenomena in the GAM experiments were observed and discussed, the results are in good agreement with gyrokinetic simulations. The investigations on broadband plasma turbulence focused on one of the most interesting but not yet fully understood observations on the TCV tokamak: when the triangularity (δ) at the edge of the plasma poloidal cross-section changes from positive to negative, the energy confinement is improved, and the electron heat transport level is reduced at all radial locations in the outer half of the plasma, even though the triangularity has a finite radial penetration depth. Fluctuation measurements were performed in a series of limited TCV discharges including ECH L-mode and Ohmic plasmas. A substantial reduction of turbulence amplitude and decorrelation time was observed over a large plasma radius ($0.5 < \rho_{\mathrm{vol}} < 0.95$) from positive to negative triangularity, both in conditions of equal EC heating power and of similar density and electron temperature profiles. The power spectrum of the density fluctuations shows that the reduction is more pronounced in the low frequency range ($f < 100$ kHz). The negative triangularity plasmas has a narrower and less stiff core region [6] with higher critical gradient values, compared to the ones with positive triangularity.

Two triangularity scans were also performed for the inner core measurements ($\rho_{\mathrm{vol}} = 0.33$) where the gradients are below the critical gradient, one Ohmic and the other with $P = 1.35$ MW ECH. A reduction in turbulence amplitude in the low frequency range but no change in radial correlation length was observed in the Ohmic discharge; however, no significant turbulence amplitude reduction was observed in the ECH L-mode triangularity scan. This observation was explained by the impact of lower effective collisionality in negative triangularity due to higher temperature as a result of improved transport. Measurements with ECH power scans and Ohmic density scans show an offset-linear dependence of turbulence amplitude on the reciprocal of the effective collisionality $1/\nu_{\text{eff}}$, consistent with previous research on electron heat transport [7]. The improved confinement with negative triangularity can be characterized by reduced radial correlation length; the turbulence amplitude stays unchanged due to a lower effective collisionality.

As a self-organized phenomenon within plasma turbulence, the geodesic acoustic modes have been investigated further in experiments on the TCV tokamak. A general characterization [8] on multiple oscillating fields including $E \times B$ flow, density, magnetic and temperature components of the GAM has been reviewed. The mode is axisymmetric, has a $m = 2$ standing wave magnetic component, and its frequency varies globally proportionally to the square root of the temperature.

In most TCV L-mode plasmas, the GAM appears as a radially extended single-frequency mode, which differs from the conventional continuum GAM but shares many similarities with avalanches. A regime transition from continuum to single-frequency radially extended mode was observed and analyzed in an L-mode safety factor scan. Comparisons with global nonlinear gyrokinetic simulations suggest that the different density and temperature as well as their different gradient profiles are the underlying reason for the two different regimes. Further investigations are necessary to identify the mode, and also to understand the regime transition.

The interaction between GAMs and turbulence were studied in a density ramp-up, featuring a LOC-SOC transition. The GAM amplitude was found to decrease in the LOC phase but to remain independent of the collisionality in the SOC regime. The bicoherence spectrum shows that the nonlinear coupling between the GAM and the turbulence are only detectable at low densities. A quasi-coherent mode is also observed during the TEM-ITG mixed LOC phase and vanishes in the ITG dominant SOC phase. This observation is consistent with the QCM studies in Tore Supra and TEXTOR [58].

Finally, GAM oscillations have been observed and characterized on the SOL diagnostics near the strike points in various divertor configurations. This is the first study of its kind, even though GAMs were punctually detected before by, e.g., D_α measurements. An extensive characterization has been provided in varying divertor geometries. The results suggest a modulated particle flux that is partly consistent with gyrokinetic simulations. Its underlying physical mechanism remains to be understood and further suggests a relation with avalanche phenomena.

Bibliography

[1] Cornelis Adrianus de Meijere. *An Experimental Study of Plasma Fluctuations in the TCV and TEXTOR Tokamaks*. PhD thesis, École Polytechnique Fédérale de Lausanne, 2013.

[2] A. Marinoni, S. Coda, R. Chavan, and G. Pochon. Design of a tangential phase contrast imaging diagnostic for the TCV tokamak. *Review of Scientific Instruments*, 77(10):10E929, oct 2006.

[3] Alessandro Marinoni. *Plasma Fluctuation Studies in the TCV Tokamak : Modeling of Shaping Effects and Advanced Diagnostic Development*. PhD thesis, École Polytechnique Fédérale de Lausanne, 2009.

[4] J.-M. Moret, F. Buhlmann, D. Fasel, F. Hofmann, and G. Tonetti. Magnetic measurements on the TCV Tokamak. *Review of Scientific Instruments*, 69(6):2333–2348, 1998.

[5] G. D. Conway, E. Poli, T. Happel, and the ASDEX Upgrade Team. Interaction of Mean and Oscillating Plasma Flows Across Confinement Mode Transitions. *Plasma and Fusion Research*, 5:S2005, 2010.

[6] O. Sauter, S. Brunner, D. Kim, G. Merlo, R. Behn, Y. Camenen, S. Coda, B. P. Duval, L. Federspiel, T. P. Goodman, A. Karpushov, A. Merle, and the TCV Team. On the non-stiffness of edge transport in L-mode tokamak plasmas. *Physics of Plasmas*, 21(5):055906, 2014.

[7] Y. Camenen, A. Pochelon, R. Behn, A. Bottino, A. Bortolon, S. Coda, A. Karpushov, O. Sauter, G. Zhuang, and the TCV Team. Impact of plasma triangularity and collisionality on electron heat transport in TCV L-mode plasmas. *Nuclear Fusion*, 47(7):510, 2007.

[8] C. A. de Meijere, S. Coda, Z. Huang, L. Vermare, T. Vernay, V. Vuille, S. Brunner, J. Dominski, P. Hennequin, A. Krämer-Flecken, G. Merlo, L. Porte, and L. Villard. Complete multi-field characterization of the geodesic acoustic mode in the TCV tokamak. *Plasma Physics and Controlled Fusion*, 56(7):072001, jul 2014.

[9] P. C. Strangeby. *The Plasma Boundary of Magnetic Fusion Devices*. CRC Press, 2000.

[10] J.-M. Moret, S. Franke, H. Weisen, M. Anton, R. Behn, B. Duval, F. Hofmann, B. Joye, Y. Martin, C. Nieswand, Z. Pietrzyk, and W. van Toledo. Influence of Plasma Shape on Transport in the TCV Tokamak. *Physical Review Letters*, 79(11):2057, 1997.

[11] A. Pochelon, T. P. Goodman, M. Henderson, C. Angioni, R. Behn, S. Coda, F. Hofmann, J. P. Hogge, N. Kirneva, A. A. Martynov, J.-M. Moret, Z. A. Pietrzyk, F. Porcelli, H. Reimerdes, J. Rommers, E. Rossi, O. Sauter, M. Q. Tran, H. Weisen, S. Alberti, S Barry, P. Blanchard, P. Bosshard, R. Chavan, B. P. Duval, Y. V. Esipchuck, D. Fasel, A. Favre, S. Franke, I. Furno, P. Gorgerat, P. F. Isoz, B. Joye, J. B. Lister, X. Llobet, J. C. Magnin, P. Mandrin, A. Manini, B. Marletaz, P. Marmillod, Y. Martin, J. M. Mayor, J. Mlynar, C. Nieswand, P. J. Paris, A. Perez, R. A. Pitts, K. A. Razumova, A. Refke, E. Scavino, A. Sushkov, G. Tonetti, F. Troyon, W. Van Toledo, and P. Vyas. Energy confinement and MHD activity in shaped TCV plasmas with localized electron cyclotron heating. *Nuclear Fusion*, 39(11Y):1807, 1999.

[12] P. H. Diamond, S-I Itoh, K. Itoh, and T. S. Hahm. Zonal flows in plasma—a review. *Plasma Physics and Controlled Fusion*, 47(5):R35–R161, may 2005.

[13] K. Itoh, S.-I. Itoh, P. H. Diamond, T. S. Hahm, A. Fujisawa, G. R. Tynan, M. Yagi, and Y. Nagashima. Physics of zonal flows. *Physics of Plasmas*, 13(5):055502, may 2006.

[14] S. Coda, M. Porkolab, and K. H. Burrell. Signature of turbulent zonal flows observed in the DIII-D tokamak. *Physical Review Letters*, 86(21):4835, 2001.

[15] P. H. Diamond and H. Biglari. Theory of dissipative trapped-ion convective-cell turbulence. *Physical Review Letters*, 65(23):2865, 1990.

[16] E. Kim and P. H. Diamond. Zonal flows and transient dynamics of the L-H transition. *Physical review letters*, 90(18):185006, 2003.

[17] G. D. Conway, C. Angioni, F. Ryter, P. Sauter, and J. Vicente. Mean and oscillating plasma flows and turbulence interactions across the L-H confinement transition. *Physical Review Letters*, 106(6):065001, 2011.

[18] G. R. Tynan, M. Xu, P. H. Diamond, J. A. Boedo, I. Cziegler, N. Fedorczak, P. Manz, K. Miki, S. Thakur, L. Schmitz, L. Zeng, E. J. Doyle, G. M. McKee, Z. Yan, G. S. Xu, B. N. Wan, H. Q. Wang, H. Y. Guo, J. Dong, K. Zhao, J. Cheng, W. Y. Hong, and L. W. Yan. Turbulent-driven low-frequency sheared E × B flows as the trigger for the H-mode transition. *Nuclear Fusion*, 53(7):073053, 2013.

[19] M. A. Malkov, P. H. Diamond, K. Miki, J. E. Rice, and G. R. Tynan. Linking the micro and macro: L-H transition dynamics and threshold physics. *Physics of Plasmas*, 22(3):032506, 2015.

[20] J. C. Hillesheim, E. Delabie, H. Meyer, C. F. Maggi, L. Meneses, and E. Poli. Stationary Zonal Flows during the Formation of the Edge Transport Barrier in the JET Tokamak. *Physical Review Letters*, 116(6):065002, 2016.

[21] Niels Winsor. Geodesic Acoustic Waves in Hydromagnetic Systems. *Physics of Fluids*, 11(11):2448, 1968.

[22] G. D. Conway, C. Tröster, B. Scott, and K. Hallatschek. Frequency scaling and localization of geodesic acoustic modes in ASDEX Upgrade. *Plasma Physics and Controlled Fusion*, 50(5):055009, may 2008.

[23] P. Angelino, X. Garbet, L. Villard, A. Bottino, S. Jolliet, Ph Ghendrih, V. Grandgirard, B. F. McMillan, Y. Sarazin, G. Dif-Pradalier, and T. M. Tran. The role of plasma elongation on the linear damping of zonal flows. *Physics of Plasmas*, 15(6):062306, jun 2008.

[24] Zhe Gao. Plasma shaping effects on the geodesic acoustic mode in the large orbit drift width limit. *Physics of Plasmas*, 17(9):092503, sep 2010.

[25] G. Wang, W. A. Peebles, T. L. Rhodes, M. E. Austin, Z. Yan, G. R. McKee, R. J. La Haye, K. H. Burrell, E. J. Doyle, J. C. Hillesheim, M. J. Lanctot, R. Nazikian, C. C. Petty, L. Schmitz, S. Smith, E. J. Strait, M. Van Zeeland, and L. Zeng. Multi-field characteristics and eigenmode spatial structure of geodesic acoustic modes in DIII-D L-mode plasmas. *Physics of Plasmas*, 20(9):092501, sep 2013.

[26] T. Ido, Y. Miura, K. Kamiya, Y. Hamada, K. Hoshino, A. Fujisawa, K Itoh, S.-I. Itoh, A. Nishizawa, H. Ogawa, Y. Kusama, and JFT-2M Group. Geodesic–acoustic-mode in JFT-2M tokamak plasmas. *Plasma Physics and Controlled Fusion*, 48(4):S41–S50, apr 2006.

[27] A.V. Melnikov, L.G. Eliseev, S.V. Perfilov, S.E. Lysenko, R.V. Shurygin, V.N. Zenin, S.A. Grashin, L.I. Krupnik, A.S. Kozachek, R.Yu. Solomatin, A.G. Elfimov, A.I. Smolyakov, and M.V. Ufimtsev. The features of the global GAM in OH and ECRH plasmas in the T-10 tokamak. *Nuclear Fusion*, 55(6):063001, jun 2015.

[28] K. Itoh, S.-I. Itoh, P. H. Diamond, A. Fujisawa, M. Yagi, T. Watari, Y. Nagashima, and A. Fukuyama. Geodesic Acoustic Eigenmodes. *Plasma and Fusion Research*, 1:037–037, 2006.

[29] C. Wahlberg and J. P. Graves. Magnetohydrodynamic theory of the global structure and magnetic components of the geodesic acoustic continuum modes in tokamaks. *Plasma Physics and Controlled Fusion*, 58(7):075014, jul 2016.

[30] C. Wahlberg. Low-frequency magnetohydrodynamics and geodesic acoustic modes in toroidally rotating tokamak plasmas. *Plasma Physics and Controlled Fusion*, 51(8):085006, aug 2009.

[31] B. F. McMillan, S. Jolliet, T. M. Tran, L. Villard, A. Bottino, and P. Angelino. Avalanchelike bursts in global gyrokinetic simulations. *Physics of Plasmas*, 16(2):022310, 2009.

[32] F. Hofmann, J. B. Lister, W. Anton, S. Barry, R. Behn, S. Bernel, G. Besson, F. Buhlmann, R. Chavan, M. Corboz, M. J. Dutch, B. P. Duval, D. Fasel, A. Favre, S. Franke, A. Heym,

A. Hirt, C. Hollenstein, P. Isoz, B. Joye, X. Llobet, J. C. Magnin, B. Marletaz, P. Marmillod, Y. Martin, J M Mayor, J M Moret, C. Nieswand, P. J. Paris, A. Perez, Z. A. Pietrzyk, R. A. Pitts, A. Pochelon, R. Rage, O. Sauter, G. Tonetti, M. Q. Tran, F. Troyon, D. J. Ward, and H. Weisen. Creation and control of variably shaped plasmas in TCV. *Plasma Physics and Controlled Fusion*, 36(12B):B277–B287, 1994.

[33] T. P. Goodman and the TCV Team. Experience in integrated control of the multi-megawatt electron cyclotron heating system on the TCV tokamak: the first decade. *Nuclear Fusion*, 48(5):054011, 2008.

[34] Stefano Coda. *An Experimental Study of Turbulence by Phase-Contrast Imaging in the DIII-D Tokamak*. PhD thesis, Massachusetts Institute of Technology, 1997.

[35] W. C. Elmore and M. A. Heald. *Physics of Waves*. Dover Publications, 1985.

[36] Siobhan M. Barry. *The Extension of the FIR Interferometer of TCV to a Polarimeter and Measurements of the Faraday Rotation caused by the Poloidal Magnetic Field*. PhD thesis, National University of Ireland, 1999.

[37] F. Zernike. Beugungstheorie des schneidenver-fahrens und seiner verbesserten form, der phasenkontrastmethode. *Physica*, 1(7):689, 1934.

[38] H. Weisen. The phase contrast method as an imaging diagnostic for plasma density fluctuations. *Review of Scientific Instruments*, 59(8):1544, 1988.

[39] S. Coda, M. Porkolab, and T. N. Carlstrom. A phase contrast interferometer on DIII-D. *Review of Scientific Instruments*, 63(10):4974, 1992.

[40] F. Hofmann and G. Tonetti. Tokamak equilibrium reconstruction using Faraday rotation measurements. *Nucl. Fusion*, 28(10):1871, 1988.

[41] L. Vermare, P. Hennequin, Ö. D. Gürcan, C. Bourdelle, F. Clairet, X. Garbet, R. Sabot, and the Tore Supra Team. Impact of collisionality on fluctuation characteristics of micro-turbulence Impact of collisionality on fluctuation characteristics of micro-turbulence. *Physics of Plasmas*, 18:012306, 2011.

[42] T. Happel, A. Bañón Navarro, G. D. Conway, C. Angioni, M. Bernert, M. Dunne, E. Fable, B. Geiger, T. Görler, F Jenko, R. M. McDermott, F Ryter, and U Stroth. Core turbulence behavior moving from ion-temperature-gradient regime towards trapped-electron-mode regime in the ASDEX Upgrade tokamak and comparison with gyrokinetic simulation. *Physics of Plasmas*, 22(3), 2015.

[43] L. Vermare, P. Hennequin, Ö. D. Gürcan, and the Tore Supra Team. Detection of geodesic acoustic mode oscillations, using multiple signal classification analysis of Doppler backscattering signal on Tore Supra. *Nuclear Fusion*, 52(6):063008, 2012.

[44] L. C. Johnson and E. Hinnov. Ionization, recombination, and population of excited levels in hydrogen plasmas. *Journal of Quantitative Spectroscopy and Radiative Transfer*, 13(4):333, 1973.

[45] J. M. Beall, Y. C. Kim, and E. J. Powers. Estimation of wavenumber and frequency spectra using fixed probe pairs. *Journal of Applied Physics*, 53(6):3933, 1982.

[46] Y. C. Kim and E. J. Powers. Digital Bispectral Analysis and Its Applications to Nonlinear Wave Interactions. *IEEE Transactions on Plasma Science*, 7(2):120, 1979.

[47] Y. Censor. Row-action methods for huge and sparse systems and their applications. *SIAM Review*, 23(4):444, 1981.

[48] Y. Censor and A. Lent. An iterative row-action method for interval convex programming. *Journal of Optimization Theory and Applications*, 34(3):321, 1981.

[49] L. M. Bregman. The relaxation method of finding the common point of convex sets and its application to the solution of problems in convex programming. *USSR Computational Mathematics and Mathematical Physics*, 7(3):200, 1967.

[50] T. Vernay, S. Brunner, L. Villard, B. F. McMillan, S. Jolliet, A. Bottino, T. Görler, and F. Jenko. Global gyrokinetic simulations of TEM microturbulence. *Plasma Physics and Controlled Fusion*, 55(7):074016, 2013.

[51] A. Marinoni, S. Brunner, Y. Camenen, S. Coda, J. P. Graves, X. Lapillonne, A. Pochelon, O. Sauter, and L. Villard. The effect of plasma triangularity on turbulent transport: modeling TCV experiments by linear and non-linear gyrokinetic simulations. *Plasma Physics and Controlled Fusion*, 51(5):055016, 2009.

[52] G. Merlo, S. Brunner, O. Sauter, Y. Camenen, T. Görler, F. Jenko, A. Marinoni, D. Told, and L. Villard. Investigating profile stiffness and critical gradients in shaped TCV discharges using local gyrokinetic simulations of turbulent transport. *Plasma Physics and Controlled Fusion*, 57(5):054010, 2015.

[53] Gabriele Merlo. *Flux-tube and global grid-based gyrokinetic simulations of plasma microturbulence and comparisons with experimental TCV measurements*. PhD thesis, École Polytechnique Fédérale de Lausanne, 2016.

[54] Y. Camenen, A. Pochelon, A. Bottino, S. Coda, F. Ryter, O. Sauter, R. Behn, T. P. Goodman, M. A. Henderson, A. Karpushov, L. Porte, and G. Zhuang. Electron heat transport in shaped TCV L-mode plasmas. *Plasma Physics and Controlled Fusion*, 47(11):1971, 2005.

[55] A. Krämer-Flecken, S. Soldatov, D. Reiser, M. Kantor, and H. R. Koslowski. Investigation of geodesic acoustic modes and related zonal flows at TEXTOR. *Plasma Physics and Controlled Fusion*, 51(1):015001, 2008.

[56] V.V. Bulanin, V.K. Gusev, A.D. Iblyaminova, N.A. Khromov, G.S. Kurskiev, V.B. Minaev, M.I. Patrov, A.V. Petrov, Yu.V. Petrov, N.V. Sakharov, P.B. Shchegolev, S.Yu. Tolstyakov, V.I. Varfolomeev, F. Wagner, and Yu. Yashin. Geodesic acoustic mode investigation in the spherical Globus-M tokamak using multi-diagnostic approach. *Nuclear Fusion*, 56(1):016017, jan 2016.

[57] Akihide Fujisawa. A review of zonal flow experiments. *Nuclear Fusion*, 49(1):013001, jan 2009.

[58] H. Arnichand, R. Sabot, S. Hacquin, A. Krämer-Flecken, X. Garbet, J. Citrin, C. Bourdelle, G. Hornung, J. Bernardo, C. Bottereau, F. Clairet, G. Falchetto, and J.C. Giacalone. Quasi-coherent modes and electron-driven turbulence. *Nuclear Fusion*, 54(12):123017, 2014.

[59] H. Arnichand, R. Sabot, S. Hacquin, A. Krämer-Flecken, C. Bourdelle, J. Citrin, X. Garbet, J.C. Giacalone, R. Guirlet, J.C. Hillesheim, and L. Meneses. Discriminating the trapped electron modes contribution in density fluctuation spectra. *Nuclear Fusion*, 55(9):093021, 2015.

[60] H. Reimerdes, G. P. Canal, B. P. Duval, B. Labit, T. Lunt, W. A. J. Vijvers, S. Coda, G De Temmerman, T. W. Morgan, F. Nespoli, and B. Tal. Power distribution in the snowflake divertor in TCV. *Plasma Physics and Controlled Fusion*, 55(12):124027, dec 2013.

ZHOUJI HUANG

Rue du Valentin 22,
Lausanne CH-1004
Switzerland

Phone : +41 78 686 0969
+41 21 693 1917

Email : zhouji.huang@epfl.ch

EDUCATION

PhD candidate in plasma physics **2012 – present**
Swiss Plasma Center (SPC), Ecole Polytechnique Fédérale de Lausanne (EPFL)
Thesis: “Experimental Study of Plasma Turbulence in the TCV Tokamak”
Thesis director: Dr. Stefano Coda

MSc in Nuclear Fusion Science and Engineering Physics **2009 - 2011**
Erasmus Mundus FUSION-EP program
Thesis: “Probe measurement of electron temperature dynamics in TJ-K and ASDEX Upgrade”
Thesis supervisors: Dr. Mirko Ramisch, Dr. Bernhard Nold

Bachelor of Engineering **2004 – 2008**
Department of Engineering Physics, Tsinghua University

PUBLICATIONS

Z. Huang et al., “*Experimental observations of geodesic acoustic modes in the TCV tokamak*”, Plasma Physics and Controlled Fusion, to be submitted.

C. A. de Meijere et al., “*Complete multi-field characterization of the geodesic acoustic mode in the TCV tokamak*”, Plasma Phys. Control. Fusion **56** (2014) 072001

B. Nold et al., “*Influence of temperature fluctuations on plasma turbulence investigations with Langmuir probes*”, New Journal of Physics **14** (2012) 063022.

CONFERENCE CONTRIBUTIONS

“*Investigation of plasma turbulence and geodesic acoustic modes using tangential phase-contrast imaging in the TCV tokamak*”, Annual Meeting of the APS, Division of Plasma Physics, Nov. 16-20, 2015, Savannah, USA.

“*The electromagnetic geodesic acoustic mode in TCV*”, MHD Stability and Control Workshop, Nov. 22-24, 2015, PPPL, USA.

“*Structure and scaling of GAMs in TCV*”, EFTSOMP Workshop, June 29-30, 2015, Lisbon, Portugal.

“*The tangential phase-contrast imaging diagnostic on the TCV tokamak*”, EPS Conference on Plasma Diagnostics, April 14-17, 2015, Frascati, Italy.

“*Investigation of plasma turbulence and geodesic acoustic modes using tangential phase-contrast imaging in the TCV tokamak*”, EPS Conference, June 23-27, 2014, Berlin, Germany. P5.071.

“*Multi-diagnostic characterization of geodesic acoustic modes in the TCV tokamak*”, EPS Conference, July 1-5, 2013, Espoo, Finland. P2.175.

AWARDS

10th Itoh Project Prize in Plasma Turbulence at 41st EPS Conference on Plasma Physics	2014
Master thesis passed with “Greatest distinction”	2011